DEVELOPMENT OF A GIGAWATT REPETITIVE PULSE MODULATOR AND HIGH-PRESSURE SWITCH TEST STAND AND RESULTS FROM HIGH-PRESSURE SWITCH TESTS

A Thesis
presented to
The Faculty of the Graduate School
University of Missouri – Columbia

In Partial Fulfillment
of the Requirements for the Degree
Master of Science

---

by PETER NORGARD
Dr. Randy Curry, Thesis Supervisor

AUGUST 2006

The undersigned, appointed by the Dean of the Graduate School, have examined the thesis entitled:

DEVELOPMENT OF A GIGAWATT REPETITIVE PULSE MODULATOR AND HIGH-PRESSURE SWITCH TEST STAND AND RESULTS FROM HIGH-PRESSURE SWITCH TESTS

presented by Peter Norgard, a candidate for the degree of Master of Science, and hereby certify that in their opinion it is worthy of acceptance.

_____

Dr. Randy Curry

_____

Dr. Robert O'Connell

_____

Dr. Mark Prelas

ACKNOWLEDGEMENTS

I would like to acknowledge my advisor for letting me work at my own pace and making seemingly infinite resources available. I would like to thank Dr. Ken MacDonald for providing me with some insights into working with high-voltage technology and people. I would like to thank anyone who has let me verbalize an idea, and particularly those who have provided me feedback. I owe a special debt of gratitude to those who have given me a hand on the project—particularly Jeff (whose last name I cannot remember), Leland "Mark" Nichols and Russell "Rusty" Burdt, and also including (in no particular order) Tom Hancock, Numbers 1 and 2, Chris Yeckel, both Dustins, Kevin O'Connor, Brett Huhman, Josh Leckbee, Mark Kemp, and Andy Benwell. Also thanks to Nicholas Hudson for listening to my complaints about thesis writing and Microsoft Word.

TABLE OF CONTENTS

APPENDIX

LIST OF SYMBOLS

Symbol	Description	Units	Page
$\partial p/\partial V$	Volume-rate-change of the pressure, defines the compressibility of a fluid	N·m	4
k	Bulk modulus, defines the rate-constant of compressibility as a function of present volume	$N \cdot m^{-2}$ (Pa)	4
V	Volume, defines the present volume of a fluid undergoing compression or expansion	m^3	4
τ	Cavity collapse time, defines the time required for a cavity to collapse from some initial radius to zero radius	s	5
r_i	Initial radius, defines the initial radius of a collapsing cavity	m	5
ρ	Density, defines the density of the fluid surrounding the gas or vapor cavity	$kg \cdot m^{-3}$	5
p	Hydrostatic pressure, defines the pressure of a fluid surrounding a gas or vapor cavity	$N \cdot m^{-2}$ (Pa)	5
F	Force exerted by the bulk fluid on the boundary of a gaseous cavity of radius r	N	6
r	Radius of a spherical cavity	m	6
W	Energy, defines the energy required to form a cavity with a given radius in a pressurized fluid, also defines the energy deposited by an arc discharge	J	6
τ_r	Resistive-phase fall time, defines the exponential fall time of the resistive phase of an arc discharge	μs	6
Z	Source impedance, defines the impedance of the source driving an arc discharge	Ω	6

E_b	Breakdown electric field strength, defines the electric field at which 50% of the time a breakdown occurs	$MV \cdot cm^{-1}$	6
V	Breakdown voltage, defines the voltage just prior to the arc formation	kV	6
$v_2(t)$	Voltage across the initially uncharged capacitor as a function of time	V	12
v_1	Voltage across the initially charged capacitor at the instant prior to switch closure	V	12
C_1	Capacitance of the initially charged capacitor, equivalent to C_{bank}	F	12
C_2	Capacitance of the initially uncharged capacitor, equivalent to C_{coax}	F	12
ω_0	Resonant frequency of the CLC discharge	$rad \cdot s^{-1}$	12
t	Time	s	12
L	Inductance of the series element, equivalent to L_{mut}	H	13
$i(t)$	Current through the series inductance as a function of time	A	13
I_{RMS}	Root mean square current of a half-sinusoidal pulse	A	14
T	Period, defines the duration of the measurable current pulse	s	14
f	Frequency, defines the rate at which the current pulse is repeated	Hz	14
I_m	Peak current, defines the peak current magnitude	A	14
C_{coax}	Capacitance of a coaxial segment, defines the capacitance of the pulse forming line	F	15
ε_0	Permittivity of free space, defines the magnitude of polarizability of free space	$F \cdot m^{-1}$	15, 42, 59

ε_r	Relative permittivity of a dielectric, defines the magnitude of polarizability of a dielectric	none	15, 58
l	Length, defines the length of the coaxial structure	m	15
r_o	Outer radius, defines the inside radius of the outer conductor of a coaxial segment	m	15, 42, 59
r_i	Inner radius, defines the outside radius of the inner conductor of a coaxial segment	m	15, 42, 59
I^2t	Fusing-product for a semiconductor junction	$A^2 \cdot s$	21
$\int vdt$	Volt-seconds integral, defines the voltage-time product integral that is applied, or can be applied to a magnetic device	$V \cdot s$	25
N	Number of turns, defines the effective number of turns that magnetically couple to a magnetic device	none	25
$\int BdA$	Blocking product, defines the maximum volt-second product integral that can be tolerated prior to saturation (when applied to a magnetic device)	$T \cdot m^2$	25
L_{pri}	Self-inductance associated with the primary winding of a transformer	H	27
L_{sec}	Self-inductance associated with the secondary winding of a transformer	H	27
L_{leak}	Leakage inductance associated with a magnetic transformer, defines the inductance associated with magnetic fields that do not penetrate the magnetic material	H	27
L_{mut}	Mutual inductance associated with the primary-secondary coupling	H	27
k_T	Coupling coefficient, defines the quality of a transformer winding (a function of the ratio of mutual to leakage inductances)	none	27

$R_{ser,Pri}$	Series winding resistance associated with the primary winding	Ω	27
$R_{ser,Sec}$	Series winding resistance associated with the secondary winding	Ω	27
$n_{winding}$	Number of turns associated with either the primary or the secondary winding (winding-dependent)	turn	28
l_T	Per-turn length of a winding, defines the total length of either the primary or secondary winding when multiplied by $n_{winding}$	$m \cdot turn^{-1}$	28
ρ	Specific resistivity of the conductor used to wind the primary and secondary side of the transformer	$\Omega \cdot m^{-1}$	28
i	Current	A	29
H	Magnetic field strength, defines the magnetic field strength generated in the proximity of a current	$A \cdot m^{-1}$	29
l_m	Magnetic path length, defines the equivalent geometric mean path length of a magnetic device	m	29
n	Turns, defines the number of turns that couples magnetic fields into a magnetic device	none	29
Z	Surge impedance of a transmission line system	Ω	42
L	Total inductance of a transmission line segment	H	42
C	Total capacitance of a transmission line segment	F	42
μ_0	Permeability of free space, defines the magnetizability of free space	$H \cdot m^{-1}$	42
τ	Transit time of a transmission line system, defines the one-way propagation time	s	42
E_c	Energy, defines the energy stored as a result of the establishment of electric fields between two conductors	J	43

C	Total capacitance between two conductors at different voltages	F	43
V	Voltage difference between two conductors	V	43
E_{ap}	Applied electric field strength	$kV \cdot cm^{-1}$	44
E_b	Breakdown electric field strength, as defined earlier	$kV \cdot cm^{-1}$	44
n	Average number of charge cycles between dielectric failures	none	44
t_{eff}	Effective time, defines the time for which the voltage is above 63% of the peak voltage attained, determined *ex post facto*	μs	44
A	Stressed area, defines the area over which the electric field strength is large (ill-defined in the literature), generally taken to be the exposed area of an electrode system	cm^2	44
f	Field enhancement factor, defines the ratio of local maximum to average electric field strengths	none	44
Γ	Reflection coefficient, defines the proportion of incident voltage that is not transmitted through an interface	none	50
σ	Conductivity, defines the conductivity of a conductive solution or material	$S \cdot m^{-1}$	51
l	Length, defines the length over which the resistive media exists	m	51
A	Area, defines the minimum cross sectional area of the resistive media perpendicular to the flow of current	m^2	51
R	Resistance, defines the absolute resistance of the resistive media	Ω	51
Q	Dissipated power, defines the average power absorbed by a resistive element	$J \cdot s^{-1}$	52
m	Mass, defines the mass of a resistive element	kg	52

c_p	Specific heat, defines the thermal inertia of a resistive element	$J \cdot kg^{-1} \cdot °K^{-1}$	52
ΔT	Temperature differential, defines the change in temperature given an input of power into a resistive element	°K	52
v_o	Voltage generated by the probe, defines the output voltage generated by the D-dot probe operating into an impedance	V	58
A_p	Area of the probe, defines the effective area exposed to the electric fields developed on the conductor of interest	m^2	58
R	Series output impedance, defines the magnitude of the impedance loading the output of the D-dot probe	Ω	58
dE/dt	Time-rate change of the electric field strength, defines the rate at which the electric field is changing	$V \cdot m^{-1} \cdot s^{-1}$	58
a	Arbitrary radius used in the computation of dE/dt	m	59
dv/dt	Time-rate change of the voltage, defines the rate at which the voltage on the conductor of interest is changing	$V \cdot s^{-1}$	59
σ_t	Circumferential tension, defines the tension, or hoop stress, developed in a thin-walled cylinder that is internally pressurized by a fluid	psi	72
t	Wall thickness, defines the thickness of the cylinder wall	in	72
r_i	Inner radius, defines the inner radius of the thin-walled cylinder	in	72
p	Internal pressure, defines the pressure of the fluid internal to the cylinder (assumes no external pressure)	psi	72

σ_b	Bolt tension, defines the tension developed in a bolt that retains two perpendicular plates between which there is a fluid under hydrostatic pressure	psi	73
A_p	Perpendicular area, defines the total area exposed to a high pressure fluid between two plates that are perpendicular (A_p is area on one plate)	in^2	73
n	Number of bolts, defines the total number of bolts holding	none	73
A_t	Thread area, defines the effective stressed area of a threaded stud	in^2	73

Chapter 1. Introduction

The need for an advanced concept, compact switch that is capable of achieving long lifetime under repetitive conditions has prompted the development of a rep-rate, high-pressure flowing oil switch and a high voltage test stand. A high pressure switch utilizing advanced design techniques has been incorporated into a rep-rate, high voltage pulse generator designed specifically to test the switch performance and lifetime. The pulse generator has been designed to approximate anticipated electrical needs in the field of directed energy, and is summarized in Table 1-1.

Table 1-1. Specifications of the pulse generation system.

Charge Voltage	-250 kV
Impedance	4.8 Ω
Discharge Current	25 kA
Pulse Duration	70 ns
Repetition Rate (Continuous)	20 pps
Repetition Rate (Burst)	100 pps

1.1. Previous Work

A large body of previous effort has been well established for oil-based switches operating under single shot and low energy conditions. Most of the efforts have attempted to analyze or otherwise describe the physical processes taking place in the liquid dielectric switch, in the hopes that the results in some way scale to other parameter ranges. Very little work has been performed in the arena of high energy, repetitive oil switching, and even less has been performed at pressures exceeding 100 psig.

Early breakdown studies of oil at high pressure were performed under static, single shot conditions by Kao and Higham [1]. Oil pressure was increased from atmospheric

pressure to approximately 350 psig and breakdown was studied. The Kao study found that the breakdown voltage increased as the hydrostatic pressure was increased up to a point, at which the hold off strength was observed to remain approximately constant. This saturation effect was found to take place near the critical point of the test fluids. The critical point occurs when the liquid and vapor phases become indistinguishable [2]. Additional studies have subsequently confirmed this finding [3, 4].

Following the single shot studies at pressure, a number of additional studies were later reported that examined streamer formation, bubble generation and extinction, and various other phenomena associated with liquid breakdown. In 1991 a rep-rate oil switch was reported in the literature by Curry et. al. [5]. The rep-rate oil switch was operated in short bursts at repetition frequencies up to 1 kHz, and pulse energies of 50 J. The study offered strong evidence that the ability of a switch to recover under repetitive conditions could be adversely affected by extreme flow rate. The study also found that it was necessary to pressurize the oil to 415 kPa to prevent the formation of vapor cavities for flow rates up to 5.2 $L \cdot s^{-1}$.

The limited scope of the experiments performed to date have not shed sufficient light on the issue of long-duration bursts operating at moderate energy levels. Consequently a test stand to study breakdown in long-duration bursts has been developed. The test stand utilizes pressurized, flowing oil as the dielectric medium and is designed to meet the specifications presented in Table 1-1.

1.2. HPS Concept

The design concept utilizes pressurized and flowing oil as the switching medium because this combination has several key advantages over current rep-rate switching

technologies. Oil dielectrics offer a number of advantages including increased safety, lower cost of maintenance, and greater platform compatibility when gas switches of comparable performance are considered. The benefits of pressurization and flow potentially increase the likelihood of rep-rate switch recovery during the inter-shot interval.

Platform compatibility is the most important reason for utilizing oil. The intended applications for the high pressure switch may place the switch on airborne platforms. The dielectric oil selected for the test switch, poly-α olefin, or PAO, is not only compatible with airframes but is in widespread use in the avionics already onboard most airframes [6]. Poly-α olefin is classified as a dielectric coolant under military specification number MIL-PRF-87252C. The important properties of PAO include low viscosity at low temperatures, high resistance to oxidation, and a flash point of 160 °C [7].

Maintenance costs associated with PAO have been found to be quite low. Under repetitive conditions with moderate discharge energy (~ 250 J per pulse) the oil does not degrade significantly. Gas column mass spectrographic analysis of used PAO, when compared to new PAO, exhibited virtually no difference in the chemical compositions. Furthermore, PAO is a very good lubricant and is currently one of the major components in many synthetic motor oils. Poly-α olefin effectively resists aging under repetitively pulsed conditions and provides good lubrication to the hydraulic equipment and thus, should result in lower operating and maintenance costs than other liquid dielectrics.

Oil dielectrics are much safer to operate at high pressure due to the relative incompressibility of most liquids. Incompressibility is a mechanical property that relates the applied compressive force to a change in volume, often characterized by the modulus

of compressibility in solids, or bulk modulus in liquids. Equation (1.1) relates the change in volume, ∂V in m^3, to an incremental applied pressure, ∂p in Pa, the initial volume, V in m^3, and the bulk moudulus, k in Pa [8]. The bulk modulus for liquids is in the range of 10^8 to 10^{10} Pa [9]. Using a typical bulk modulus value of approximately 10^9 Pa, a volume of 1 m^3, and an incremental pressure of 10.34 MPa (1500 psig), the approximate change in volume ∂V is -0.0103 m^3, or about 1 part per hundred. The small change in volume when a liquid is pressurized means the oil will not expand very much if it is suddenly decompressed.

$$\frac{\partial p}{\partial V} = -kV \qquad (1.1)$$

The principal concept behind the use of pressurized oil is to reduce the absolute volume of gaseous byproducts generated during a discharge. During a discharge the oil molecules within the immediate vicinity of the arc channel are either vaporized or burned. It is believed that the vapor and gas cavities that remain are particularly susceptible to dielectric failure since gases tend to break down at lower applied electric field strengths than liquids [10]. A fundamental limit to the upper pulse repetition frequency in any liquid dielectric is the rate at which gaseous byproducts can be cleared from the electrically stressed region between the anode and cathode electrodes.

The gaseous byproducts may be swept from the region by sufficiently high oil flow rates. It is easy to show that for repetition rates in the range of 100 to 1,000 pps the flow rate required to move a cavity out of the stressed region of a switch, though geometry dependent, can be large. The primary problem associated with high flow rates is pump power consumption. A secondary problem associated with high flow rates is due to the Bernoulli principal in which pressure within an orifice is inversely proportional to the

flow rate through the orifice. The flow rate can be increased to such an extent that the pressure within the orifice reaches the vapor pressure of the fluid and then cavitation ensues [5]. Cavitation is the formation of vapor cavities within the fluid—a condition that is not favorable for switch recovery.

An alternative approach to increase the recovery rate is to utilize increased oil pressure to drive up the rate at which hydrodynamic transients occur. Under the assumption that the vapor pressure remains constant over the range of pressures attainable in the laboratory, and over similar ranges of oil flow rate and oil temperature, an increase in the operating pressure increases the probability that the occurrence of a vapor cavity will be a transitory event. Indeed the cavity will experience increased rates of extinction through damped oscillatory motions as well as increased rates of absorption within the oil.

As described, the rate of cavity extinction through damped oscillation increases as the operating pressure is increased. The equation that describes the oscillation rate is based on conservation of momentum and was worked out by Lord Rayleigh and published in 1917 [11]. Equation (1.2) is Rayleigh's fundamental finding and describes the duration of the collapse of a cavity under static ambient pressure. In (1.2) τ is the time to collapse in seconds, r_i is the initial (starting) radius of the cavity in meters, ρ is the fluid density in $kg \cdot m^{-3}$, and p is the hydrostatic pressure in Pa. Under the assumption that the process is symmetric with respect to time, the cavity oscillation period may be determined for any cavity. From (1.2) it is clear that the oscillation period is inversely proportional to the square-root of the pressure; increasing pressure causes a decreasing oscillation period and in a viscous fluid, such as oil, the cavity extinguishes more rapidly.

$$\tau = \frac{1}{1.0931} r_i \sqrt{\frac{\rho}{p}} \qquad (1.2)$$

The initial cavity radius, r_i, is quite important for determining the relative temporal duration of the cavity. Taking a first-principals approach to the problem it is a simple matter to estimate the initial cavity radius given a known energy deposition, *W*. The first step is to identify a function that describes the force on the outer boundary of a spherical cavity, which is simply the external (bulk fluid) pressure times the surface area of the cavity, or $F = 4\pi P r^2$ (*F* in newtons, *P* in pascals, and *r* in meters). The work done to create the full-sized cavity is simply the opposing force times displacement, which when worked out for the spherical cavity results in equation (1.3) (*W* in joules, other units as defined) [12]. Provided a good initial guess can be made for *W*, the cavity initial radius is known with reasonable precision. Equation (1.3) is not exact because it fails to address the many loss modes present.

$$W = \frac{4}{3} P \pi r_i^2 \qquad (1.3)$$

Using an established method for estimating energy deposition in the arc channel, a reasonable estimate of the energy required to generate a cavity is developed. The approach taken utilizes the switch loss equation developed by J. C. Martin, presented as equation (1.4) [13]. The energy dissipated in an arc channel, *W* in joules, occurs mostly as a result of Joule heating during the decay of arc-channel resistance. The arc channel decays exponentially with a time constant, τ_r, given by equation (1.5), where *Z* is the source impedance in Ω, E_b is the electric field strength at breakdown in $MV \cdot cm^{-1}$, and τ_r is resistive-phase time constant in nanoseconds [10]. Returning to (1.4), the voltage *V* in kV is the charge voltage at breakdown, *Z* is the source impedance in Ω, and the resistive

rise time constant is in microseconds. The energy deposited in the arc channel is about 7.6 J when breakdown occurs at 250 kV and 1.2 MV·cm^{-1} on a 4.8 Ω pulse generator.

$$W = \frac{V^2 \tau_r}{4Z} \qquad (1.4)$$

$$\tau_r = \frac{5}{Z^{1/3} E_b^{4/3}} \qquad (1.5)$$

The anticipated size of the cavity generated as a result of electrical discharge may be estimated by utilizing the energy deposition value found in equation (1.3). The cavity radius is pressure dependent, so some extremes are selected for evaluation: atmospheric pressure (101 kPa) and high pressure (10 MPa). At 101 kPa the cavity size would be 2.62 cm in radius and at 10 MPa the radius would be 5.66 mm. In both cases the cavity is expected to be several times greater than the gap spacing. The boundary constraints offered by the electrodes will result in a geometric distortion in the shape of the cavity. Instabilities that arise from sliding contact with the electrode surface, as well as Rayleigh-Taylor fluid instabilities, will cause the single cavity to undergo a breakup process as the cavity contracts during the first oscillation period. The resulting collection of smaller cavities will still obey the Rayleigh oscillation criterion, however it is possible that additional constrained-geometry breakups will occur. Eventually, however, all of the cavities in a pressurized fluid will be absorbed by the fluid provided the fluid remains under saturated.

An added benefit of oil pressurization is an increase in the ability of the oil to absorb gases. Figure 1-1 demonstrates the increase in gas absorption as a function of pressure [14]. Figure 1-1 indicates that for pressures approaching the critical pressure of an oil (typically about 2 MPa +/- 1MPa) the oil can absorb a volume of gas nearly twice the

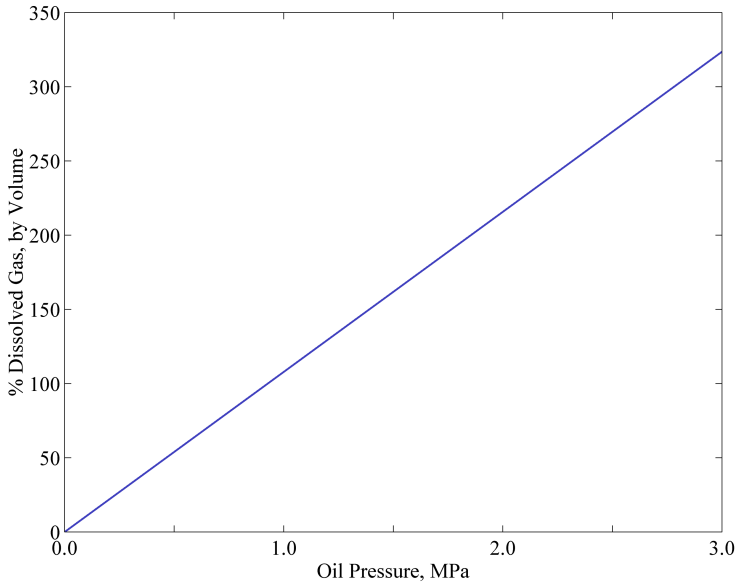

Figure 1-1. Gas absorption capacity of oil as a function of oil pressure.

volume of the oil. The total volume of gas that can be absorbed therefore depends on the total volume of oil that will be utilized. The oil will become over saturated when it returns to the low-pressure reservoir, thus releasing the absorbed gas to the atmosphere.

The gas absorption rate is strongly dependent upon the surface area of the cavity exposed to under saturated liquid oil. A single cavity of a given volume can be shown to have less surface area than a collection of smaller cavities with an equivalent sum-total volume. Therefore the cavity breakup that occurs during a constrained-geometry cavity expansion/collapse cycle can be beneficial at lower flow rates due to enhanced rates of absorption.

Solid phase byproducts are generated during a discharge, in addition to the gaseous cavities discussed previously. The solid particles include carbon that results from the incomplete combustion of the oil as well as metal particles that are ablated from both electrodes by the arc. The solid particles are swept away from the electrically stressed region between the electrodes with hydraulic flow that is incorporated into the switch.

The oil flow profile throughout the regions immediately above and below the stressed region, as well as the stressed region itself, must be meticulously designed to reduce the possibility of particle entrapment due to turbulent vortexes.

1.3. Experimental Goals

The program seeks to characterize the performance of a rep-rate switch that utilizes high-pressure oil as the dielectric switching medium. The performance of the switch was characterized by analyzing the statistical properties of the breakdown voltage under a range of operating conditions. The statistical properties that were characterized and studied include the mean breakdown voltage and different ranges of the breakdown voltage that relate the shape of the distribution of shots.

The program also identified and tested electrode materials that were compatible with the operating conditions and constraints. The electrode materials identified were tested in a full-scale high-pressure switch for evaluation over a large number of shots ($\geq 1x10^5$ shots). The electrodes were then examined and the erosion characterized.

1.4. Test Verification Program

A test verification program was undertaken at the University of Missouri-Columbia to verify the operating characteristics of a high-pressure switch. The test verification program was a multifaceted program that characterized operation of a high-pressure switch using a 250-300 kV test stand constructed at the University of Missouri-Columbia. The test stand as shown in Figure 1-2 is comprised of a high voltage power supply, a thyratron switched modulator, a pulse transformer, a water filled pulse forming line, a housing for the DVT switch and a flowing copper sulfate resistive load. The test stand was designed to operate for 10^9 pulses and was designed for test and measurement as

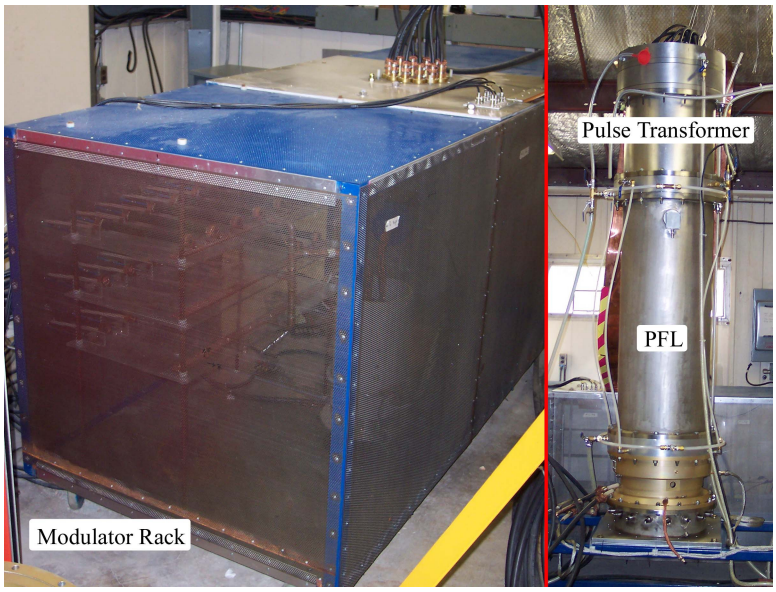

Figure 1-2. Photograph of the pulse modulator, the pulse transformer, and the pulse forming line.

well as optimization of the high-pressure switch fluid dynamics and electrode erosion. The test stand also includes a hydraulic pump cart for pressurization and fluid flow in the test switch. The test stand is depicted in a block diagram in Figure 1-3.

A number of diagnostic probes were installed on the test stand to monitor the electrical performance of the modulator and switch. The modulator current is measured with a commercial current transformer. Switch cathode and anode voltages were measured with high-speed D-dot probes custom designed for the test stand. Capacitive voltage probes were also installed on the transmission lines that connect between the switch and the

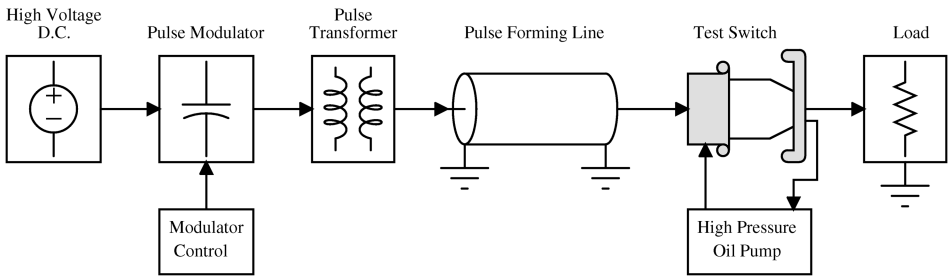

Figure 1-3. Diagram of the high-pressure switch test stand.

resistive load.

During the design-verification test (DVT) switch tests, modeling of the fluid dynamics was utilized to understand and optimize the DVT switch. The test stand allowed the switch fluid dynamics to be optimized and flow shapers designed for the switch to mitigate flow instabilities in the switch. The optimized fluid flow shapers were verified using the high voltage test stand and concurrently electrode materials and shapes were characterized. The tests at UMC allowed a compact switch to be designed and delivered to the Air Force Research Laboratory upon completion of the program.

1.5. References

[1] K. C. Kao and J. B. Higham, "The effects of hydrostatic pressure, temperature, and voltage duration on the electric strength of hydrocarbon liquids," *J. Electrochem. Soc.*, vol. 108, no. 6, June 1961, pp. 522 – 528.

[2] J. P. Holman, "Thermodynamics," McGraw-Hill Inc., New Yori, 1969, pp. 51 – 72.

[3] Z. Krasucki, "Breakdown of liquid dielectrics," *Proc. Royal Soc. London Ser. A: Mathem. and Phys. Sci.*, vol. 294. no 1438, 4 October 1966, pp. 393 – 404.

[4] K. C. Kao and J. P. McMath, "Time-dependent pressure effect in liquid dielectrics," *IEEE Trans. Elec. Ins.*, vol. EI-5, no. 4, September 1970, pp. 64 – 68.

[5] R. D. Curry, P. D'A. Champney, C. Eichenberger, J. Fockler, D. Morton, R. Sears, I. Smith, and R. Conrad, "The development and testing of subnanosecond-rise, kilohertz oil switches for the generation of high-frequency impulses," *IEEE Trans. Plasma Sci.*, vol. 20, no. 2, June 1991, pp. 383 – 392.

[6] J. Khodorkovsky, B. Khusid, A. Acrivos, M. Beltran, "*Comprehensive electrical evaluation of polyalphaolefin (PAO) dielectric coolant*," Beltran Inc., Brooklyn, NY., Naval Air Warfare Ctr. Rpt. N68335-97-C-0025, 12 November 1997.

[7] *Performance specification, coolant fluid, hydrolytically stable, dielectric*, Military Specification MIL-PRF-87252C, 24 October 1997.

[8] V. L. Streeter, "*Fluid mechanics, 5th Ed.*," McGraw-Hill Book Co., New York, 1971, pp. 3 – 26.

[9] R. K. Moore, "*Traveling-wave engineering,*" McGraw-Hill Book Co., New York, 1960, pp. 42 – 87.

[10] J. C. Martin, "Nanosecond pulse techniques," *Proc. IEEE*, vol. 80, no. 6, June 1992, pp. 934 – 945.

[11] L. Rayleigh, "On the pressure developed in a liquid during the collapse of a spherical cavity," *Phil. Mag.*, vol. 32, 1917, pp. 94 – 98.

[12] D. Halliday, R. Resnick, and J. Walker, "Fundamentals of physics, 5th Ed.", John Wiley and Sons Inc., New York, 1997, pp. 131 – 147.

[13] T. H. Martin, J. F. Seamen, and D. O. Jobe, "Energy losses in switches," *Proc. 9th Int'l. IEEE Pulsed Power Conf.*, vol. 1, 1993, pp. 463 – 470.

[14] G. Andersen, The Boeing Co., private communications, Aug. 2005.

Chapter 2. Pulse Modulator and Pulse Transformer

A test stand was developed to support the high-pressure flowing-dielectric switch program described in Chapter 1. As shown by the block diagram in Figure 1-3 the modulator operates at 25 to 30 kV and pulse charges the water pulse forming line through the primary winding of the pulse transformer in 2.5 μs. The pulse transformer provides a voltage gain of ten into the pulse forming line, generating -250 to -300 kV across the DVT switch. The modulator was tested at rep-rates of up to 20 pps continuously, and 100 pps in burst mode. The modulator design was complicated by the switch-out voltage of the pulse forming line (PFL).

2.1. Pulse Modulator

The pulse modulator was designed around a CLC resonant discharge topology. The resonant topology utilized is comprised of the modulator capacitance, the transformer leakage inductance and the capacitance of the pulse forming line. The modulator capacitor is initially charged and is discharged into the uncharged capacitance formed by the PFL. The resulting waveform is given mathematically in equation (2.1) [1].

$$v_2(t) = \frac{C_1 v_1}{C_1 + C_2}\left(1 - \cos\left(\omega_o t\right)\right) \qquad (2.1)$$

In the equation the voltage on the initially uncharged capacitor, v_2, is given as a function of the voltage on the initially charged capacitor, v_1, and circuit parameters C_1 and C_2 in Farads, the time, t, in seconds, and the resonant frequency, ω_0, in rad·s^{-1}. The resonant frequency is given as a function of circuit elements in equation (2.2), where the capacitances are in Farads and the inductance is in Henries [2, 3].

$$\omega_o = \sqrt{\frac{1}{L}\left(\frac{C_1 + C_2}{C_1 C_2}\right)} \qquad (2.2)$$

In addition to the voltage on C_2, the current through the modulator loop is important for the estimation of the RMS loop current. The current in a CLC discharge is given by equation (2.3) where the parameters have already been defined [2, 3].

$$i(t) = \frac{\omega_0 v_1}{\left(\frac{1}{C_1} + \frac{1}{C_2}\right)} \sin(\omega_0 t) \quad (2.3)$$

A schematic diagram of the pulse modulator is shown in Figure 2-1. The initially charged capacitor, C_1, described in (2.1) is C_{bank} in Figure 2-1, while the initially uncharged capacitor, C_2, in (2.1) is the net parallel capacity of the pulse forming line (PFL). The series leakage inductance of the pulse transformer, L_{leak}, provides the resonant inductance described by L in (2.2). The two current loops comprising the complete circuit during a pulse are magnetically coupled through the pulse transformer. The switch that initiates a pulse discharge is a hydrogen thyratron, labeled CX1625AS in Figure 2-1.

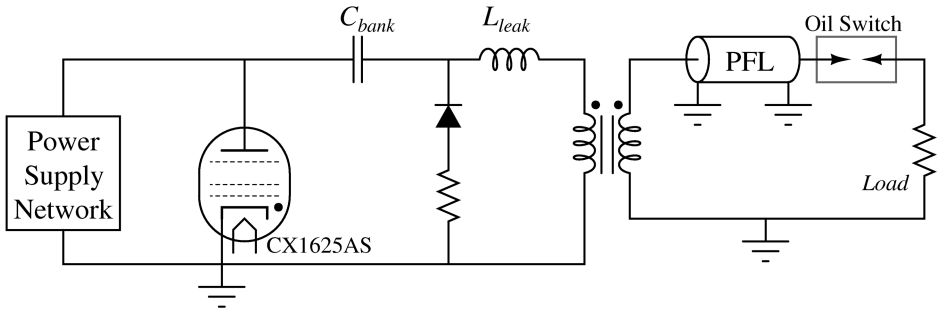

Figure 2-1. Schematic diagram of the pulse modulator layout.

Additional circuit elements are shown in Figure 2-1 that are not necessary for the production of current pulses, but are nevertheless important. A network of high voltage power supplies is utilized to provide the capacitor bank, C_{bank}, with an initial charge

voltage at high average power levels. A series resistor-diode network is utilized to clamp negative current transients that are reflected back to the modulator during normal oil switch operation. Under normal operating conditions the high-pressure DVT switch was found to self break over the range of 50 to 100 % of the peak charge voltage, depending upon oil conditions (pressure, flow, or temperature). Additional elements, not shown in Figure 2-1, provide magnetic core reset, thyratron switch control, system control, and safety.

2.1.1. Resonant Elements

The primary storage capacitor, C_{bank} in Figure 2-1, is represented in the circuit by an array of nine parallel high-voltage metal-film capacitors. Each capacitor is nominally 90 nF, bringing the total capacitor bank capacity to 810 nF. The total stored energy on the capacitor bank is about 250 J when the capacitor bank is charged to 25 kV. Table 2-1 provides a summary of the specification limits and parameters of the individual capacitors [4].

Design calculations and simulations were utilized to verify that the operating conditions remained within the specification limits. The RMS current of a burst of pulses was estimated with equation (2.4), where I_m is the peak amplitude of the current pulse in

Table 2-1. Summary of capacitor specifications. Estimated based on dissipation factor.

Manufacturer	Maxwell Labs
Part Number	31662
Capacitance	90 nF
ESR	90 mΩ†
ESL	80 nH
V_{max}	45 kV
I_{peak}	25 kA
I_{RMS}	25 A
$PRF_{max,cont}$	100 pps

amperes, T is the duration of the pulse in seconds, and f is the repetition rate in pulses per second [5]. From equation (2.3) the peak current switched by the thyratron was 11.9 kA. From equation (2.4) the RMS of the full capacitor bank was estimated at 60.1 A at a repetition frequency, f, of 20 pps and a discharge duration, T, of 2.547 μs. The per-capacitor RMS current was therefore 6.673 A and significantly below the rated value.

$$I_{RMS} = I_m \sqrt{\frac{Tf}{2}} \qquad (2.4)$$

The series inductance element in the resonant network, L_{leak} in Figure 2-1, was initially measured with a low-amplitude impedance bridge to obtain an approximate value for the design models. Following the assembly and testing of the pulse modulator and PFL, the value of L_{leak} was measured by ringing the capacitor bank through the pulse transformer and into the pulse forming line at a voltage below the breakdown value of the DVT switch. The time to attain the peak charge voltage on the PFL was found to be 2.547 μs, which gave a resonant frequency of 1.233×10^6 rad·s^{-1}. During the tests the capacitance of the PFL was assumed to be 738 nF. The resonant frequency observed under pulsed conditions suggested a leakage inductance of 1.703 μH. The leakage inductance value of 1.703 μH is utilized from this point forward in the models.

The PFL represents the second half of the resonant network in Figure 2-1. The PFL is a water-filled coaxial transmission line. The geometry was utilized to estimate the total capacitance of the PFL according to equation (2.5), where ε_r is 81, ε_0 is 8.85 pF·m^{-1}, r_o is the inner radius of the outer conductor in cm, r_i is the outer radius of the inner conductor in cm, and l is the total length in cm [6]. Evaluation of (2.5) with measured dimensions gives a net capacity of approximately 7.38 nF.

$$C_{coax} = \frac{2\pi\varepsilon_0\varepsilon_r l}{\boldsymbol{ln}\left(r_o / r_i\right)} \qquad (2.5)$$

2.1.2. Power Supply Network

Power is supplied to the modulator by a series of parallel power supply networks, each network consisting of a power supply, an isolation resistor, and a reverse voltage clamping diode. The circuit diagram in Figure 2-2 illustrates the interconnections utilized. Building power limited the available 3-phase current to the extent that only nine power supplies could be safely operated simultaneously.

The power supplies utilized were ALE 302S capacitor charging supplies. Capacitor charging supplies deliver a constant current to the load until the set-point voltage is attained, at which point the current output is reduced to a level sufficient to overcome capacitor and other losses. A summary of the power supply specifications is provided in Table 2-2 [8].

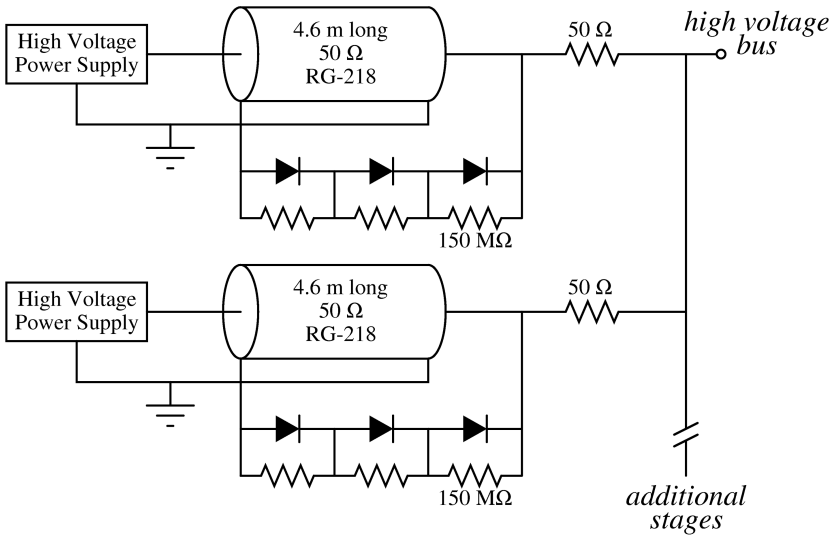

Figure 2-2. Schematic diagram of the power supply network.

Table 2-2. Specifications for individual power supplies.

Manufacturer	Applied Laser Electronics
Model Number	ALE 302S
V_{peak}	30 kV
P_{avg}	2 kW
No. of Supplies	9

Series isolation resistors were utilized to limit the magnitude of current transients generated during the modulator discharge. Specifications for the resistors employed are presented in Table 2-3. The resistors are high-power tubular ceramic elements that are 25 cm in length and 2.54 cm in diameter (outer). The resistors only dissipate power while the capacitor bank is being charged, and the amount of power dissipated per resistor is

Table 2-3. Series current limiting resistor specifications. † 40 °C ambient air.

Manufacturer	Kanthal-Globar
Part Number	889AS500KDS
R	50 Ω ±10%
P_{diss}	100 W†
E_{max}	27 kJ

negligibly small under the worst-case scenario (100 mW) [9].

Diodes were installed on the power-supply side of the isolation resistor to prevent reverse transients from propagating to the power supply. Reverse transients can result in power supply failure in the worst-case scenario, or output voltage instability under rep-rate conditions [10]. The specifications for the diodes utilized are provided in Table 2-4 [11]. To obtain a safe voltage rating, three diodes were used in series, as indicated in Figure 2-2. The in the worst case, the reverse current is merely transitory in nature, and so the average reverse current is much less than the average forward current. The diodes

Table 2-4. Power supply reverse transient diode specifications. †Half-sinusoid, 8.3 ms duration.

Manufacturer	High Voltage Components Assoc.
Part Number	HVR-1X-30B
V_{PIV}	12 kV
$I_{F,avg}$	500 mA
$I_{F,peak}$	30 A†

are rated to handle more than the forward average current, so average current was not considered an issue.

The diodes were operated with parallel resistors to improve turn on time by equally biasing each diode to 1/3 of the applied voltage. The resistors specifications are summarized in Table 2-5 [12]. The resistors featured low-inductance construction techniques and were sized to provide ample voltage tracking distance. Each resistor dissipates 1.4 W when 25 kV is applied to a string of three series resistors.

Table 2-5. Summary of diode bias resistor specifications.

Manufacturer	Caddock
Part Number	MX450
R	150 MΩ ±1%
P_{diss}	5 W

2.1.3. Thyratron and Thyratron Control

The modulator was switched with a hydrogen thyratron switch. The hydrogen thyratron, or thyratron, is a controlled plasma closing switch that consists of an anode, a cathode, and control grids. The cathode temperature is controlled by an external power source. Fast-rising voltage pulses applied to the grid accelerate electrons generated at the cathode towards the anode. A conducting plasma column forms 10's of nanoseconds after the application of the grid voltage pulses and establishes the complete closure of the switch. The thyratron remains conducting until the magnitude of the current can no

longer sustain the plasma discharge, at which time the switch becomes an open circuit [13, 14].

The hydrogen thyratron utilized for the modulator is the English Electric Valve (now e2vtechnologies) CX1625AS hollow-anode hydrogen thyratron. The CX1625AS is a metal-envelope pentode capable of holding off up to 35 kV and conducting up to 15 kA. The specifications for the CX1625AS are summarized in Table 2-6 [15]. Simulations of the modulator indicate a peak current of up to 11 kA at a charge voltage of 25 kV was expected. The average value of the current was computed for a number of conditions and at no time did the value exceed about 2.5 A under a repetition rate of 20 pps and a peak charge voltage of 25 kV.

Table 2-6. Specifications for the hydrogen thyratron.

Manufacturer	English Electric Valve
Part Number	CX1625AS
Voltage Holdoff	35 kV
Peak Current	15 kA
Average Current	5 A

The thyratron is initiated by applying voltage pulses to the control grids. The manufacturer has determined that to obtain the lowest jitter, a double-pulse triggering scheme should be utilized [13]. In the double-pulse scheme grids 0 and 1, shown in Figure 2-3, are tied together through a current divider network, while Grid 2 is independently driven. The characteristics of the two pulses that provide the best jitter performance over a wide range of ambient conditions are summarized in Table 2-7. Following the application of the grid 2 pulse, grid 2 receives a negative voltage to aid

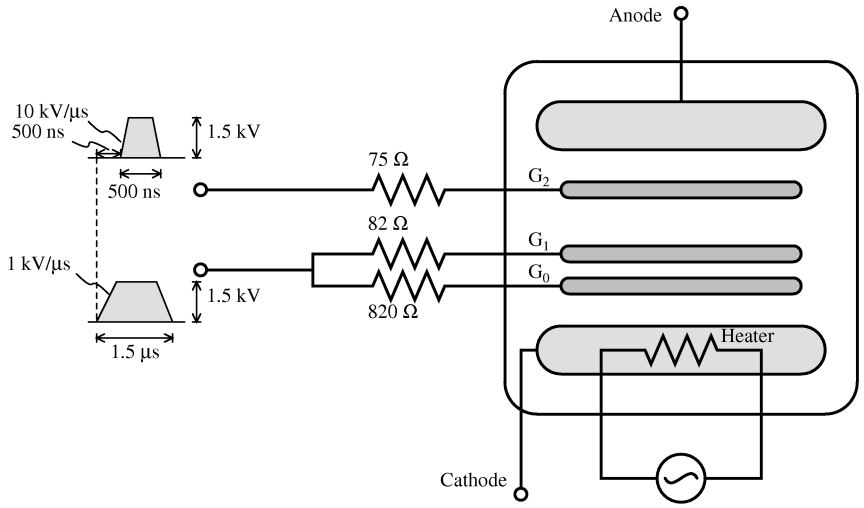

Figure 2-3. Internal connections and trigger pulse characteristics of the thyratron.

recovery following the main discharge. The trigger pulses were generated by a commercially available thyratron trigger specifically designed to drive pentode tubes.

Table 2-7. Trigger pulse characteristics of the thyratron trigger generator.

Parameter	Grid 0/1	Grid 2
Voltage Amplitude, kV	1.5	1.5
Driver Impedance, Ω	75	75
Pulse Length, µs	1	0.5
Pulse Delay, µs	0	0.5
Pulse Front dV/dt, kV/µs	1	10

2.1.4. Snubber Circuit

The snubber is composed of the series resistor-diode network shown in Figure 2-1. The circuit is designed to mitigate the negative current pulses generated by the test switch discharge. The reverse current results when the test switch fires either before or after the PFL voltage reaches peak in the charge cycle. The late or early switch-out of the DVT switch can result in capacitor bank reversal. Large reverse current flow is detrimental to the thyratron switch and the capacitor bank. The thyratron has been designed to handle modest current reversal, however the reverse current does add to the total RMS current,

which affects tube heating under rep-rate conditions. The capacitors may also be damaged if the magnitude of the current reversal results in a voltage reversal on the order of 15% of the peak charge voltage [4]. A simple and reliable snubber was therefore added to the modulator to protect the capacitors.

The snubber utilizes a series of Unitrode 1N5603 diodes stacked to obtain a peak reverse blocking voltage of 35 kV. A summary of the diode specifications is provided in Table 2-8 [16]. The 1N5603 is designed for high-voltage rectification applications but has been found to perform satisfactorily under pulsed conditions. Because the highest average current occurs when the test switch fires either earlier or later than the peak of the PFL charge voltage, the average current through the diodes was estimated with circuit simulations for a range of early breakdown conditions, from 65% of peak to 100% of peak, as well as a fault condition that occurs if the switch misfires.

Table 2-8. Snubber diode specifications for individual diodes.

Manufacturer	Microsemi Corp.
Part Number	1N5603
V_{piv}	5 kV
$I_{fwd,avg}$	5 A
$I_{fwd,\ peak}$	200 A, 8.3 ms
V_{on}	10 V
C_{jo}	40 pF max.

The peak diode current, indicated by $I_{fwd,peak}$ in Table 2-8, applies to AC sinusoidal current waveforms and must be scaled to obtain peak pulsed current under different conditions. The peak current is most easily scaled by applying the relationship found in equation (2.6), in which I is the peak current, in amperes, for a sinusoidal pulse duration of t seconds [17]. The ideal peak current the diodes can tolerate under a 2.5 μs sinusoidal pulse was estimated by utilizing $I_{fwd,peak}$ from Table 2-8 and t = 8.3 ms and is well above

the fault current that the diode must handle. When non-idealities such as doping gradients are considered, the estimated peak current must be reduced considerably, however the diodes are expected to be able to handle the peak current delivered.

$$I^2 t \simeq const. \qquad (2.6)$$

The average snubber diode current must remain below the device average current limit. An argument similar to the one presented for average thyratron current will be utilized to show the average current to be less than the device limit. The average reversal current flowing in the modulator is significantly less than the average forward current in the modulator, which is about 405 mA at 20 pps. The diodes are rated to handle the full forward average current, therefore the diodes are capable of safely operating at any conceivable reverse current while the modulator is operating at 20 pps.

The diodes operate in series with a 1.4 Ω load resistor utilized to dissipate the reverse pulse energy. The resistor is composed of two series 0.7 Ω disc resistors, clamped between aluminum plates to increase power dissipation capacity. The peak voltage across the resistors is voltage-flashover limited, while the peak current is energy limited. Due to the low expected peak voltages across the resistors and the very low energy (with respect to the peak energy capacity), the average power dissipation is the only rating that must be considered. The resistor specifications are summarized for a single resistor in Table 2-9 [18].

Table 2-9. Snubber resistor specifications for individual resistors.

Manufacturer	HVR Advanced Power Components
Part Number	W1528A070J
Resistance	0.7 Ω ± 5%
Outer Diameter	152 mm
Inner Diameter	26 mm
Height	25.4 mm
P_{diss}, 40 °C	2.5 W·cm^{-2}
E_{max}	110 kJ

Power dissipation in the resistors was analyzed utilizing circuit simulations at the same time that average diode current was estimated. The peak power dissipation within the resistors was found to occur at the earliest test switch breakdown as expected. The total power dissipation, computed with the RMS of the simulated current waveforms, was about 1 to 2 kW depending on how early the test switch was allowed to break down. The total exposed area of the resistors was sufficient for approximately 100 W of continuous dissipation. The 100 W rating was increased by installing a fan to blow directly across the resistors at all times. The fan limits the temperature excursions to about 30 °C during bursts of 1,000 shots, as measured with an infrared thermometer.

2.1.5. Safety and Control

The modulator stores energy in low-loss high voltage capacitors. The capacitors are able to retain stored charge for a long time following disconnection from the power supplies. A shorting relay was therefore installed to reduce the likelihood of personnel injuries associated with high voltage capacitor discharges. The relay is a Ross EA-40NC relay that is rated for 40 kV holdoff in typical ambient conditions (air at 70 °F and a relative humidity < 75%) [19]. The relay is a fail-safe relay that will snap shut if the control panel is either turned off or suddenly loses power. A schematic diagram of the relay placement is provided in Figure 2-4. The relay operates into two parallel 15 Ω wire-

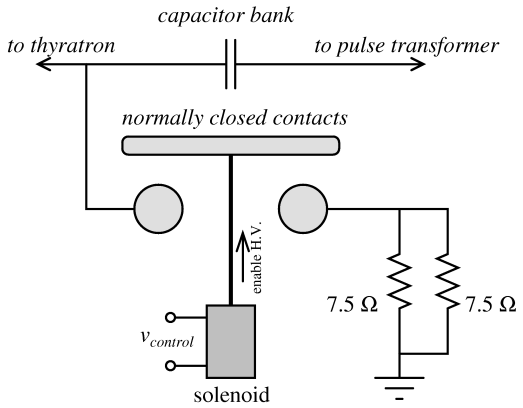

Figure 2-4. Safety relay circuit. Contacts are opened when a control signal is supplied to the solenoid.

wound resistors to prevent capacitor bank reversal when the capacitors are discharged [20].

A number of modulator functions are controlled remotely from a control panel. The panel utilizes a series of toggle switches to provide current to remote relays from a small D.C. power supply. Relays are utilized to control the thyratron fan, snubber resistor fan, and the core reset power supply, in addition to the Ross high-voltage relay. The control panel also converts TTL trigger pulses into optical pulses that the thyratron trigger generator utilizes for control. The TTL trigger pulses are additionally used to increment a pulse counter. Finally, a remote interface to the power supplies is operated from the control panel.

2.2. Pulse Transformer

The pulse transformer is utilized to convert the input low-voltage modulator pulse into a high-voltage output across the terminals of the pulse forming line. The pulse transformer additionally provides the resonant inductance required to complete the CLC charging network topology. The pulse transformer uses a magnetic core to increase the coupling efficiency of the windings. A core reset winding and D.C. current supply circuit

is utilized to reduce the magnetic material requirement by operating the magnetics in all four quadrants of the B-H loop.

2.2.1. Magnetic Core

A magnetic core is utilized to concentrate magnetic field lines and increases the coupling efficiency of a transformer. The magnetic material utilized for the cores is Metglas 2605CO, a material commonly utilized for pulse transformers. The magnetic properties of the material are summarized in Table2-10 [21].

Table 2-10. Magnetic properties of the pulse transformer core material.

Manufacturer	Allied Signal
Material	Metglas 2605CO
Saturation Flux (B_S)	1.0 T
Remanent Flux (B_R)	0.95 T
Coercive Force (H_C)	80 $A \cdot m^{-1}$

The magnetic core of the pulse transformer, shown in a photograph in Figure 2-5, is actually composed of four separate cores. The performance of the pulse transformer as a true transformer depends heavily on whether the magnetic material saturates. Solving the

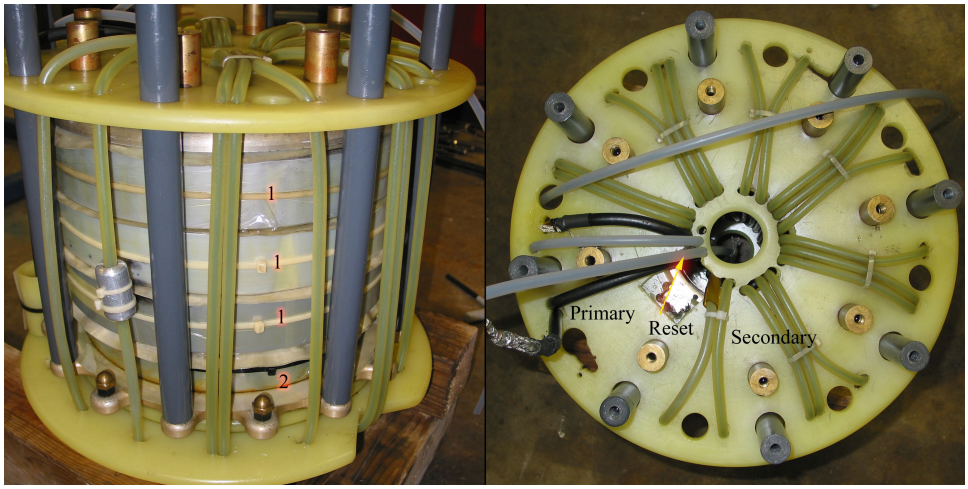

Figure 2-5. Photograph of the pulse transformer. (*left*) Cores are labeled based on the two sizes. (*right*) Windings are indicated in top view.

Faraday law of induction results in equation (2.7), which can be utilized to evaluate magnetic saturation [22]. The geometry of the magnetic material was evaluated in order to estimate the volt-seconds withstand (*i.e.* the right hand side of equation (2.7)) of the magnetic core. The dimensions of equation (2.7) are v volts, dt seconds, N turns, B in Tesla, and dA in m^2. Table 2-11 provides a summary of the dimensions and computed withstand volt-second product.

$$\int v dt = N \int B dA \qquad (2.7)$$

Table 2-11. Geometry and volt-second analysis of the magnetic core. †Estimated. ‡Per individual core.

	Size 1	Size 2	Total
Outer Radius, cm	17.78	15.24	—
Inner Radius, cm	6.35	6.35	—
Height, cm	5.94	5.94	—
Stacking Factor†	0.8	0.8	—
Number of Cores	3	1	—
Magnetic Length, l_m, cm	69.75	65.80	65.80
Magnetic Area, A_e, $cm^{2‡}$	40.72	31.67	153.83
Volt-Seconds Withstand, mV·s‡	16.288	12.668	61.53

The volt-seconds withstand, provided in Table 2-11, suggests a maximum volt-second product (*i.e.* the left-hand side of equation (2.7)) at which the magnetic core saturates. The voltage waveform developed across the primary, integrated with respect to time, gives a volt-second product of 31.3 mV·s when the PFL just becomes fully charged. The volt-second product is found to be less than the volt-second withstand given in Table 2-11, therefore the magnetic core remains linear during the pulse, provided the magnetic flux excursion is twice the saturated magnetic flux density, B_S, given in Table 2-10.

2.2.2. Transformer Model

The transformer was modeled as an equivalent circuit in Spice simulations. The equivalent T-model of the pulse transformer in Figure 2-6 is an ideal transformer and the remaining parameters model the non-ideal effects observed in the laboratory [23]. The leakage inductance is estimated utilizing the technique described in Section 2.1.1 where the capacitor bank was allowed to ring through the pulse transformer and the resultant

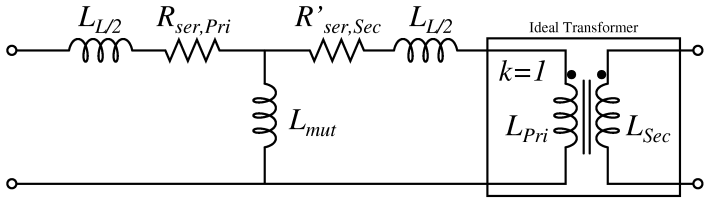

Figure 2-6. Schematic diagram of the equivalent-T pulse transformer model utilized in the analysis of the test stand.

period was measured.

Based upon an actual measurement of the leakage inductance an initial first-order model of the system was built and analyzed to determine rough parameters. Following a series of test shots utilizing the capacitor ring-through method, the inductance was calculated utilizing known capacitor bank and PFL capacitances and the measured oscillation period. The equivalent capacitance of the parallel 810 nF capacitor bank and the 738 nF PFL (transformed to the primary side of the pulse transformer) is 386.2 nF, and the measured charge time is 2.547 μs. Substitution of these values into equation (2.2), where $2t_{charge} = T = 2\pi/\omega_0$, yields a leakage inductance of 1.703 μH, as already indicated in Section 2.1.1. The complete model parameters indicated in Figure 2-5 are summarized in Table 2-12.

Table 2-12. Summary of the pulse transformer inductances. †L_{leak} estimated in the text. ‡L_{mut} estimated utilizing Eq. (2.8).

L_{pri}	76.1 µH
N_P/N_S	10
L_{sec}	7.61 mH
L_{leak}	1.703 µH
L_{mut}	75.2 µH
k_T	0.98881
$R_{ser,Pri}$	15.88 mΩ
$R_{ser,Sec}$	158.8 mΩ

The series resistance and mutual inductance were evaluated to determine the remaining parameters of the transformer model. The mutual inductance, also called the magnetizing inductance by some authors, is evaluated numerically with equation (2.8), where $L_{leak/2}$ is half the leakage inductance and k_T is the coupling coefficient of the pulse transformer [23]. The series resistance of the windings is estimated with equation (2.9), where the term n is the number of integer turns, l_T is the length of a single turn (estimated at 5 feet), and ρ is the per-unit-length resistance of the equivalent 12 AWG winding (about 1.588 mΩ·ft^{-1}) [23].

$$L_{mut} = L_{leak/2}\frac{k_T}{1-k_T} \qquad (2.8)$$

$$R_{ser} = nl_T\rho \qquad (2.9)$$

2.2.3. Core Reset

The magnetic core utilized in the pulse transformer was found to remain linear based upon the assumption that the magnetic flux density excursion during the modulator discharge was twice the saturation flux density, or $2 \cdot B_S$. Direct-current magnetic core reset is employed to drive the transformer core into reverse saturation. The core reset circuit utilizes a low-voltage D.C. current supply, a pulse filter network, and an auxiliary winding on the pulse transformer core. The polarity of the voltage applied to the reset

winding was determined by measuring the PFL voltage under positive and then negative polarities; saturation was observed under one polarity, and not under the opposite polarity.

The current requirements for D.C. core reset are easily established by analyzing the integral form of Ampere's law. Ampere's law, following integration and algebraic manipulation, yields equation (2.10), which gives the relationship between magnetic field strength, H in $A \cdot m^{-1}$, current, i in amperes, the magnetic path length, l_m in meters, and the number of turns, n [22]. Substituting values of $H = H_c = 80$ Am^{-1}, $l_m = 0.6580$ m, and $n = 2$, the minimum current required to drive the core into saturation in one quadrant is 26.3 A.

$$i = \frac{Hl_m}{n} \qquad (2\text{-}10)$$

The core reset power supply generates a D.C. current into the auxiliary 2-turn winding added to the pulse transformer. The winding will be pulse-charged to 25 kV when the modulator fires. A pulse-blocking circuit was developed and fabricated to prevent the pulse energy from damaging the power supplies. A schematic diagram of the pulse blocking circuit is provided in Figure 2-7 below, in which a three-stage RLC network is employed to gradually reduce the high-voltage pulses to levels that will not result in damage to the power supplies.

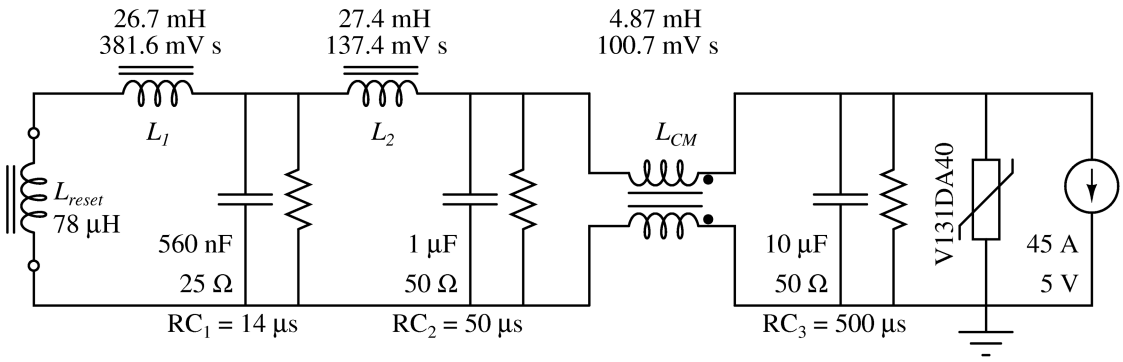

Figure 2-7. DC Core reset circuit schematic. Power flow is from right to left.

2.3. Full System Simulations

A full model of the modulator, pulse transformer, pulse forming line, and equivalent output of the load was simulated in LTSpice. Equivalent models were employed for the pulse transformer, the test switch, and the load resistor. A complete schematic diagram of the circuit simulated is presented in Figure 2-8. The netlist that corresponds the circuit in

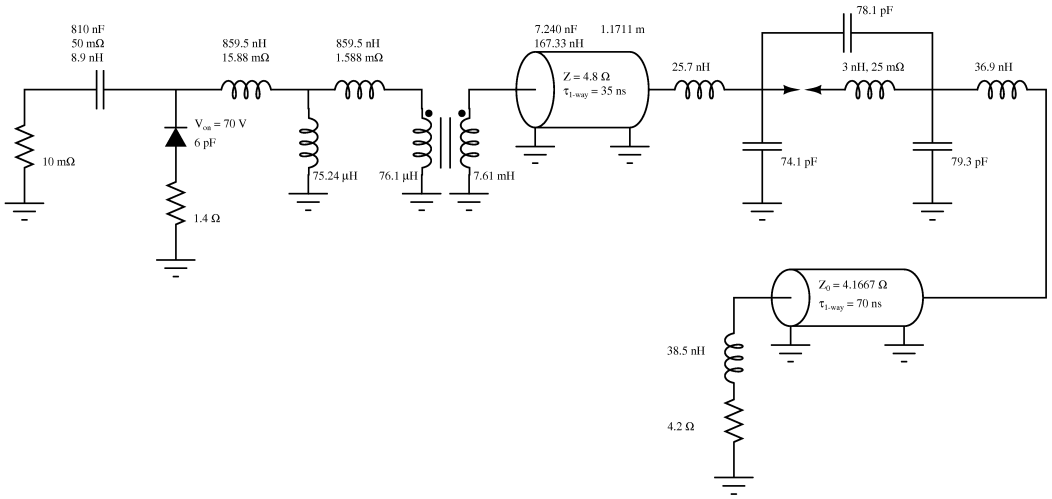

Figure 2-8. Schematic diagram of the circuit simulated within LTSpice. Parasitic elements, when included, appear below the nominal element value.

Figure 2-8 may be found in Appendix A.

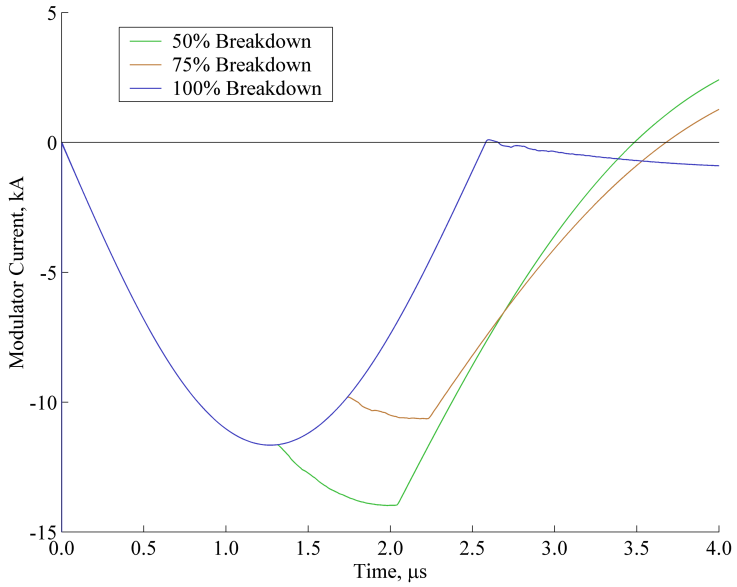

Figure 2-9. Simulated modulator current for three levels of breakdown voltage.

The modulator performance was analyzed to determine peak, average, and RMS current through the thyratron and capacitor bank, and average snubber current. The average and RMS values were expected to vary depending upon when the test switch breaks down, so several scenarios were simulated to verify that continuous operation at 20 pps would not significantly impact the snubber or thyratron. Simulations were performed for test switch breakdown at 50%, 75%, and 100% of the peak charge voltage and the resulting current waveforms are plotted in Figure 2-9. The simulations show that when the switch fires early there is an increase in the forward current through the capacitor bank and thyratron—this current contributes to the average current through the thyratron and the RMS current through the capacitors. The 100% breakdown waveform represents the idealized case, where magnitude of I_{peak} was found to coincide with the theoretical value of 11 kA.

The snubber current was simulated to verify the average current through the diodes, and the RMS resistor current, remained at safe levels. The waveforms plotted in Figure 2-

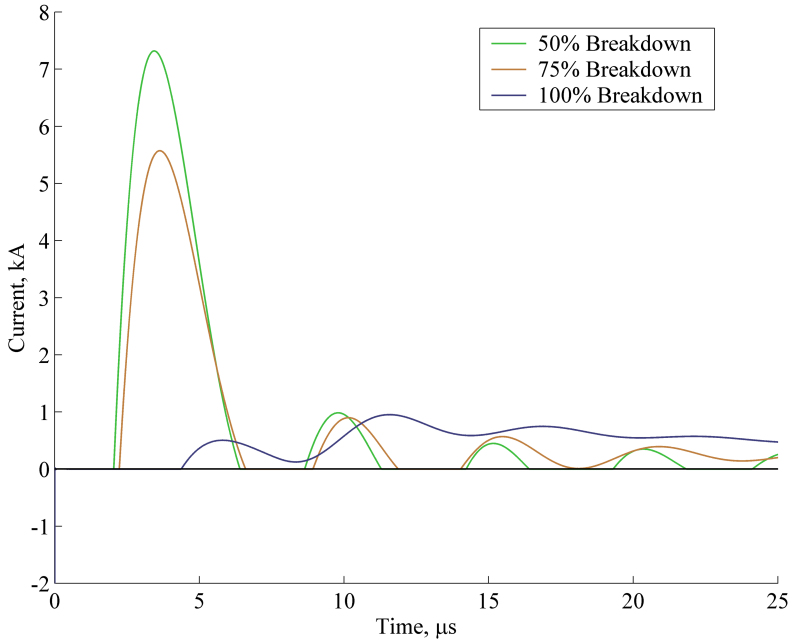

Figure 2-10. Simulated snubber current amplitudes for three levels of breakdown voltage.

10 suggest the peak current, which attains a maximum value of 7.3 kA for the 50% breakdown scenario, remains at safe levels for the diodes. The average and RMS current values were found to be within specification limits, provided the resistors are given a brief cool-down period following a long burst of shots.

The voltage developed on the pulse forming line was simulated to enable estimates of the peak voltage, peak dV/dt during the charging interval, and post-pulse characteristics of the pulse forming line voltage. The waveforms from three simulations are shown in Figure 2-11. The time to peak voltage is 2.547 µs, as determined from the estimate of the resonant frequency described in 2.1.1. The capacitor bank is initially charged to 25 kV, and the peak voltage at the end of the charge cycle is about –245 kV. The transients on the PFL following the end of the discharge appear to increase in magnitude as the percent-breakdown increases to 100%.

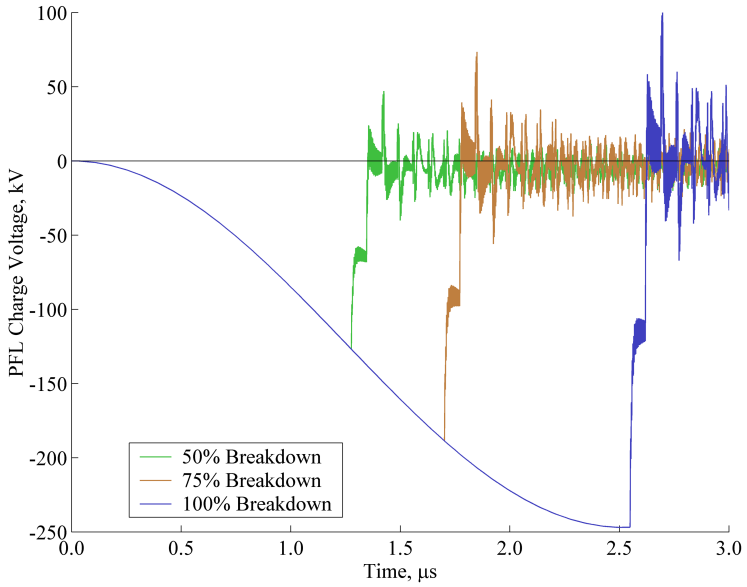

Figure 2-11. Voltage waveform on the pulse forming line for three different levels of test-switch breakdown.

The load voltage simulation is presented in Figure 2-12. The load resistor was designed as a low-inductance resistor. The effective inductance of the load will be shown in a later chapter to be equivalent to 38.5 nH at the equivalent frequency of the pulse expected from the switch (τ_{rise} ~ 15 ns) in series with 4.2 Ω. The oscillations that appear

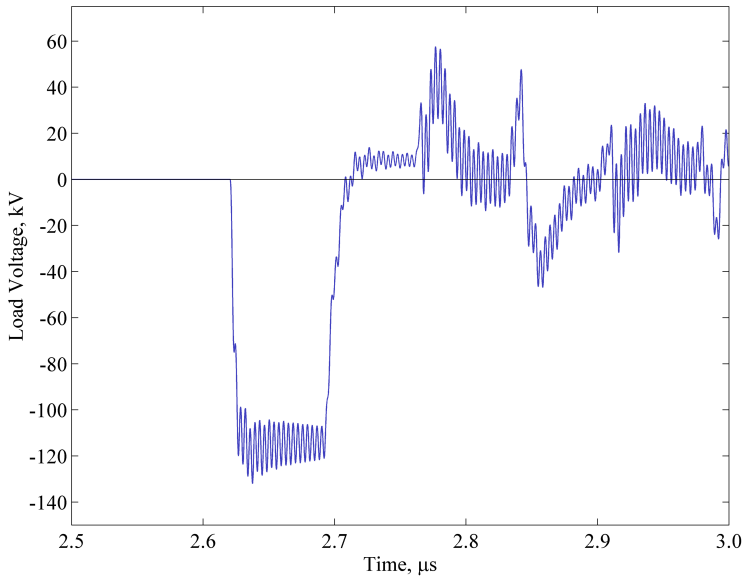

Figure 2-12. Simulated load voltage for breakdown at 100% of the peak PFL voltage.

superimposed upon the waveform (f = 288 MHz) are the result of the complex network of inductance and capacitance in the oil switch model and are not the result of the load. A number of large amplitude reflections are observed which are the reflections of the pulse propagating back and forth across the high-voltage cables.

The simulated load current is presented to show the effects of the load impedance on the pulse characteristics. The load current waveform, presented in Figure 2-13, shows a much slower leading edge rise time than the voltage waveform exhibited—this is believed to be due to the inductive nature of the effective load impedance. The inductance, in concert with the series resistance, also effectively removes by integration the great majority 288 MHz noise that was observed on the voltage waveform. The simulated current rise time into a 38.5 nH inductance in series with a 4.2 Ω resistor is approximately 20.4 ns (10-90), which agrees with the design calculations of 20.2 ns.

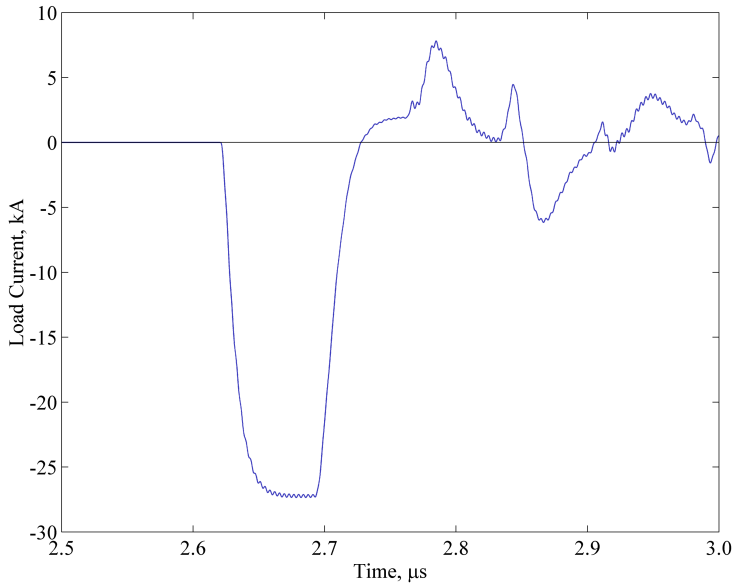

Figure 2-13. Simulated load current into a series R-L load, for breakdown at 100% of the peak PFL voltage.

2.4. Performance Verification Measurements

A number of waveforms were measured from the modulator and pulse forming line to verify system operation. Diagnostics, which will be described in greater detail in Chapter 4, were placed in key locations within the modulator and PFL to measure system performance.

Two modulator current waveforms were recorded with a current transformer and are presented in Figure 2-14. The waveforms were recorded when the switch fired at 88.6 % and 99.5 % of the peak voltage on the pulse forming line. The peak current amplitude attained in both cases is 6 kA. There was a high-frequency component superimposed upon the crest of the main current pulse in all waveforms recorded that is due to the fact that the modulator discharges into a series of paralleled high-voltage cables that connect the modulator to the primary winding of the pulse transformer. The leading edge spike is due to the rapid charging of the snubber diode junctions and is easily simulated by

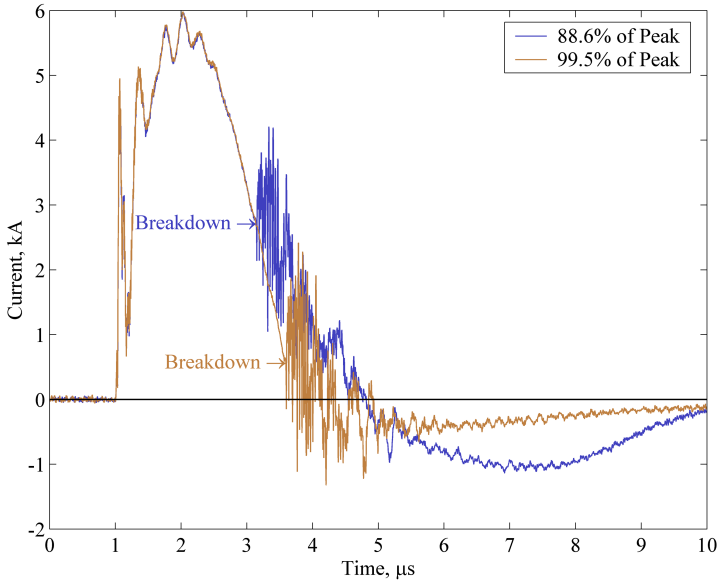

Figure 2-14. Measured modulator current waveforms. The percentage recorded refers to the percent of the peak voltage at which breakdown occurred.

including diode junction capacitance in the LTSpice model. A current reversal with a 1 kA magnitude is seen for the early breakdown case (88.6 % of peak).

The charge voltage on the capacitor bank was monitored under rep-rate conditions to determine the peak repetition frequency that could be utilized for testing. The voltage presented in Figure 2-15 was measured at the anode terminal of the capacitor bank, with respect to ground. The modulator was operated at a repetition rate of 10 pps and the power supplies were set to provide 23.8 kV. The voltage is observed to rise linearly until the capacitor bank is nearly fully charged. The voltage next increases very slowly, indicating that more and more of the power supplies are current limiting until finally at approximately 50 ms after the pulse discharge was initiated the voltage has attained a steady-state value. The charging interval of 50 ms suggests the peak repetition rate to attain the steady-state voltage is 20 pps. The power supplies are therefore providing about 4.66 kW average power.

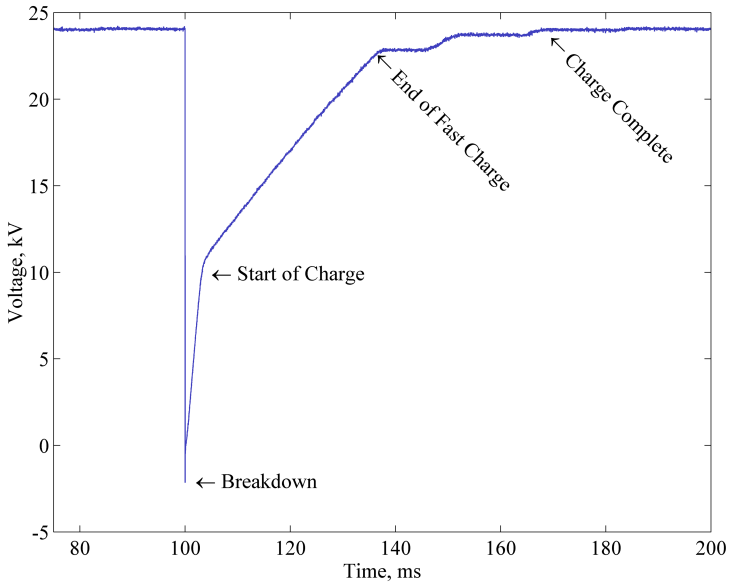

Figure 2-15. Capacitor bank voltage at 10 pps and 23.8 kV charge voltage.

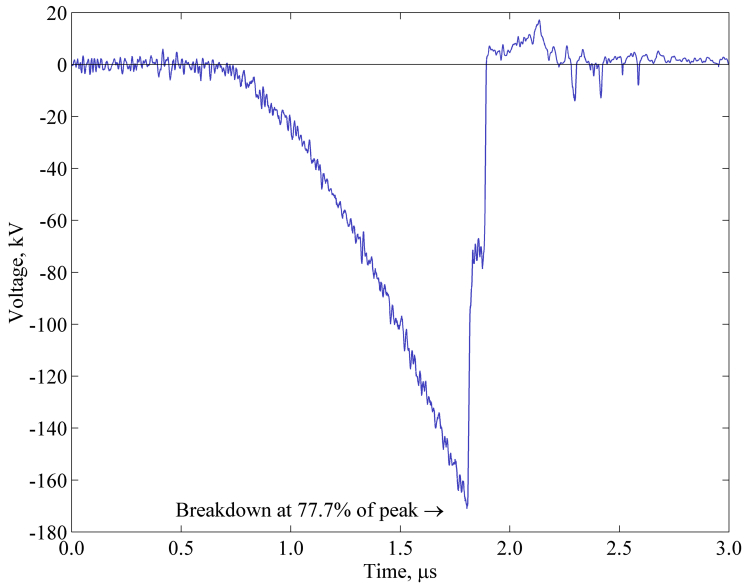

Figure 2-16. Pulse forming line voltage during a charging interval.

The pulse forming line voltage is measured at the switch cathode with a high-performance D-dot probe. The D-dot probe output drove a 2 µs passive integrator, and the output from the integrator was recorded. The recorded waveform shows many of the characteristics predicted by the simulation found in Figure 2-11, including post-pulse noise. A typical PFL voltage waveform is presented in Figure 2-16 in which breakdown took place at 77.7 % of the peak charging voltage, or -171 kV. The modulator was provided with a 22 kV charge voltage for the waveform plotted in Figure 2-16. The post-pulse noise is due to a minor impedance mismatch at the load resistor.

The voltage delivered to the output transmission lines is measured with a self-integrating capacitive monitor. A measured output voltage waveform is presented in Figure 2-17. The rise time of the output voltage pulse was determined to be about 15 ns, which is 5 ns slower than the simulated value. The complex geometry associated with the test switch and the transmission line connections may have introduced some additional inductance that was not accounted for in the simulations.

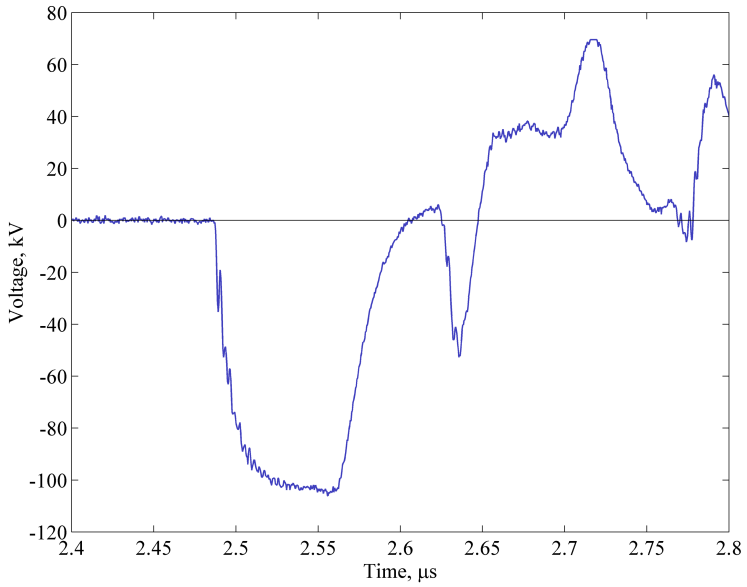

Figure 2-17. Output voltage pulse measured on the high-voltage transmission lines that connect between the switch and the load resistor.

The simulations predict most of the major behaviors exhibited by the modulator, transformer, and pulse forming line. Some additional parasitic elements have been identified that could be added to the modulator model. The overall response of the circuit model was not found to change significantly when the additional elements were added, however.

2.5. References

[1] G. W. Ewell, "*Radar transmitters*," McGraw-Hill Book Co., New York, 1981, pp. 87 – 91.

[2] J. Millman and H. Taub, "*Pulse, digital, and switching waveforms*," McGraw-Hill Book Co., New York, 1965, pp. 1 – 4.

[3] W. E. Boyce and R. C. DiPrima, "*Elementary differential equations and boundary value problems, 6th Ed.*," John Wiley and Sons, New York, 1997, pp. 121 – 137.

[4] Data sheet, *Capacitor specification, model number 31663*, General Atomics Energy Products, 2002.

[5] R. J. Tallarida, "*Pocket book of integrals and mathematical formulas, 3rd Ed.*," Chapman & Hall/CRC Press LLC, Boca Raton, 1999, pp. 95 – 98.

[6] M. Sadiku, "*Electromagnetics, 2nd Ed.*," Oxford University Press, New York, 1995, pp. 518 – 530.

[7] F. R. Bergseth and S. S. Venkata, "Introduction to electric energy devices," Prentice Hall Inc., Englewood Cliffs, 1987, pp. 89 – 93.

[8] Data sheet, *ALE 302 operators manual*, ALE Inc., Boston, 1985.

[9] Data sheet, *Type 889AS tubular resistor product data sheet*, Kanthal-Globar Inc., Niagra, 2002.

[10] Application Note, *Voltage reversal protection*, Lambda-EMI Inc., App. Note 517, Boston, 2002.

[11] Data sheet, *HVR-1X standard recovery high current diodes*, High Voltage Components Associates Inc., Farmingdale, 2002.

[12] Data sheet, *Type MX precision high voltage resistors*, Caddock Electronics Inc., Riverside, 2004.

[13] Application note, *Hydrogen thyratrons*, e2v Technologies Ltd., Chelmsford, 2002.

[14] K. Henney, "*Electron tubes in industry, 2nd Ed.*," McGraw-Hill Book Co., New York, 1937, pp. 24 – 55.

[15] Data sheet, *CX1625 air cooled, hollow anode, metal/ceramic pentode thyratrons*, e2v Technologies Ltd., Chelmsford, 2002.

[16] Data sheet, *Rectifier assemblies, high voltage stacks, 1 amp to 5 amp, military approved*, Microsemi Inc., Irvine, 2003.

[17] Application Note, *SCR/GTO/Diode ratings and characteristics*, Powerex Inc., Youngwood, pp. 20 – 21.

[18] Data sheet, *High energy disc resistors*, HVR Advanced Power Components Inc., Tonawanda, 2003.

[19] Data sheet, *EA series relays*, Ross Engineering Co. Campbell, 2002.

[20] Data sheet, *270 series vitreous enamel power resistors*, Ohmite Manufacturing Co., Rolling Meadows, 2001.

[21] Data sheet, Metglas magnetic properties, Allied Signal Inc., Parsippany, 1996.

[22] *i.b.i.d.* Sadiku, pp. 289 – 322.

[23] G. N. Glasoe and J. V. Lebacqz, "Pulse generators," McGraw-Hill Book Co., New York, 1948, pp. 335 – 354.

Chapter 3. Water Pulse Forming Line and High Voltage Load

An existing water pulse forming line was modified to generate fast, high-voltage pulses into a series of output cables. The high-voltage output cables drove a high-power flowing load resistor designed to absorb the pulse forming line (PFL) output energy. The PFL is charged to -250 kV in about 2.55 μs and, when switched into the output cables through the test switch, generates a -125 kV, 70 ns pulse. The output cables connect the output of the DVT switch to the load resistor.

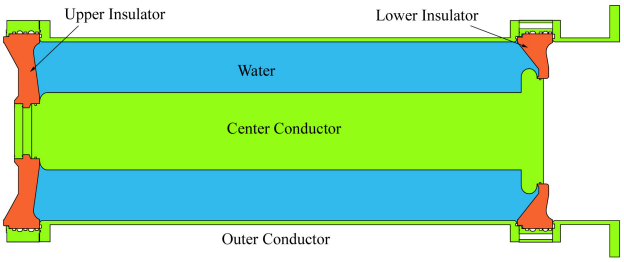

Figure 3-1. PFL cross section showing the location of insulating bushings (insulators).

3.1. Water Pulse Forming Line

The water PFL was refurbished and modified to suit the requirements of the high-pressure test switch program. The PFL refurbishment included a redesign of the upper and lower insulating bushings and a complete electrostatic simulation analysis. The simulated electric fields were compared to flashover criterion to ensure that the insulators would provide a long, flashover-free service life. A scale cross-section of the water PFL is presented in Figure 3-1.

3.1.1. Electrical Analysis of the PFL

The water PFL is a simple coaxial structure, constructed of stainless steel, that utilizes the dielectric properties of water to store electrical energy within the electric fields [1].

Table 3-1. Measured dimensions of the water pulse forming line.

Inner Diameter	20.8 cm
Outer Diameter	42.5 cm
Length	1.171 m
Dielectric Constant	$80\varepsilon_0$

The PFL structure has the dimensions given in Table 3-1. The impedance of the PFL was estimated based on equation (3.1), where the impedance in Ω is related to the total capacitance in Farads, and the total inductance in Henries [2]. The capacitance was estimated with equation (2.5), where l is the length, r_o is the outer radius, r_i is the inner radius, ε_r is the dielectric constant of water, and ε_0 is the dielectric constant of free space (l, r_o, and r_i in meters, ε_0 in $F \cdot m^{-1}$, ε_r unit-less) [2]. The inductance was estimated with equation (3.2), where μ_0 is the permittivity of free space in $H \cdot m^{-1}$, and all other dimensions are as defined for the capacitance [2]. Utilizing the dimensions listed in Table 3-1 the total capacitance of the PFL is 7.245 nF, the total inductance is 167.3 nH, and therefore the PFL impedance is 4.8 Ω.

$$Z = \sqrt{L/C} \qquad (3.1)$$

$$L = \frac{\mu_0 l}{2\pi} \ln\left(\frac{r_o}{r_i}\right) \qquad (3.2)$$

The transit time of the PFL determines the pulse duration generated by the PFL according to equation (3.3). The pulse duration, τ_p in seconds, is defined as twice the propagation time of a D.C. charged transmission line system. The propagation time is the square root of the inductance times the capacitance, where the inductance is specified in Henries and the capacitance is specified in Farads [2]. Utilizing the values determined above for L and C, the pulse duration should be 69.6 ns, or about 70 ns.

$$\tau = \sqrt{LC} \qquad (3.4)$$

The PFL stores energy in the electric field set up within the water dielectric. The magnitude of the stored energy is calculated with equation (3.4), which relates the stored energy, E in Joules, to the total capacitance, C in Farads, and the terminal voltage, V in volts. Utilizing a charge voltage of 250 kV and a total capacitance of 7.245 nF the total stored energy within the PFL is about 226 J. Table 3-2 summarizes all of the important electrical specifications of the PFL.

$$E_C = \tfrac{1}{2} CV^2 \qquad (3.4)$$

Table 3-2. Electrical specifications of the water PFL derived from measured dimensions.

Inductance	167.3 nH
Capacitance	7.245 nF
Impedance	4.81 Ω
Pulse Duration	70 ns
Stored Energy	226 J
Charge Voltage	-250 kV

3.1.2. Electrostatic Analysis of the PFL

Electrostatic models of the water PFL were utilized to verify the PFL would have a low probability of surface flashover at the insulating bushings. As received, the insulating bushings had considerable damage that rendered them unusable. The bushings were carefully measured so that an electrostatic model could be developed to test design modifications prior to fabrication. A new pair of insulating bushings with design modifications incorporated were fabricated from new polycarbonate. Polycarbonate was selected as the replacement material because it is easily available in void-free form, it absorbs very low amounts of water (< 7%), is not subject to strong chemical attack by transformer oil or water, and is a mechanically strong polymer [3].

Long operational life was the main requirement for the bushings. The operational life of the bushings could be affected by changes in mechanical properties and changes in electrical properties. The old bushings did not indicate any signs of mechanical failure so only electrical properties limit the bushing lifetime. Electrical flashover, an arc discharge over the surface of an insulator, is particularly detrimental to bushing lifetime because the trail of carbon that is left behind on the plastic surface following a flashover can act as an initiation source for future flashovers. As can be verified in Figure 3-2 the previous insulators indicate obvious signs of cracking (believed to be due to age) and burn marks (believed to be due to arcs), as well as carbon tracks.

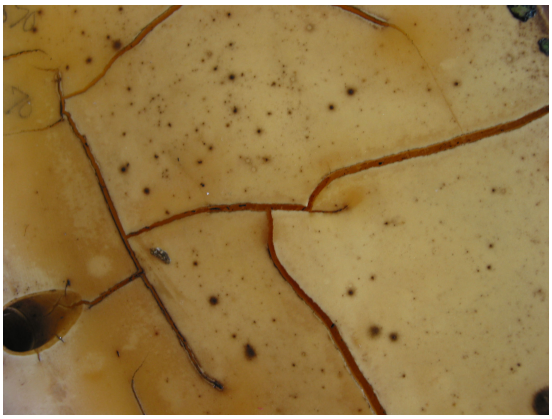

Figure 3.2. Photograph of the damaged insulator.

Electrical flashover along a liquid-solid interface is a phenomenon that has received considerable attention within the literature [4]. A function that relates applied electric field strength to the number of shots to failure and the breakdown electric field strength has been developed by Elizondo [5]. Equation (3.5) gives the maximum applied field strength, E_{ap} in kV·cm^{-1}, that can be applied to a dielectric with a breakdown electric field strength of E_b in kV/cm for a total of n cycles. Equation (3.6) provides E_b in MV·cm^{-1} as a function of field enhancement factor, f, the effective time of the voltage pulse, t_{eff} in μs, and the stressed area, A in cm^2. For the present analysis, t_{eff} is approximately 0.95 μs, A is

approximately 1090 cm^2, f is approximately 1.46, and the resulting E_b is about 380 $kV \cdot cm^{-1}$ [6]. The value for E_b is inserted into (3.5), and a value of 10^8 is inserted for n to obtain a value for E_{ap} of approximately 110 $kV \cdot cm^{-1}$. Therefore to limit the potential for flashover the electric field strength needs to remain below 110 $kV \cdot cm^{-1}$. Equation (3.6) was adapted from a large-area water dielectric application and represents a good first-order approximation of the maximum applied electric fields that just prevent breakdown for a given number of shots.

$$E_{ap} = E_b \left(\frac{2}{n} \right)^{0.07} \qquad (3.5)$$

$$E_b^- = \left(\frac{0.56}{t_{eff}^{0.333} A^{0.07}} \right) \left(1 + 0.12\sqrt{f-1} \right) \qquad (3.6)$$

Electrostatic simulations were performed for three separate cases representing ideal conditions, and two non-ideal conditions. In the ideal case the water dielectric was allowed to completely fill the interior of the PFL. In the two non-ideal cases, the interior was not allowed to be completely filled and both air and oil pockets at the top of the PFL were simulated.

3.1.2.1) Normal (Ideal) Operating Conditions

The ideal case simulations were performed with the PFL interior completely filled with water dielectric. Within the simulation dielectric constants of 80, 2.1 and 3.2 were utilized for the water, the transformer oil, and the Lexan (polycarbonate) bushings, respectively. The boundary conditions at the inner and outer conductor surfaces were specified such that -250 kV appeared on the PFL center conductor and the ground conductor was fixed at 0 V. The results of the simulation are presented in Figure 3-3.

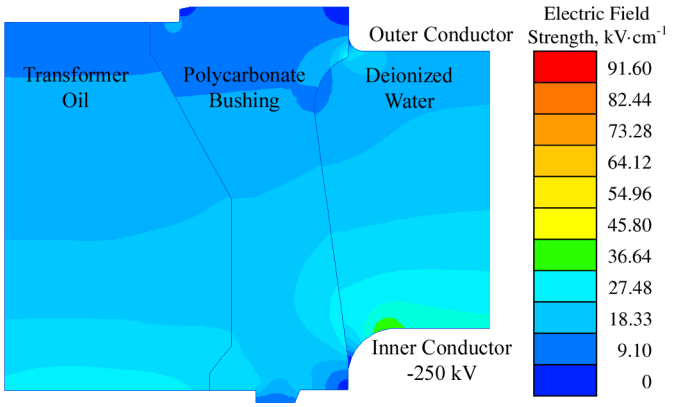

Figure 3-3. Simulated upper bushing electrical field strength under normal operating conditions.

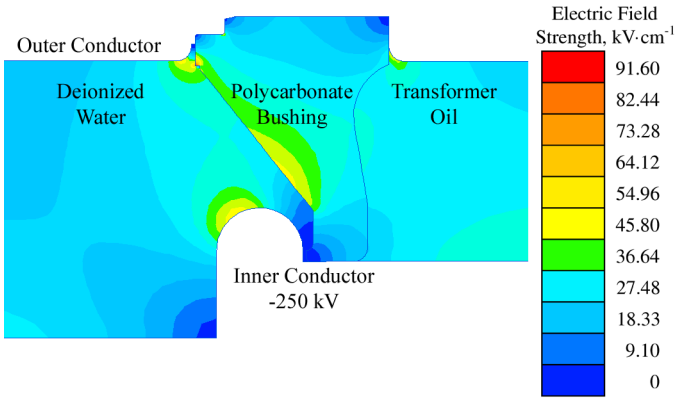

Figure 3-4. Simulated lower bushing electrical field strength under all conditions.

The simulation results in Figure 3-3 indicate that the upper bushing is not very highly stressed while simulation results in Figure 3-4 indicate much higher stress on the lower insulator. The peak electric fields are concentrated within the lower bushing and approach a peak strength of about 92 $kV \cdot cm^{-1}$ near the outer conductor. Within the bushing at the mid-point, the electric field strength remains lower than 50 $kV \cdot cm^{-1}$. The mesh-node densities near the high-stress singularities were increased to ensure the software computed the electric field magnitudes correctly. In both cases the electric field strength remains lower than the calculated threshold of 110 $kV \cdot cm^{-1}$.

3.1.2.2) Failure Mode: Air Pocket

The next case simulated included a small air pocket at the high point in the pulse forming line. The dielectric constant of the air pocket was assumed to be that of free space. Figure 3-5 shows the simulation results at the upper bushing, which indicates the field strength near and within the air pocket remains below about 20 kV·cm^{-1}. The breakdown strength of air at atmospheric pressure is about 30 kV·cm^{-1}. The simulations indicate a low risk of dielectric failure at or along the upper bushing.

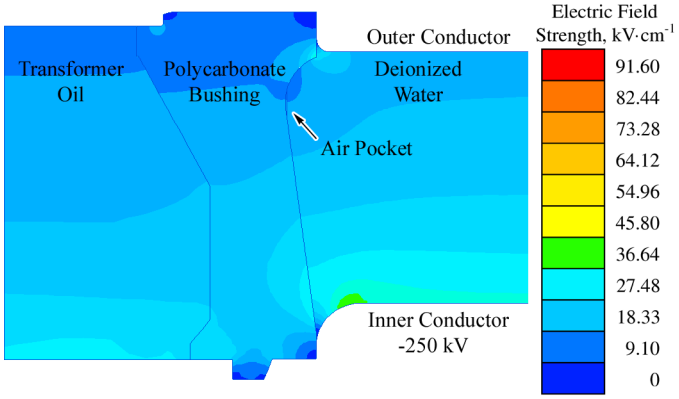

Figure 3-5. Simulated upper bushing electrical field strength with a trapped air pocket.

3.1.2.3) Failure Mode: Oil Pocket

The final case simulated included a small oil pocket at the high point in the pulse forming line. The dielectric constant of the oil was $2.1\varepsilon_0$ in the simulation. The simulation results, shown in Figure 3-6, reveal a situation nearly identical to the case involving the air pocket, with the electric field strength attaining less that 20 kV·cm^{-1} along the edge of the oil pocket.. The voltage holdoff of oil is considerably greater than that of air so the risk of a dielectric failure with a trapped oil pocket appears to be quite low.

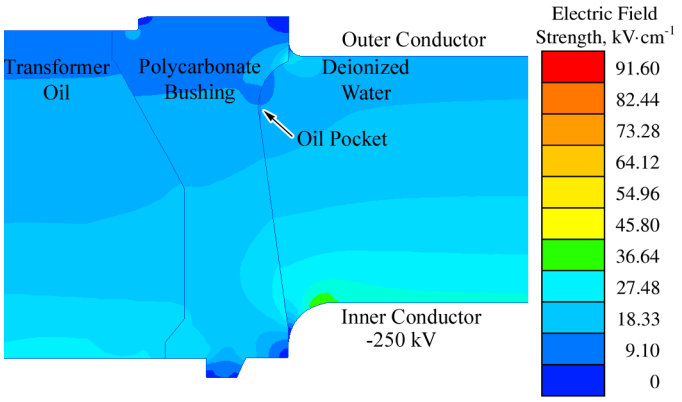

Figure 3-6. Simulated upper bushing electrical field strength with a trapped oil pocket.

3.1.3. Updated Bushings

Following a full analysis of the PFL bushings within the electrostatic simulator the updated bushing design was approved and then fabricated. A rendered image of the mechanical drawing for the upper bushing is provided in Figure 3-7 to show some of the design features incorporated into the new bushing. In Figure 3-7 the side of the bushing that faces water is shown. The water feed ports were machined at an offset angle to generate a vortex motion around the center conductor of the PFL. It is believed that this swirling motion would remove the trapped air at the top of the PFL. The stepped collar shelf is an improvement to help reduce compressive forces that the previous collar support inflicted upon the bushing.

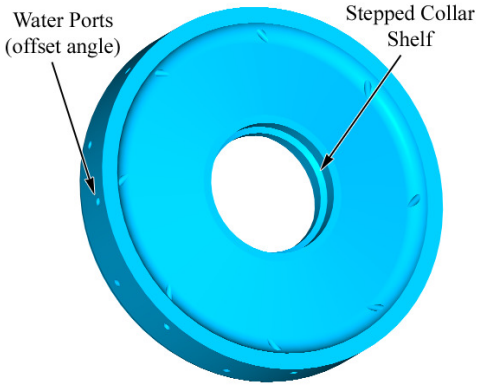

Figure 3-7. Rendered image of the upper insulator indicating the design improvements.

3.1.4. PFL Water Supply

The water used within the PFL as the dielectric medium has been deionized. The low conductivity of the deionized (DI) water is crucial to the efficient operation of the PFL. High conductivity water would allow the pulse energy delivered by the modulator to be dissipated and would result in pulse droop on the '$1-\cos(\omega t)$' charging waveform. The water deionizer maintains the supply of water at a resistivity of 5MΩ·cm at its outlet. The effective resistance across the PFL due to the water conductivity is approximately 440 kΩ, which results in less than 0.7% droop under the 2.547 μs applied pulse.

3.2. PFL Output Section

The high pressure switch discharges the pulse forming line into a series of twelve parallel high-voltage transmission line cables. The RG-218 cables each have a nominal impedance of 50 Ω and are 15.24 m in length [7]. The cables connect to the anode plate attached the switch through the spool that contains the switch, as indicated in Figure 3-8. The effective impedance of the twelve parallel transmission lines is 4.1667 Ω and the one-way transit time of the cables is 70 ns.

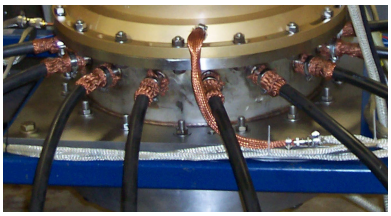

Figure 3-8. Photograph of the coaxial cable feed throughs.

A slight impedance mismatch exists between the PFL and the output cables. The degree of mismatch was characterized with transmission line reflection coefficients. Utilizing the definition of the reflection coefficient, $\Gamma = -0.0706$ at the interface between the PFL and the output cables [8]. The transmission coefficient at the interface is $1 + \Gamma =$

0.9294. Thus for a 250 kV charge voltage, the forward pulse amplitude along the transmission lines should be 116.2 kV.

3.3. High Voltage Load Resistor

The twelve parallel, high-voltage cables terminate into a high voltage load resistor. The load resistor is designed to have low inductive reactance for a fast current rise time. The resistor utilizes a water-copper sulfate mixture to achieve high conductivity, and a parallel plate topology to reduce inductance. The load resistor is shown in a photograph in Figure 3-9. The high-voltage input plates can be seen in the foreground of Figure 3-9; the ground plate is on top and the high-voltage plate is on bottom. The clear acrylic box holds the copper-sulfate solution and the electrodes, and two brass feed-throughs feed electrical power into the box. The tubes feeding into the left and right of the box provide the flowing copper-sulfate solution.

The electrical properties of the load resistor were estimated to verify the load was low inductance. The total model of the load resistor included inductances associated with feed plates, cable terminations, and the resistive element itself. The model also included significant capacitance associated with the parallel-plate construction topology. The resultant series-parallel resistor model was simplified utilizing complex impedance

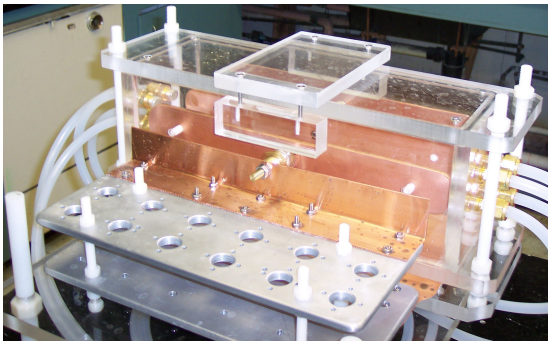

Figure 3-9. Photo of load resistor prior to installation in an electrically grounded drum filled with insulating oil.

analysis techniques. When all terms are simplified the resistor appears as a 4.198 Ω resistance in series with a 38.5 nH inductance. The *L-R* time constant of the resistor gives a 10-90 rise time of approximately 20 ns, which is about 5 ns greater than the expected rise time of the DVT switch.

The concentration of copper sulfate within the water-copper sulfate solution depends on the desired conductivity of the solution, which is related to the geometry and the desired resistance by equation (3.7). In (3.7) the conductivity σ, in $S \cdot cm^{-1}$, is related to the length of the resistor from plate to plate, l in cm, the cross sectional area of the conductive region, A in cm^2, and the desired resistance, R in Ω [9]. The dimensions of the resistor result in a length of 10.16 cm, an area of 387.1 cm^2, and the desired resistance is 4.2 Ω. Substitution of the numerical values for l, A, and R result in a conductivity of 6.3 $mS \cdot cm^{-1}$. The concentration of copper sulfate to water to achieve a conductivity of 6.3 $mS \cdot cm^{-1}$ is about 1 kg of copper sulfate to 114 liters of water [10].

$$\sigma = \frac{l}{AR} \qquad (3.7)$$

The thermal performance of the load resistor is stabilized by circulating a large volume of conductive medium. The thermal mass of the volume of conductive medium is given approximately by equation (3.8), where Q is the average energy input in $J \cdot s^{-1}$, m is the mass of the water in kg, c_p is the specific heat of the conductive medium in $J \cdot kg^{-1} \cdot K^{-1}$, and ΔT is the anticipated change in temperature of the medium given energy input Q, in Kelvin [11]. The expected change in temperature of the water solution under 20 pps conditions at 230 J per pulse is approximately 0.010 °K (Q = 4.6 kW, m = 114 kg, c_p = 4186 $J \cdot kg^{-1} \cdot K^{-1}$).

$$Q = mc_p \Delta T \qquad (3.8)$$

3.4. High Pressure Pump Stand

An oil pump cart generated the high-pressure, flowing oil utilized during the tests. A schematic overview of the pump stand is presented in Figure 3-9. The pump delivers pressurized oil to the switch through two separate hydraulic lines. One of the hydraulic lines feeds the axial-flow inlet tube and the other feeds the coaxial-flow inlet tube. The unloading valve is utilized, in conjunction with the three needle valves, to control flow rate and pressure simultaneously. An adjustable over-pressure bypass valve prevents the inlet pressure from exceeding the set point pressure.

Two high-performance filters are utilized both before and after the switch to remove oil contaminants larger than 0.45 µm in diameter. The filters are designed to handle flow rates up to 20 gpm while maintaining low pressure loss across the filter medium. The filter medium itself is a finely-woven polymer mesh that removes as much as 99.99% of all particles 0.45 µm in diameter or larger [12]. The large surface area of the Pall Waterfine filter element is able to trap a large amount of free particles before needing replacement.

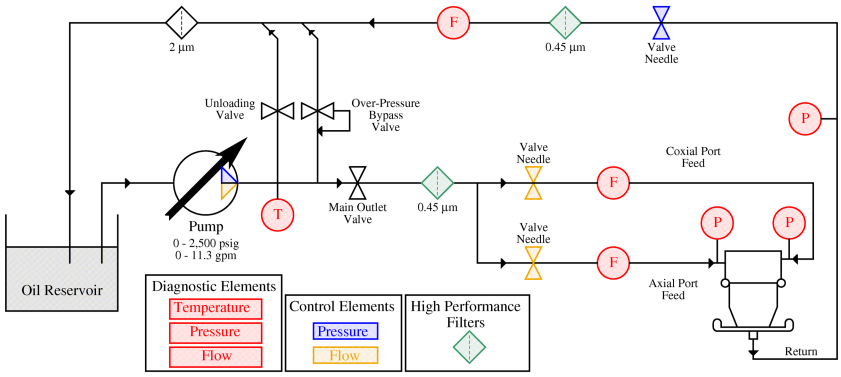

Figure 3-9. Schematic diagram of the high pressure oil circuit.

3.5. References

[1] R. G. Brown, R. A. Sharpe, and W. L. Hughes, "*Lines, waves, and antennas*," The Ronald Press Co., New York, 1961, pp. 12 – 42.

[2] M. Sadiku, "*Electromagnetics, 2nd Ed.*," Oxford University Press, New York, 1995, pp. 518 – 592.

[3] Data sheet*, Lexan 103 resin*, General Electric Co., Pittsfield, 1995

[4] H. C. Miller, "*Surface flashover of insulators*," IEEE Trans. Elec. Ins., vol. 24, no. 5, October 1989, pp. 765 – 786.

[5] J. M. Elizondo, T. H. Martin, K. W. Struve, and L. F. Bennett, "The Z-20 reliability calculations," *Proc. 13th Int'l. IEEE Pulsed Power Conf.*, June 2003, pp. 895–898.

[6] R.J. Adler, "*Pulse power formulary*," North Star Research Corp., Albuquerque, 2002.

[7] Data Sheet, *High power coaxial cable and assemblies*, Times Microwave Systems, Wallingford, 2002.

[8] *i.b.i.d.* M. Sadiku, pp. 530 – 536.

[9] *i.b.i.d.* M. Sadiku, pp. 184 – 189.

[10] Application Note, *Aqueous-electrolyte resistors*, R. E. Beverley III and Associates, Lewis Center, 2004.

[11] J. P. Holman, "*Thermodynamics*," McGraw-Hill Book Co., New York 1969, pp. 51 – 53.

[12] Data Sheet, *Water-fine series filter cartridges*, Pall Corp., East Hills, 2003.

Chapter 4. Diagnostics

System performance is monitored with a series of diagnostics. Diagnostics are deployed to observe both electrical and hydraulic conditions at key points throughout the test stand. In this chapter the diagnostic parameters are discussed and the equations are developed that relate the diagnostic response to the high-voltage or high-current signal. The electrical diagnostics included fast D-Dot probes, capacitive voltage monitors, and current transformers. Functional descriptions of the hydraulic diagnostics are provided.

4.1. Electrical Diagnostics

Electrical diagnostics were utilized to monitor modulator, pulse forming line, and output line status. The modulator performance is observed with a voltage probe and a current transformer. The pulse forming line status is monitored with a pair of fast D-dot probes. The output line status is measured with a fast capacitive divider.

4.1.1. Modulator Voltage Monitors

Modulator charge voltage is observed real-time to facilitate power supply voltage adjustment. The voltage is monitored with a dedicated high-voltage resistive divider that is securely affixed to the anode terminal of the capacitor bank. Figure 4-1 shows a photograph of the Fluke 80K-40 high-voltage resistive divider attached to the capacitor bank [1].

The primary voltage divider, housed within the red tube in the photograph of Figure 4-1, provides an output that is proportional to the input, but scaled down by a factor of 1,000. The probe output voltage is then read with a digital multimeter that has at 10 MΩ

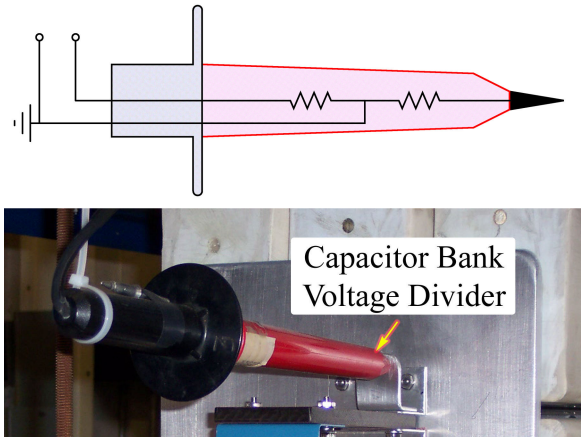

Figure 4-1. Photograph and schematic diagram of the voltage divider.

input impedance [2]. Figure 4-1 shows the equivalent circuit diagram of the probe-meter combination.

The resistive divider probe has not been optimized for high frequency operation, therefore it is only suitable for monitoring D.C. and low-frequency A.C. voltages [3]. A Tektronix P6015B high-frequency, high-voltage voltage divider was utilized to make measurements of the capacitor bank voltage under pulsed conditions. The Tektronix P6015B exhibits much higher performance because uncontrolled stray capacitances have been minimized by internally shielding the resistive divider from external components. The specifications for both the Fluke 80K-40 and the Tektronix P6015B are provided in Table 4-1.

Table 4-1. Specifications for the modulator voltage probes.

Manufacturer	Fluke Corp.	Tektronix
Part Number	80K-40	P6015B
Division Ratio	1000:1	1000:1
Bandwidth	60 Hz	75 MHz

4.1.2. Modulator Current Transformer

The modulator current developed during a pulse discharge is monitored with a current transformer. Current transformers couple to the circuit under measurement via a single-turn primary and utilized non-linear magnetic cores to increase the secondary winding inductance. The current transformer provides an output voltage that is proportional to the primary current. Specifications for the current transformer utilized in the circuit are provided in Table 4-2 [4].

Table 4-2. Specifications for the modulator current transformer.

Manufacturer	Stangenes Industries
Part Number	SI 3-0.002
Sensitivity	2 $mV \cdot A^{-1}$
Pulse Droop	< 0.005 $\% \cdot \mu s^{-1}$
Output Impedance	50 Ω

The Stangenes current transformer was selected based on a trade-off between voltage holdoff and the size. The inner diameter of the current transformer measures 7.62 cm which provides insufficient clearance around the high-voltage conductor to prevent breakdown. Larger diameter current transformers, however, would not have fit into the original modulator layout. Therefore a plastic sleeve was fabricated to increase the voltage holdoff between the transformer shield and the high-voltage conductor. The

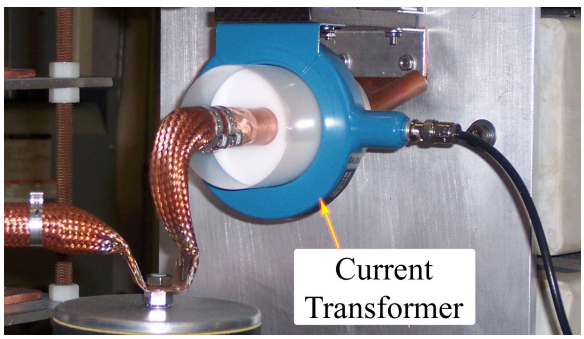

Figure 4-2. Photograph of the current transformer and capacitor bank low-frequency voltage monitor.

current transformer is shown installed around the high-voltage conductor in Figure 4-2.

An external attenuator 20 dB was utilized to reduce the relatively large output voltage generated during modulator operation [5]. Utilizing the voltage sensitivity listed in Table 4-2, the anticipated output voltage for a 10 kA current pulse is 20 V, which is utilized to drive a 50 Ω oscilloscope termination. A 20 dB attenuator reduced the measured voltage from 20 V_{peak} to 2 V_{peak}.

4.1.3. Switch Cathode and Anode D-Dot Probes

Switch voltage at the cathode and the anode was measured with fast D-dot probes. A D-dot probe is a simple diagnostic device that becomes electrically coupled to surfaces that are at some voltage with respect to ground and within the proximity of the probe [6]. The probe itself is composed of a floating conductor surrounded by a dielectric material. The probe response is governed by equation (4.1), which relates the output voltage, v_o in volts, to the dielectric constant of the bulk dielectric material, $\varepsilon_0\varepsilon_r$ in Farad·m^{-1}, the area of the probe exposed to the electric fields, A_p in m^2, the impedance that the probe drives, R in Ω, and the time-changing electric field, dE/dt in V·m^{-1}·s^{-1}. Figure 4-3 shows a

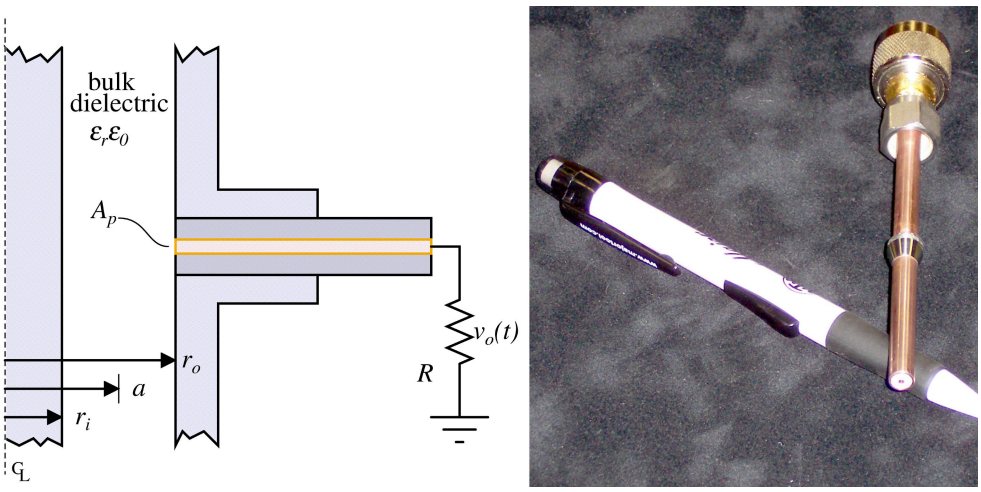

Figure 4-3. (*left*) Cutaway diagram of a D-dot probe in a coaxial geometry and (*right*) photographs of one of the D-dot probes prior to installation.

cutaway diagram of the D-dot probe that shows the parameters in equation (4.1).

$$v_o = \varepsilon_0 \varepsilon_r A_p R \, dE/dt \qquad (4.1)$$

The Poisson equation was solved for the cylindrical case in which the voltage is assumed uniform along the axis and about the axis (z and θ axes, respectively). Utilizing nomenclature presented in Figure 4-3 for the system dimensions, equation (4.2) is the resulting differential electric field strength with respect to time, where *dv/dt* is the time-derivative of the high-voltage signal in $V \cdot s^{-1}$, r_o is the outer radius of the coaxial structure in meters, r_i is the inner radius of the coaxial structure in meters, and $a = r_o$.

$$dE/dt = \frac{1}{a \, \mathbf{ln}\left(r_o / r_i\right)} dv/dt \qquad (4.2)$$

The dimensions and estimated scaling factor for the of the D-dot probes that were fabricated are presented in Table 4-3. The probes were constructed from 13 cm lengths of 0.25 inch semi-rigid coaxial cable and N-connectors were soldered to the free end. The probe end was inserted into ¼" pipe-thread mounts built into the ground-return spool that surround the switch. Swagelok fittings were utilized to secure the probe body to the pipe-threaded ports.

Table 4-3. Dimensions and scaling factor for the D-dot probes.

	Cathode	Anode
r_i (cm)	11.46	17.07
r_o (cm)	17.86	21.67
ε_r	2.1	2.1
A_p (10^{-3} cm^2)	21.1	21.1
R (Ω)	50	50
dv/dt (10^{12} $V \cdot s^{-1}$)	0.1	8
Sensitvity, ($mV \cdot kV^{-1}$)	0.011	2.66

The D-dot probe response is proportional to the time-rate of change of the source signal, as indicated in equation (4.1). The signal is passively integrated at the oscilloscope utilizing a fast capacitive integrator. The integrator specifications are summarized in Table 4-4 [7]. The integrator includes a terminating resistance on the input to prevent transmission line reflections from degrading signal performance. The integrated cathode waveform signal experienced droop due to the exponential time constant of the integrator being comparable to the pulse duration. The droop on the cathode waveform was numerically removed on the data reported. The anode waveform did not experience significant droop.

Table 4-4. Fast capacitive integrator specifications.

Manufacturer	Titan Pulse Science Div.
Part Number	Passive Integrator
RC Time Constant	2 μs
Input Impedance	50 Ω
Risetime	< 5 ns

4.1.4. Output Voltage Cable Monitor

An output cable monitor was installed on one of the high-voltage output transmission lines as a backup to the anode-mounted D-dot probe. The capacitive cable monitor utilizes the same general technique as the D-dot probe to generate a signal, however the ratio of the capacitances, combined with the output impedance allows the capacitive monitor to generate a signal on the output that is proportional to the driving signal. The specifications for the capacitive monitors selected are given in Table 4-5 [8]. Photographs of the cable monitor before and after installation on the high-voltage transmission line are shown in Figure 4-4.

Table 4-5. Specification summary for the capacitive cable monitor.

Manufacturer	Titan Pulse Science Div.
Part Number	PSI-CCM-RG-218
RC Time Constant	5.05 μs
Droop, 70 ns	< 1.4 %
Output Sensitivity	53 $\mu V \cdot V^{-1}$

Figure 4-4. Photograph of the capacitive cable monitor prior to and following installation.

4.1.5. Probe Calibrations

The capacitive cable monitor was calibrated against an external high-impedance voltage probe with a square-pulse, fast rise time pulse generator. The pulse generator utilized for calibrations was a Tektronix type 109 mercury-relay cable pulser. A length of 50 Ω coaxial cable was D.C. charged to a voltage and discharged into the high-voltage transmission line that the cable monitor was attached to. The voltage pulse was simultaneously measured at the cable monitor output and with a calibrated P6015B voltage monitor at the input of the high-voltage transmission line. The response from

both probes was compared for a number of test shots and an average value for the cable multiplier was thus estimated to be 5600. The actual scale factor is about 1/3 the estimated value of 53 $\mu V \cdot V^{-1}$ (1/5600 ~ 173 $\mu V \cdot V^{-1}$), and may be due to incorrect measurements on one of the cable monitor capacitances.

The D-dot probes were calibrated *in situ* once the cable monitor had been successfully calibrated at low amplitude. The scale factors were determined by simultaneously measuring the integrated output from each of the D-dot probes and comparing the correctly scaled cable monitor output. The scale factor for the cathode D-dot was estimated *after* numeric corrections for droop had been applied. The scaling multipliers

Table 4-6. Measured probe sensitivities.

	Multiplier	Termination	Droop
Cathode D-Dot	7.6292×10^6	2 μs integrator	< 72% at 2.5 μs
Anode D-Dot	15.264×10^6	2 μs integrator	< 2.8% at 70 ns
Cable Monitor	5600	20 dB attenuator	< 1.4% at 70 ns

for each of the probes is presented in Table 4-6.

Representative waveforms from each of the diagnostics presented in Table 4-6 were generated to demonstrate the output response of each. Figure 4-6 shows the response of the capacitive cable monitor to a low-amplitude voltage pulse that was simultaneously monitored with a high-frequency passive probe (Tektronix P5100, 100x). The cable monitor waveform is scaled up by a factor of 5600 and agrees well with the P5100 voltage monitor.

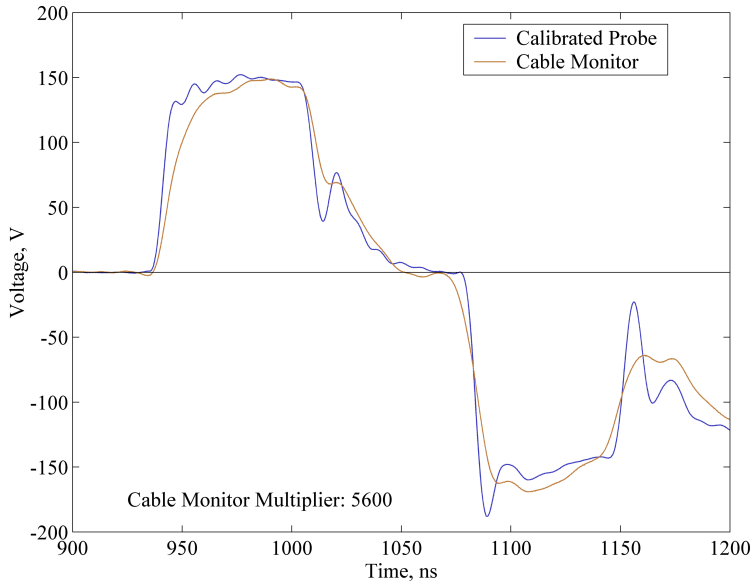

Figure 4-6. Simultaneous plot of cable monitor and external passive voltage probe.

The scaled response of the cathode-mounted D-dot probe is plotted with the cable monitor response in Figure 4-7. A series of five shots was recorded and the average value of the scale factor determined for each of the five shots was computed and reported in Table 4-6. The waveform plotted in Figure 4-7 shows a scaled cathode voltage waveform following integrator-droop adjustment.

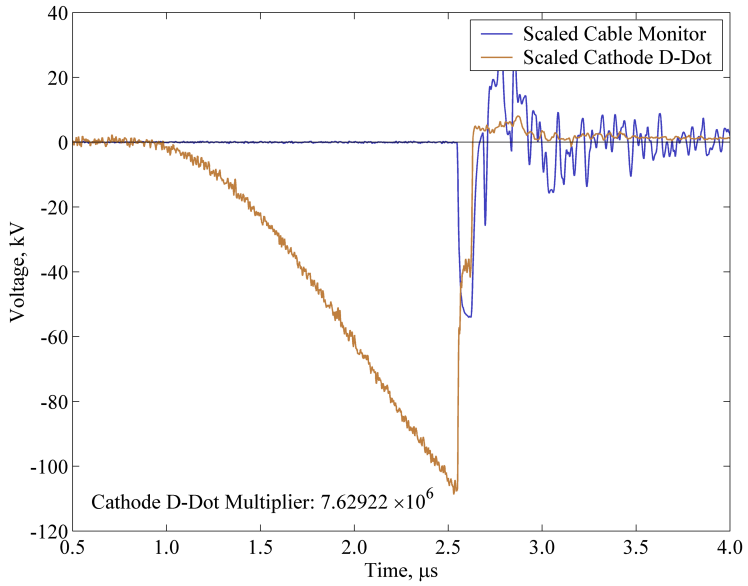

Figure 4-7. Simultaneous plot of the PFL voltage and the cable monitor response.

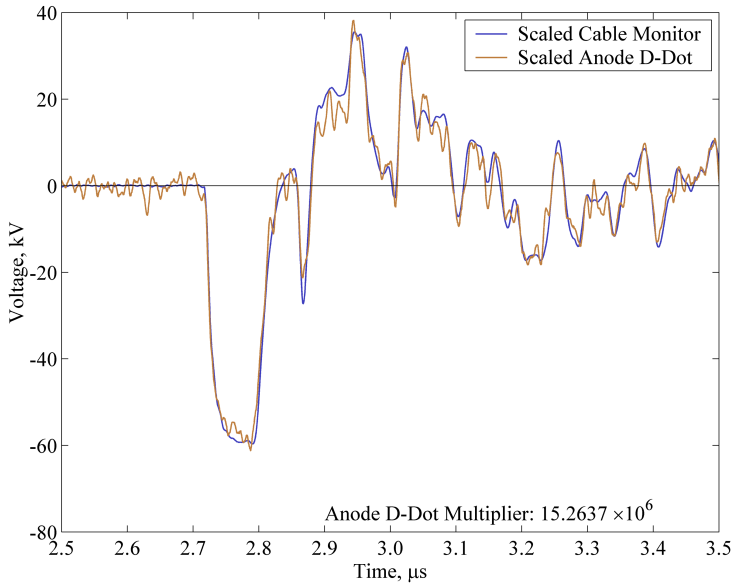

Figure 4-8. Simultaneous plot of the anode voltage and the cable monitor response.

The scaled response of the anode-mounted D-dot probe is plotted with the cable monitor response in Figure 4-8. The measured D-dot response was compared directly to the measured cable monitor response to generate a scaling factor for the D-dot probe. The scaling factor was applied to the measured response to generate the scaled response seen in Figure 4-8. The overall noise floor was observed to temporarily increase following a discharge, which explains the increased noise content superimposed on the D-dot trace in Figure 4-8.

4.2. Fluid Diagnostics

Fluid diagnostics were deployed to measure the properties of the oil in the hydraulic circuit. Switch inlet and outlet pressure were recorded, as was the relative flow rate going into the axial and coaxial sections of the switch. Total flow rate was measured in the return line of the hydraulic circuit. Oil temperature was monitored at the output of the hydraulic boost pump.

4.2.1. Oil Pressure

The oil pressure was monitored with a Bourdon tube pressure gage at the inlet of the axial flow section of the switch and at the outlet of the switch. A mechanical diagram of a simplified Bourdon tube is presented in Figure 4-9. High-pressure oil tends to force the tube to straighten slightly, pulling the spur gear and resulting in indicator rotation. The tube diameter and material determines the range over which the gage is linear, and most gages remain linear to better than 0.1% over their full indicated range [9]. Specifications for the two identical gages utilized to measure oil pressure at the switch are provided in

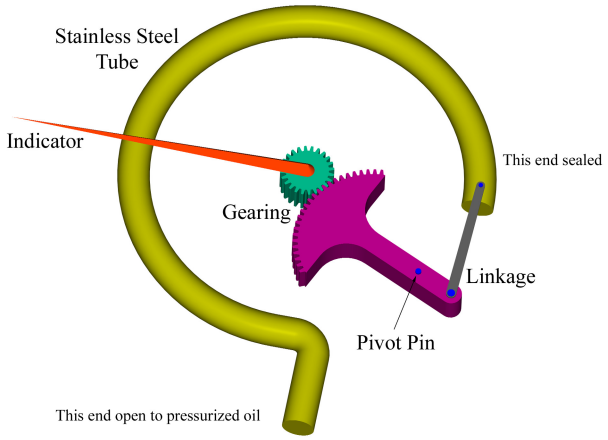

Figure 4-9. Mechanical drawing of a simplified Bourdon-tube pressure gage.

Table 4-7 [10].

Table 4-7. Summary of the pressure gage specifications.

Manufacturer	ENFM Co.
Part Number	7211-4-1/2-3000
Pressure Range	0 - 3000 psig
Accuracy	0.1% of F.S.
Indicated Resolution	20 psig
Gage Diameter	4.5 inches

4.2.2. Oil Flow

The oil flow rate was monitored with two variable orifice sensors and a turbine sensor. The variable area (variable orifice) sensors were installed on the high pressure inlet lines to measure the relative flow rate entering the axial and coaxial sections of the switch. The turbine flow sensor was installed on the return line to measure the total oil flow rate.

4.2.2.1) Variable Area Orifice Flow Sensor

The variable area orifice flow sensor utilizes the momentum of the incoming oil stream to move a calibrated orifice. A mechanical drawing of the variable area orifice flow sensor concept is provided in Figure 4-10 [11]. The spring is compressed by the orifice, which is driven to the right by the momentum of the oil. As the orifice moves further to the right the amount of momentum transfer is designed to remain constant with increasing flow rate. The indicator is magnetically coupled to the orifice.

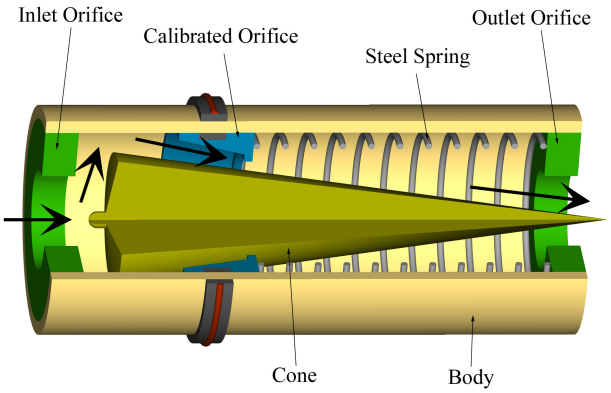

Figure 4-10. Simplified mechanical diagram of a variable area orifice sensor.

The variable area orifice sensors are utilized to measure the relative flow rates in the two high-pressure hydraulic lines. The orifice sensors were calibrated against the

Table 4-8. Specifications for the variable area orifice flow sensors.

Manufacturer	Hedland Flow Meters
Part Number	H601-A-010-RF
Flow Rate Range	1 - 15 gpm
Indicated Resolution	0.5 gpm
Maximum Pressure	3,500 psig

calibrated turbine sensor that will be described shortly. Both orifice sensors indicated identical flow rates under identical conditions, and both sensors indicate slightly exaggerated flow rates due to the specific gravity of the oil. The specifications of the variable area orifice flow sensors utilized are given in Table 4-8 [12].

4.2.2.2) Turbine Flow Sensor

A calibrated turbine flow sensor was utilized in the oil return line to provide a total flow measurement. The turbine sensor is capable of much greater resolution and much higher precision than the variable area orifice flow sensors. The turbine sensor is composed of a small turbine that is suspended on an axle in the flowing oil stream. As oil moves over the turbine blades the turbine spins on the axle. The turbine is fabricated from

Table 4-9. Specifications for the oil return line turbine flow sensor.

Manufacturer	Cox Instruments
Part Number	AN-10
Flow Rate Range	2 - 20 gpm
Resolution	∞ within range
Maximum Pressure	3,500 psig

a high permeability metal so that its rotation disrupts a magnetic field set up by an external circuit. The disrupted magnetic field is detected as a variable-frequency oscillation that is subsequently converted to an equivalent flow rate by a flow computer [11]. Specifications for the flow sensor used in the return line are given in Table 4-9 [13].

The turbine sensor also requires a flow computer to convert the variable frequency output from the sensor into an equivalent flow rate. The specifications for the flow computer utilized are presented in Table 4-10 [14]. The turbine sensor and the flow computer were calibrated simultaneously with the dielectric oil used for testing.

Table 4-10. Specifications for the flow computer used with the turbine sensor.

Manufacturer	Hoffer Flow Controls
Part Number	163
Resoluion	0.01 gpm indicated

4.2.3. Oil Temperature

The oil temperature was monitored during system operation to maintain consistency from test to test. The pump cart had a built in thermometer that registered the temperature at the outlet of the high-pressure boost pump. The thermometer utilized a bulb, filled with a liquid with a linear coefficient of thermal expansion, to drive the actuator for the meter indicator. The specifications for the thermometer are provided in Table 4-11 [15].

Table 4-11. Specifications for the oil thermometer.

Manufacturer	H. O. Trerice Co.
Part Number	L80040110
Temperature Range	30 - 240 ^{o}F
Resolution	±1 scale division
Scale Divisions	2 ^{o}F

4.3. References

[1] Data Sheet, *Fluke 80K-40 high voltage probe instruction sheet*, Fluke Corp., Everett, 1997.

[2] Data Sheet, *Fluke 77/75/23/21 series III multimeter instruction sheet*, Fluke Corp., Everett, 1997.

[3] Data Sheet, *Passive high voltage probes*, Tektronix Inc., Beaverton, 2005.

[4] Data Sheet, *CT3-0.002 pulse current transformer*, Stangenes Industries Inc., Palo Alto, 2001.

[5] Data Sheet, *Fixed attenuators*, JFW Industries Inc., Indianapolis, 2001.

[6] W. R. Edgel, "*Electric and magnetic field sensor application*," App. Note AN-192, Prodyn Technologies Inc., Albuquerque, 2002.

[7] Data Sheet, *Fast capacitive integrator*, Titan PSD, San Leandro, 2003.

[8] Data Sheet, *Capacitive cable monitor*, Titan PSD, San Leandro, 2002.

[9] H. P. Kallen, "*Handbook of instrumentation and controls, 1st Ed.*," McGraw-Hill Book Co., New York, 1963, pp. 3 – 1 to 3 – 32.

[10] Data Sheet, *Series 7211 liquid filled pressure gages*, ENFM USA, Jacksonville, 2004.

[11] *i.b.i.d.*, H. P. Kallen, pp. 5 – 1 to 5 – 59.

[12] Data Sheet, *3500/6000 psi flow meters for petroleum fluids*, Hedland Inc., Racine, 2004.

[13] Technical services, personal communications, Cox Instruments Inc., August 2004.

[14] Data sheet, *Model 163 digital flow rate indicator*, Hoffer Flow Controls Inc., Elizabeth City, 1995.

[15] Data sheet, *Remote reading dial thermometers*, H. O. Trerice Inc., Oak Park, 2001.

Chapter 5. Switch Design and Switch Tests

Two high-voltage, high-pressure oil switches were developed to be installed on the output of the pulse forming line to test breakdown effects at repetition rates up to 20 pps and at pressures up to 13.79 MPa (2000 psig) in poly-α olefin (PAO) oil. The first switch described was developed over a very short period to generate some initial data on the breakdown performance of PAO at pressures ranging up to 10.34 MPa (1500 psig). The DVT switch described was developed for full-scale testing of the pressurized poly-α olefin dielectric oil to 13.79 MPa and rep-rates to 20 pps. The second switch is referred to as the design verification test (DVT) switch.

5.1. Dielectric Test Switch

The dielectric test switch was utilized to generate initial insight into the rep-rate breakdown performance of poly-a olefin oil under flowing, pressurized conditions. The switch was developed with replaceable electrodes so that a number of geometries could be evaluated with a number of different electrode materials. The anode electrode was made adjustable by employing a threaded electrode stalk, thereby allowing greater control over the breakdown voltage. A cross sectional drawing of the dielectric test switch is shown in Figure 5-1.

5.1.1. Dielectric Test Switch Design

The dielectric test switch was designed to mimic the geometry of a pre-existing gas switch that was known to fit the test platform. A mechanical analysis of the geometry presented was performed by hand to verify that operating stresses remained substantially lower than material stress limits. High performance polymers with greater material stress

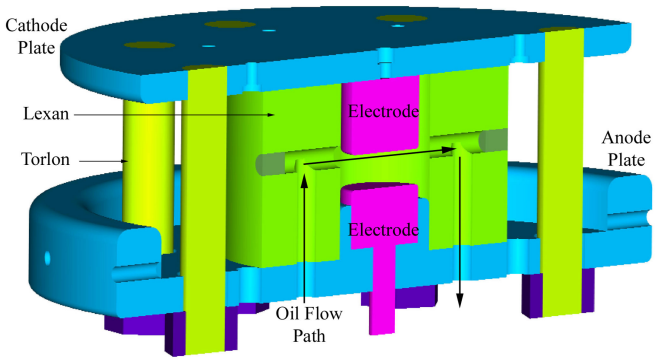

Figure 5-1. Cross sectional view of the dielectric test switch.

limits were employed throughout the design to enable greater maximum oil pressures. The envelope was fabricated from General Electric Lexan polycarbonate (PC 103) [1]. The clamp bolts were fabricated from Solvay Advanced Polymers 30% glass-fiber reinforced Torlon poly-amide imide (PAI 4203) [2]. The upper and lower plates (cathode and anode, respectively, in Figure 5-1) were fabricated from aluminum. Three sets of electrodes were fabricated, one set from type 304 stainless steel, another set from 17-4 precipitation-hardening stainless steel, and the final set from CW68 copper-tungsten alloy.

The mechanical analysis of the envelope was performed to define a maximum safe operating pressure. The principal stress the envelope will be subject to is known as hoop tension. Hoop tension is demonstrated in Figure 5-2. An applied force on the inner surface of the envelope is generated by oil pressure. The curved shape of the envelope wall translates a radial outward force into its x and y components. The hoop tension acts in directions that oppose the oil pressure-generated force. Hoop tension is generated at the molecular level by the bonds between the polymer chains in the envelope material. When the bond-strength of the molecules is exceeded the envelope breaks along the weakest links, resulting in a complete rupture.

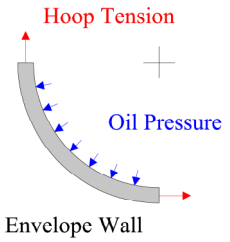

Figure 5-2. View from the top of an internally stressed cylinder.

The hoop tension developed in the envelope is proportional to the applied oil pressure acting on the inner surface of the envelope. Equation (5.1) provides the hoop stress relationship, where σ_t is the circumferential tension developed in psi, p is the internal oil pressure in psi, r_i is the inner diameter of the envelope in inches, and t is the thickness of the envelope wall in inches [3]. The envelope was designed for operation up to 1,500 psig oil pressure, with a wall thickness of 1.75 inches and an inner radius of 1.00 inch. Substituting these values into (5.1) results in a hoop tension of 2,625 psi. The maximum tensile stress for Lexan 103 is 8.4 kpsi which results in a safety factor of 3.2 for the envelope design when the internal oil pressure is 1,500 psig.

$$\sigma_t = \frac{pr_i}{t} \qquad (5.1)$$

A mechanical analysis was performed on the clamp bolts to ensure they could withstand the tension generated when the switch was pressurized. The force that is transferred to the bolts is generated as the oil pressure, p in psi, pushes against the exposed area, A_p in in^2, on the anode and cathode plates. The force developed results in a stress within each of the bolts which is given by equation (5.2). The bolt stress, σ_l in psi, is related to the force transferred to the bolt, divided by the number of bolts, n, and the effective area of the threaded section, A_t in in^2 [3]. Utilizing an oil pressure of 1,500 psig, an exposed area of 3.142 in^2, a total of 8 bolts, and an effective area per bolt of 0.60 in^2,

the total axial stress developed in each bolt is approximately 980 psi. The tensile strength of the bolt material, Torlon PAI 4203, is 20 kpsi, which gives a safety factor of more than 20 when the internal oil pressure is limited to 1,500 psig.

$$\sigma_a = \frac{pA_p}{nA_t} \qquad (5.2)$$

The final switch design utilized for the first rep-rate tests is shown prior to installation in Figure 5-3. The major components of the switch are easily visible in Figure 5-3, including the anode and cathode plates, the clamping bolts, and the plastic envelope. Figure 5-4 shows all of the switch components prior to assembly in which additional details can be seen, including the anode electrode seat on the anode plate.

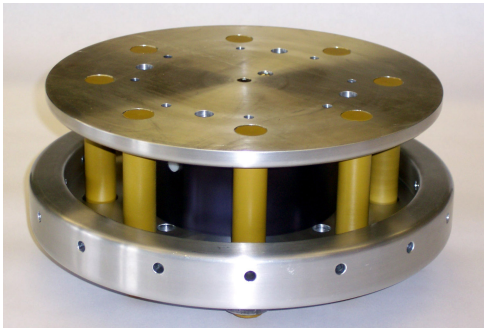

Figure 5-3. Dielectric test switch assembled and ready to install onto the PFL.

Figure 5-4. Dielectric test switch prior to assembly.

5.1.2. Dielectric Test Switch Results

The dielectric test switch was utilized to demonstrate switch performance and recovery at the 230 J per pulse energy level and to rep-rates up to and beyond 20 pps. The

switch was tested at a number of flow rates to determine if there was the potential for performance enhancement 'tuning' through adjustment of the hydrodynamic parameters. The switch also provided some early results on the severity of electrode erosion under rep-rate conditions for the three electrode materials studied. The data reported was collected on a capacitive probe that was originally installed on the PFL—the probe was never calibrated and failed before calibrations could be performed. The time to breakdown is therefore reported only for the rep-rate switch data.

Testing was performed with the electrodes set to a gap spacing of about 1.50 mm. The electrode gap spacing resulted in an estimated maximum field strength of 1.8 $MV \cdot cm^{-1}$ at a charge voltage magnitude of 250 kV and atmospheric pressure oil. Under actual operation the gap spacing increased because the Torlon clamping bolts underwent tension-related stretching. The magnitude of the electrode deflection was measured and is presented in Figure 5-5. The deflection was accounted for in estimates of the electric field

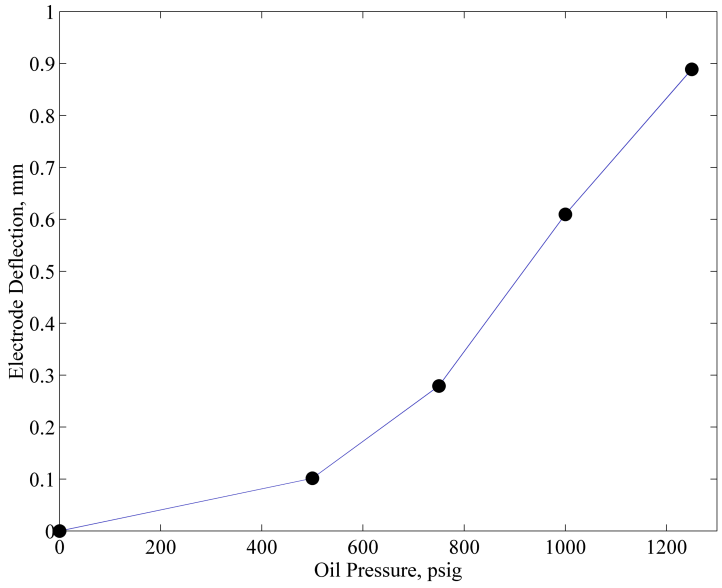

Figure 5-5. Dielectric test switch electrode deflection as a function of pressure.

strength.

The first series of tests performed on the rep-rate switch utilized a set of flat electrodes fabricated from type 304 stainless steel. The oil pressure was maintained at 1,000 psig and the oil flow rate was maintained at 7 gpm. Test shots were taken in bursts of four shots at 20 pps. A total of 18 sets of data were collected on a Tektronix TDS3054 oscilloscope. Seven of the 18 sets of four-shot bursts resulted in no late breakdowns, while two of the sets resulted in complete misfires for all four shots. The remaining bursts each had at least one late breakdown, although in several cases two late breakdowns were observed. Table 5-1 presents the descriptive statistics computed for the misfire-free data sets. The time to breakdown was estimated from photographic data and therefore the precision of the data is somewhat limited; the maximum time to breakdown reported is slightly exaggerated as a result of the precision error. The standard deviation reported is approximately ±13% of the mean time to breakdown reported.

The remainder of the experiments focused on testing electrode materials. The data reported in Table 5-1 was collected utilizing type 304 stainless steel electrodes. A second set of electrodes was fabricated from 17-4 precipitation-hardening stainless steel to see the impact of greater mechanical rigidity upon electrode erosion. Both sets of electrodes were operated for a limited number of shots which allowed the formation of shot group

Table 5-1. Statistical analysis of rep-rate switch time to breakdown data. †See text.

Shots Analyzed	27
Mean, μ	1.89 μs
Standard Deviation, 1σ	248 ns
Maximum	2.6 μs†
Minimum	1.4 μs
Range	1.2 μs

concentrations to be identified and examined.

A photograph of the type 304 electrodes is presented in Figure 5-6. The electrodes indicate preferential breakdown on one half of the surface which suggests the electrodes were not perpendicular to each other. The shots form into small clusters which suggests that the local field enhancement plays a major role in determining subsequent breakdowns. The electrodes were operated for several hundred shots before being

Figure 5-6. Photograph of the type 304 stainless steel electrodes following several hundred shots.

removed and photographed.

A photograph of the 17-4 precipitation hardened stainless steel electrodes is presented in Figure 5-7. The electrodes were fabricated with flat faces. The electrodes experienced roughly twice the number of shots as the type 304 electrodes. The erosion is distributed over more the electrode surface which is due to a more careful approach to fabrication that left the electrode surfaces more parallel than the previous set. Again the erosion has formed into small clusters over much of the surface. The erosion on both the type 304 and the 17-4 P.H. stainless steel is nearly equivalent.

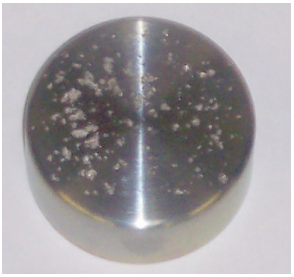

Figure 5-7. Photograph of the 17-4 precipitation hardened stainless steel electrodes following several hundred shots.

A final set of electrodes tested on the rep-rate switch were hemispherical Elkonite electrodes, shown in a photograph in Figure 5-8. Elkonite is composed of 50% tungsten and 50% copper. The two metals are milled into fine powders, homogeneously mixed, and then pressed at very high pressure and high temperature to obtain an alloy that has both high conductivity and high thermal resistance (*e.g.* resists melting). The photograph was taken after 680 shots had been taken. The shots are concentrated at the apex of the radii. The overall erosion does not appear to be very severe so Elkonite was retained as a candidate electrode material for the full-scale test switch.

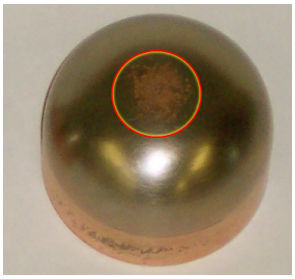

Figure 5-8. Photograph of the CW68 Elkonite electrodes following about 680 shots. The locus of shots is encircled.

The flat electrode geometry, although invaluable for determining the breakdown field strength of PAO and identifying candidate electrode materials, was found to have unacceptably high misfire rate. The small size of the electrodes utilized for testing also limit the operational lifetime of the electrodes under repetitive conditions. The dielectric test switch was not developed as an optimized solution for repetitive breakdown testing

and additional work described in the next section produced a much more robust rep-rate capable switch by taking advantage of the self-clearing flow profile of an axial geometry.

5.2. Rep-Rate DVT Switch

A rep-rate switch was developed with an geometry that promoted an axial flow profile to sweep out switching byproducts as well as to distribute wear over a larger surface area, and therefore extend the operating lifetime of a set of electrodes. This switch is referred to as the design verification test (or DVT) switch. The DVT switch was utilized to perform a parametric analysis of oil pressure, oil flow rate, oil temperature, and charge voltage on the breakdown performance of poly-α olefin oil. The DVT switch was redesigned to incorporate design upgrades to correct several mechanical, electrical, and fluid dynamic problems discovered during initial testing. Experiments are reported on that address breakdown performance with respect to the oil conditions and the charge voltage.

5.2.1. DVT Switch Design Modifications

A number of modifications were made to the switch to correct mechanical flaws as well as to attempt to correct problems with jitter that were discovered in early switch test trials. Mechanical flaws were discovered that affected both the integrity of the switch and the functionality of the switch. Problems with the dynamics of the oil flow within the switch were discovered that were believed to play a major role in the voltage breakdown jitter. A cutaway diagram of the switch is provided in Figure 5-9 and includes nomenclature that will be utilized to describe the switch components.

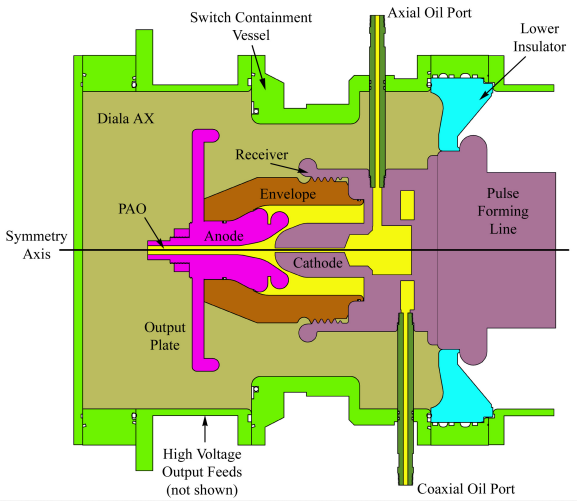

Figure 5-9. Cutaway diagram of the output end of the PFL showing the switch cross section and nomenclature.

The mechanical flaws that were discovered were concentrated in the switch receiver section, which is composed of two major components including the bell-shaped housing and a collar piece utilized to connect the switch to the PFL. A mechanical diagram of the receiver is shown in Figure 5-10 in which the flawed parts have been highlighted. Five problems were discovered and are indicated with the letters 'A' through 'E' in Figure 5-10.

The original design called for the receiver to thread into the collar with a series of threads, labeled 'A' in Figure 5-10. The specifications did not take into account the

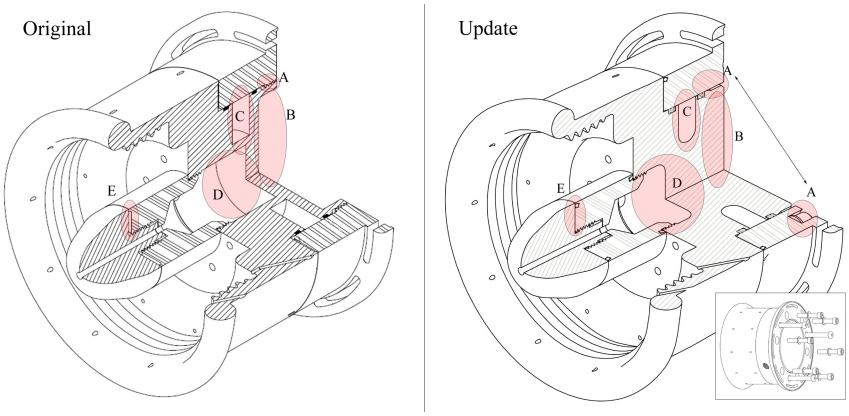

Figure 5-10. Perspective drawing of the switch receiver indicating the mechanical (*left*) problems discovered and (*right*) the problem solutions.

relative positioning of the start of the threads with respect to the oil inlet ports (both axial and coaxial). The oil feed ports are supposed to align along a straight line and pointing in opposite directions; any misalignment will result in the switch not fitting into the containment spool. The threaded section was machined flat to rectify the problem, and a series of threaded cap screws were implemented to hold the receiver assembly together. The cap screws are just visible in the updated switch drawing in Figure 5-10 and the locations of the six cap screws are indicated in the inset.

Modifications at points labeled 'B', 'C' and 'D' were made to improve the mechanical strength of the receiver. The mass of metal that was removed at the point labeled 'B' in the original implementation was not removed in the modified version. At points 'C' and 'D' in the original version the sharp edges were converted to rounded edges for the modified version. The rounded edges reduce the effective stress, thereby increasing the mechanical strength.

The contact point between the removable electrode and the electrode shaft, labeled 'E' on the original version of the switch shown in Figure 5-10, originally had no provisions for a current contact gasket. The lack of the contact gasket resulted in small discharges that produced a significant amount of carbon upstream of the electrically stressed region. In the updated version of the receiver, all threaded components that carried current were fabricated with current contact gaskets. Current contact gaskets were also added to the base of the cathode electrode shaft (visible in Figure 5-10) as well as on the anode electrode at similar locations.

Based upon electrical breakdown tests, the switch was modeled in a computational fluid dynamics program to simulate steady-state oil flow streams under typical operating

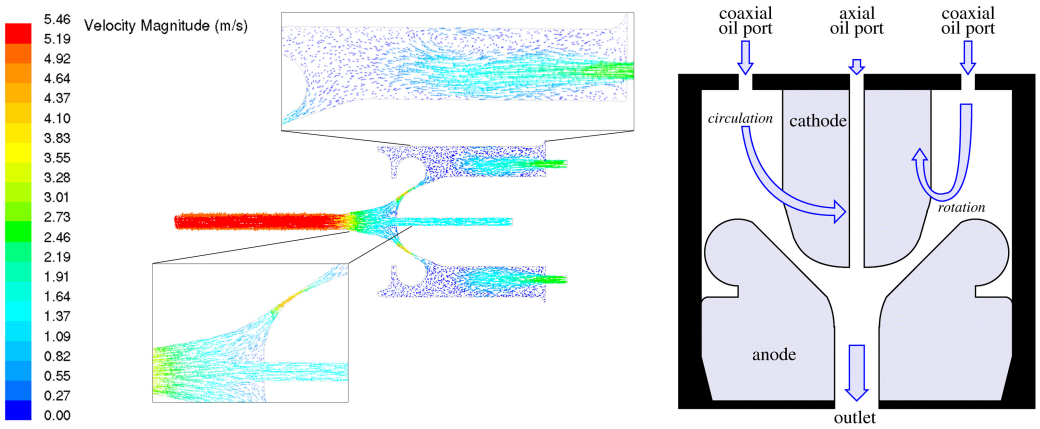

Figure 5-11. (*left*) Results of a computer model to predict oil flow within the DVT switch and (*right*) an interpretation of the simulation results.

conditions. The results of the simulation on the original DVT switch design, shown in Figure 5-11, indicated the oil flow within the switch underwent significant circulation. The circulation would have led to the entrapment of discharge byproducts upstream of the electrically stressed region within the electrodes, which is believed to have resulted in the poor breakdown performance that was observed during the initial tests.

A flow-shaping device was designed and simulated to control the oil-flow dynamics. The simulations, shown in Figure 5-12, predicted that the oil stream lines could be straightened and the upstream coaxial oil flow could be increased. The reduction in

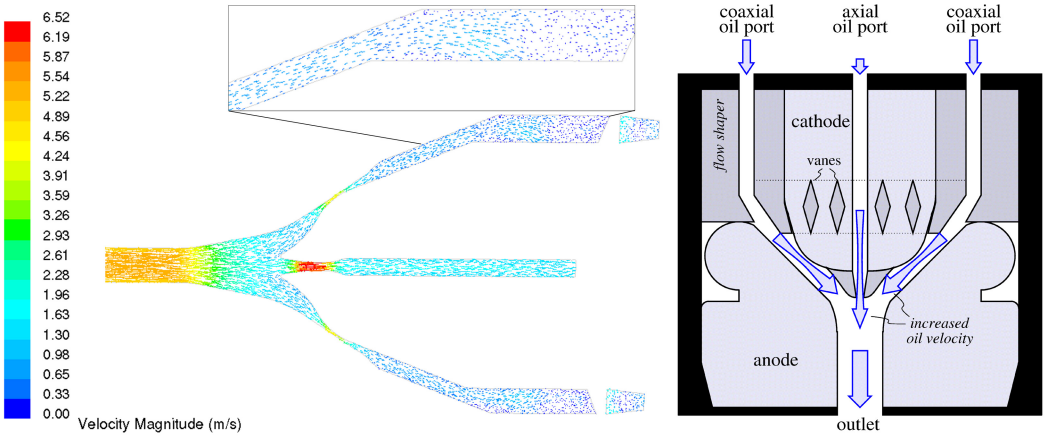

Figure 5-12. (*left*) Results of a computer model to predict the flow in the DVT switch with the addition of the flow shaper and (*right*) the results interpreted.

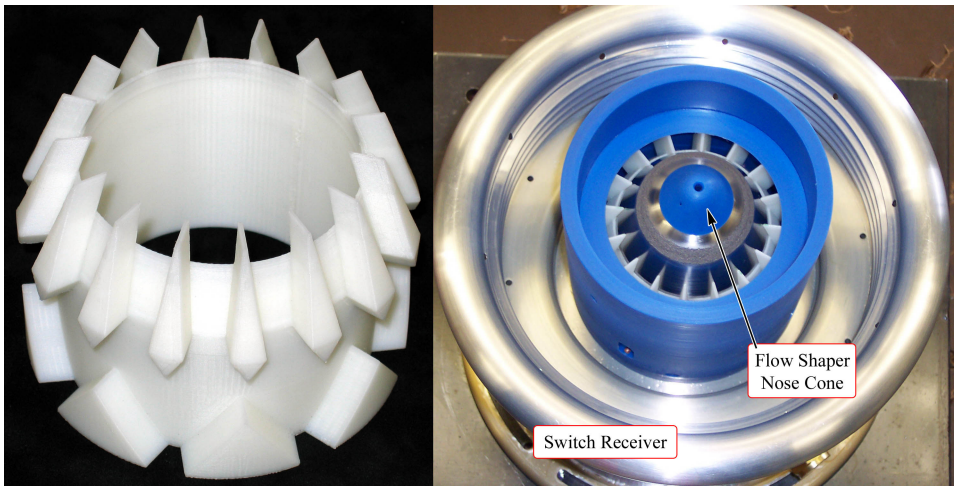

Figure 5-1. The flow shaper prior to, and following installation.

circulation reduced the likelihood of upstream particle entrapment and the increased velocity significantly reduced the amount of solid phase particles that could get upstream following a discharge. The flow shaper that was finally implemented in the switch is shown in Figure 5-13.

During tests being performed at high pressure the switch envelope suddenly ruptured. An analysis of the situation revealed a small oversight in the design process that led to the envelope failure. The envelope, which was fabricated from 40% glass-fiber reinforced polyether-ether ketone (PEEK), has a material stress-time profile that does not remain constant [4]. As suggested in Figure 5-14 for a given tensile stress the envelope has a limited lifetime that increases exponentially as the magnitude of tensile stress is decreased. A mechanical simulation, shown in Figure 5-15, indicated a peak combined stress on the order of 12 kpsi for an internal oil pressure of 2,500 psig (17.24 MPa). Examination of the curve for Victrex 450GL30 in Figure 5-14 suggests a lifetime of around 200 operating hours, which is very close to the time at which failure occurred.

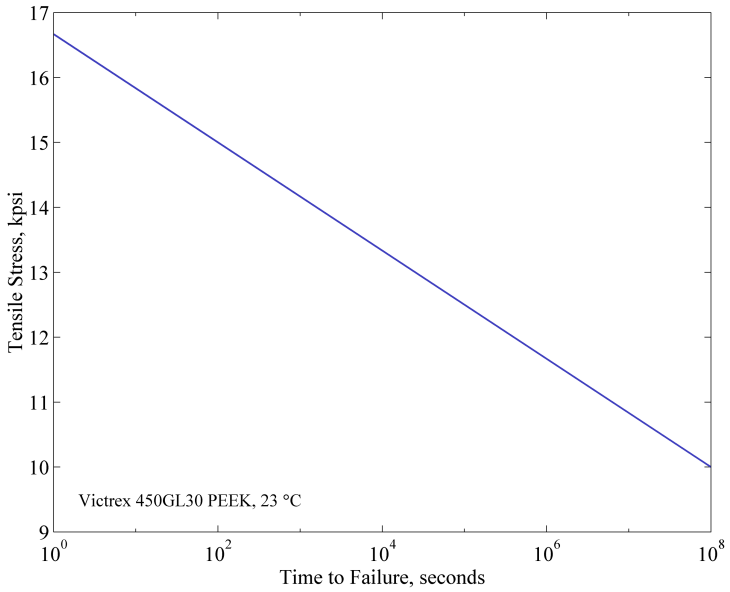

Figure 5-14. Stress versus time to failure for 30% glass filled PEEK at 23 °C.

Following the mechanical analysis the maximum operating oil pressure was reduced to 1,500 psig (10.34 MPa), resulting in a projected 27,000 hour mechanical lifetime for the envelope. The maximum operating pressure of 10.34 MPa is significantly above the critical pressure of poly-α olefin oil and does not appear to have significantly impacted the DVT switch operation.

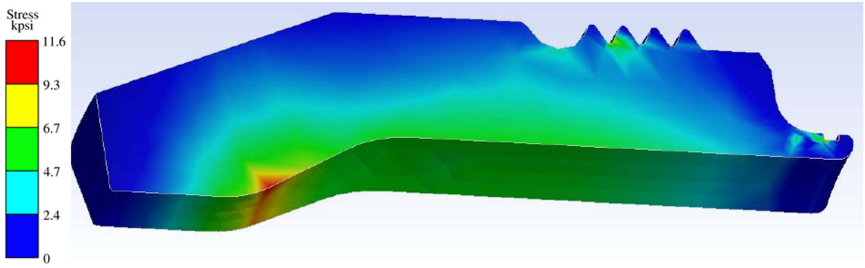

Figure 5-15. The von-Mises stress developed in the envelope with 2,500 psig internal oil pressure.

5.2.2. DVT Envelope Characterization

The plastic envelope is expected to elongate slightly when the oil within the switch is pressurized. The elongation of the housing will cause the gap spacing to increase. The housing elongation was measured with a dial gage for two different envelopes. Both

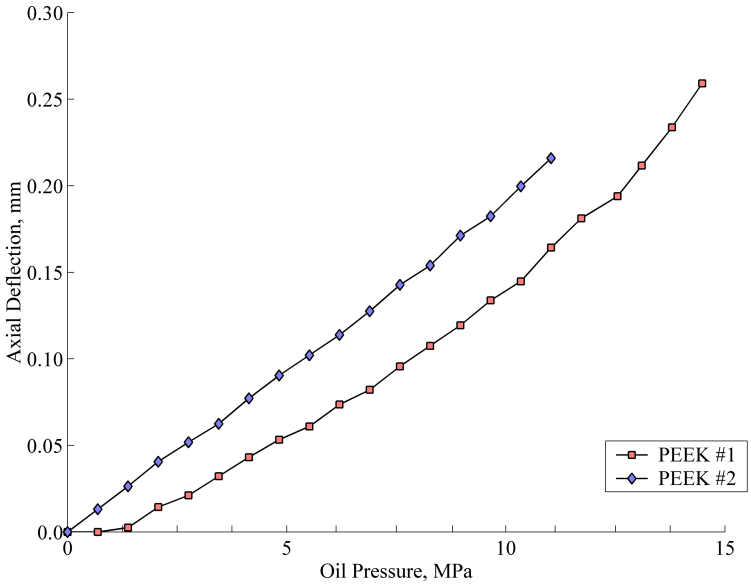

Figure 5-16. Axial elongation as a function of pressure for the 40% glass-fiber reinforce PEEK envelopes.

envelopes were fabricated from 40% glass-fiber reinforced PEEK. The switches were pressurized in 689 kPa (100 psig) steps over the range of pressures operation was expected to take place. The measurements were performed three times for the first PEEK envelope (PEEK #1) and six times for the second envelope. The average elongation at each pressure is plotted in Figure 5-16.

The axial elongation of the envelope does not result in a one-to-one increase in gap spacing due to the geometry of the gap. Figure 5-17 illustrates the relationship between the axial elongation and the elongation perpendicular to the gap. The gap spacing is

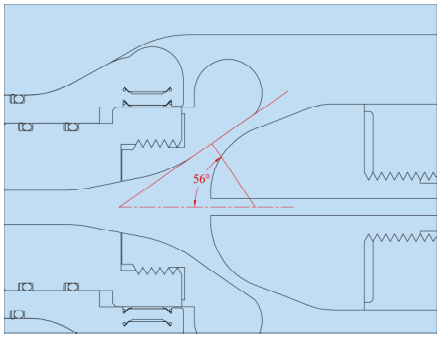

Figure 5-17. The relationship between axial displacement and perpendicular gap

related to the cosine of 56° times the overall axial displacement, which includes the gap adjustment displacement plus the pressure-dependent displacement plotted in Figure 5-16. The gap spacing is therefore equal to the total axial displacement times 0.55919.

5.2.3. Rep-Rate DVT Switch Results

Experiments were performed to demonstrate the rep-rate DVT switch operation under high-pressure conditions. The tests were utilized to evaluate recovery, breakdown jitter, and electrode erosion. Single-shot data was taken to establish a baseline for breakdown jitter. Rep-rate data was compared to the single-shot data to confirm consistent performance. Electrode erosion with and without the flow-shaping elements were established. Electrode erosion with the flow-shaping elements on two different types of electrode materials was tested.

The data were analyzed utilizing standardized statistical techniques. Mean values are computed by averaging over a group of data points that have a common trait, such as operating pressure, or oil flow rate. The median value, known as the 50^{th} percentile, is plotted to show where the midpoint of the data is. Half of the observations will fall somewhere above the median while the other half will fall below the median. The quartiles are plotted, rather than the standard deviation, because the quartiles provide greater information about the skewness of the distribution, if skew exists. The range between the two quartiles plotted is called the inter-quartile range (IQR) and represents the range over which exactly half of the data falls within. The maximum and minimum values are also plotted to provide an idea of what the distribution looks like towards the extreme values.

5.2.3.1) Single-Shot Breakdown Experiments

The first experiment performed with the rep-rate DVT switch was designed to relate single-shot breakdown jitter to pressure. The experiment was performed by operating the switch at pressures between 13.79 and 17.24 MPa (2,000 to 2,500 psig) in 689.5 kPa (100 psig) increments. A series of fifty shots was taken at each pressure. Each shot was taken every 60 seconds. The experiment was repeated so that two flow rates, 22.71 and 34.07 $L \cdot min^{-1}$ (6 and 9 gpm), could be examined. The oil flow was split between the axial and coaxial ports so that about 3.785 $L \cdot min^{-1}$ (1 gpm) was allowed into the axial feed port and the remainder of the oil flow was fed into the coaxial feed port. The oil temperature was maintained around 26.7 °C (80 °F).

The breakdown voltage is plotted against the operating pressure for the 22.71 $L \cdot min^{-1}$ case in Figure 5-18, and for the 34.07 $L \cdot min^{-1}$ case in Figure 5-19. The breakdown voltage has only a very slight increase in magnitude as the operating pressure is increased in both cases, and the IQR appears to be relatively unaffected by the pressure. The maximum and minimum values for the 22.71 $L \cdot min^{-1}$ case is plotted in Figure 5-18 and appears to vary more from pressure to pressure than the values for the 34.07 $L \cdot min^{-1}$ case. Thus it appears that higher oil flow rates may tend to stabilize the extreme excursions in breakdown voltage. The largest IQR observed is about 45 kV in magnitude, which represents about 17.3% of the magnitude of the mean breakdown voltage of 260 kV. The electric field strength at 260 kV is estimated to be about 1.8 $MV \cdot cm^{-1}$ when the 1.2 mm gap spacing and the 0.105 mm gap deflection due to pressure are considered.

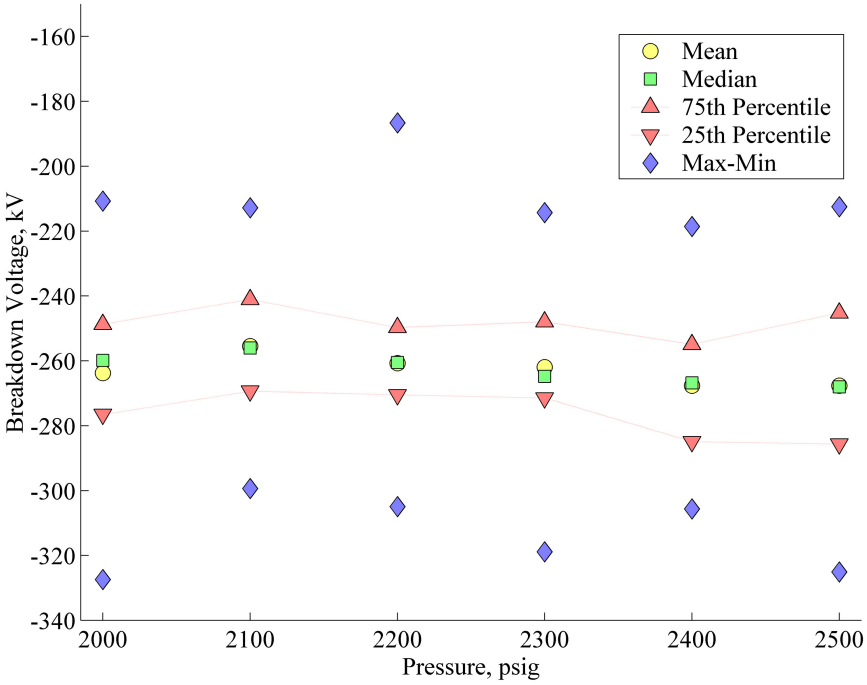

Figure 5-18. Single shot breakdown results for 22.71 L·min^{-1} (6 gpm). Coaxial flow: 5.04 gpm, Axial flow: 0.99 gpm. Oil temperature 26.7 °C. 50 shots per pressure point.

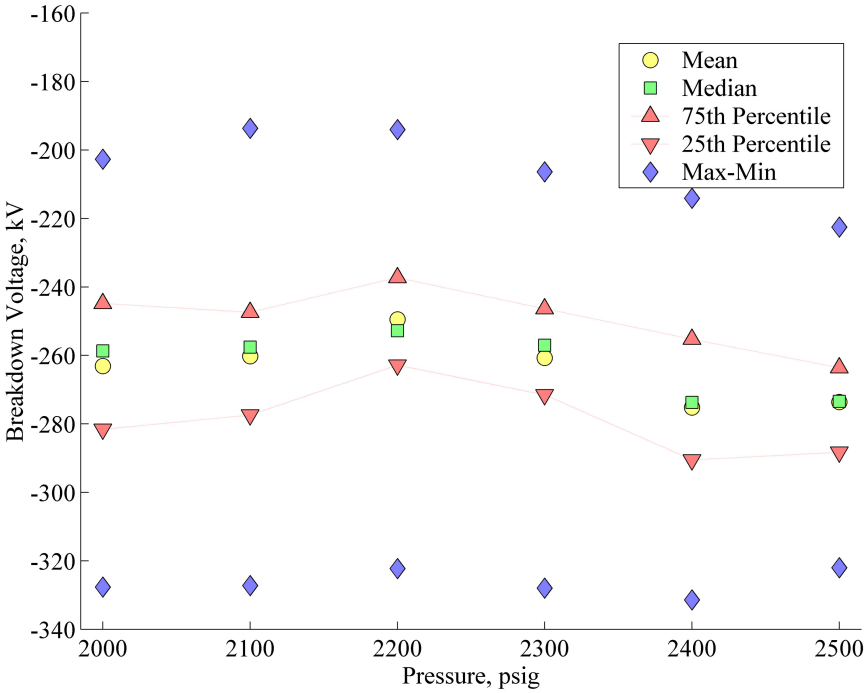

Figure 5-19. Single shot breakdown results for 34.07 L·min^{-1} (9 gpm). Coaxial flow: 8.03 gpm, Axial flow: 0.97 gpm. Oil temperature 26.7 °C. 50 shots per pressure point.

5.2.3.2) Rep-Rate Breakdown Experiments

Two separate rep-rate experiments were performed with the rep-rate DVT switch. The first experiment that is described studied the effects of varying the oil flow rate and pressure upon the mean breakdown voltage and the breakdown jitter. The experiment was conducted at four evenly-spaced flow rates from 4 to 10 gpm (2 gpm increments) and at pressures of 1,000 and 1,500 psig. The axial oil feed port was set at approximately 10% of the total oil flow volume and the remaining 90% was driven into the coaxial feed port. Tests were conducted in 100 shot bursts at 14 pps. The oil temperature was maintained at 32 °C. The cathode electrode had a total of 350,000 shots accumulated at the start of the experiment, and the anode had 500,000 accumulated shots.

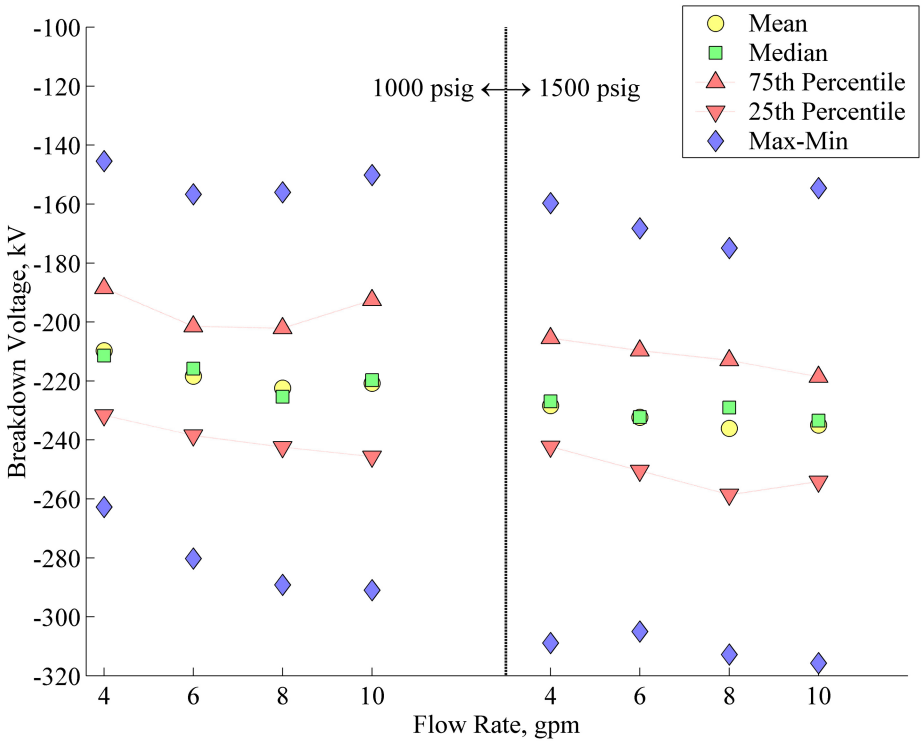

Figure 5-20. Statistics from the first rep-rate experiment. Statistics computed for 100-shot bursts at 14 pps.

The results of the first rep-rate experiment are presented in Figure 5-20 in which the breakdown voltage statistics have been plotted for both pressures as a function of the oil flow rate. The mean breakdown strength for both sets of data appears to increase slightly as the oil flow rate is increased from 4 to 10 gpm. Additionally there is a slight increase in breakdown strength for the 1,500 psig data which is probably related to the increased gap spacing deflection due to the higher operating pressure. Unlike the single-shot data presented previously, this data does not suggest in any way that higher pressure moderates or stabilizes the extreme excursions.

The second rep-rate experiment focused on the repeatability of the switch under rep-rate conditions. The experiment was performed at an oil pressure of 1,500 psig and the oil flow rate was varied between 5, 7 and 9 gpm. The experiment was repeated two additional times and the order in which the flow rates were studied was randomized. The axial oil inlet port was adjusted to be about 10% of the total flow while the coaxial inlet port was given the remaining 90% of the total flow. The oil temperature was maintained at 32 °C. Shots were recorded in bursts of 100 at 15 pps.

The statistical measures from the results of the second rep-rate experiment are presented in Figure 5-21. The data shows a slight increase in breakdown voltage magnitude as the flow rate is increased. Additionally each of the data sets appears to have a definite, and consistent peak breakdown voltage magnitude (~305 to 310 kV). The main locus of shots appears to fall within a range (*i.e.* the IQR) of about 40 kV, which represents a range of about 16.6 %. The rep-rate IQR agrees reasonably with the single-shot IQR which suggests the switch is fully recovered at 15 pps. In all cases the average

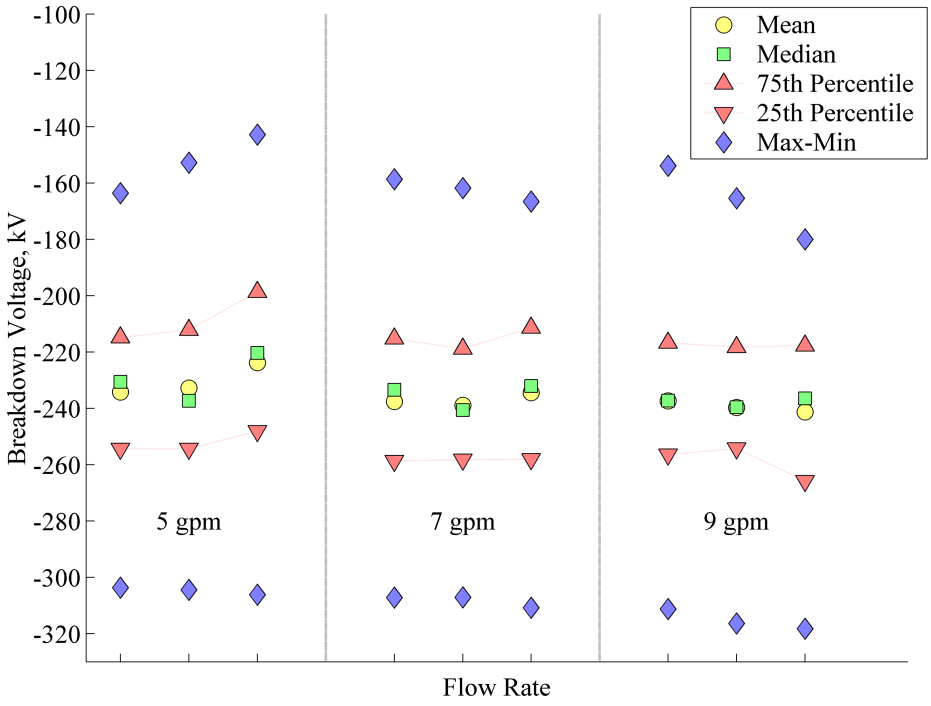

Figure 5-21. Statistics from the second rep-rate experiment. Statistics computed for 100-shot bursts at 15 pps. Oil pressure is 1,500 psig.

overall range appears to be very weakly related to the oil flow rate, with decreasing total range associated with increasing total flow rate.

5.2.3.3) Electrode Erosion Study

The rep-rate experiments were utilized to evaluate the dependence of electrode erosion upon hydrodynamic flow and the dependence of electrode material on erosion characteristics. The electrode erosion study was started by test firing the original rep-rate DVT switch design for 250,000 shots with a type-304 stainless steel anode and cathode. The oil flow shaper was not utilized during this series of test shots. The electrodes were removed after 250,000 shots and photographed. A close-up photograph of the erosion pattern on the cathode electrode is presented in Figure 5-22. The black marker in the

photograph is 1 cm in height. The total height of the erosion band, minus some the outlying discharge sites, is 1.4 cm.

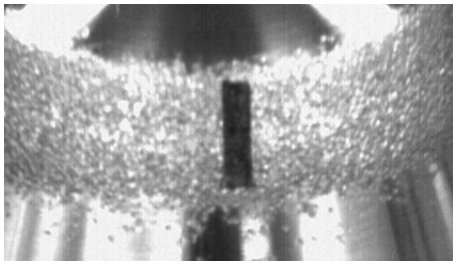

Figure 5-22. Photograph of the first type-304 stainless steel cathode following 250,000 shots.

A second type-304 stainless steel electrode was installed in the updated rep-rate DVT switch design, which included the oil flow shaper elements. The switch was test fired 150,000 times under comparable conditions to the first erosion test series. A photograph of the second stainless steel cathode is presented in Figure 5-23, in which the black marker is again 1 cm in height. The second electrode has visibly fewer outlying points (only one is visible in Figure 5-23), and the width of the erosion band has decreased to 1 cm, representing a 28% decrease in height when the oil flow shaper was installed.

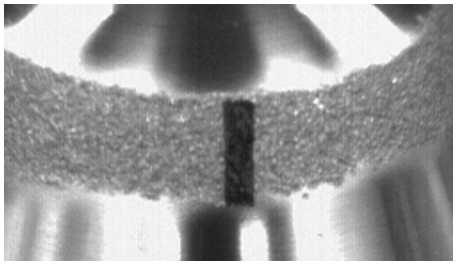

Figure 5-23. Photograph of the second type-304 stainless steel cathode following 1250,000 shots.

The effects of electrode material were studied by attempting to compare the erosion on a set of Elkonite electrodes to the erosion on a set of stainless steel electrodes. The tests on Elkonite were performed with the oil flow shaper elements and under similar conditions to the second stainless steel electrode trials (variable oil flow rate, pressures to

1,500 psig). The tests were concluded after approximately 6,000 shots because very rapid and dramatic increases in the switch pressure were noted during bursts of 1,000 shots. A photograph of the cathode electrode is shown in Figure 5-24. Given the appearance of the erosion, it became evident that the rapid increases in pressure were the result of small pieces of eroded material becoming trapped in the down-stream needle valve, resulting in stepped increases in switch pressure.

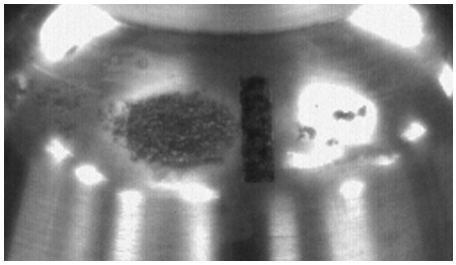

Figure 5-24. Photograph of the Elkonite cathode following approximately 6,000 shots.

The erosion of stainless steel under pulsed repetitive conditions in pressurized, flowing oil is superior to Elkonite under the same conditions. The durability of the stainless steel material is significantly greater under the types of mechanical stresses that are generated by arc discharges in liquids. The surface characteristics of the type-304 stainless steel electrodes also suggested much smoother wear than the Elkonite.

5.3. References

[1] Data sheet, *Lexan 103 resin*, General Electric Co., Pittsfield, 1995.

[2] Data sheet, *Torlon polyamide-imide design guide*, Solvay Advanced Polymers, 2003.

[3] F. B. Seely and J. O. Smith, "*Resistance of Materials, 4th Ed.*," John Wiley and Sons Inc., New York 1956, pp. 39 – 42.

[4] Data sheet, PEEK material properties guide, Victrex PLC, Lancashire, 2003.

Chapter 6. Conclusions

A test stand for studying switching performance in pressurized, flowing oil dielectrics has been successfully designed and fabricated. Two switches have been designed and operated in the test stand to demonstrate rep-rate breakdown and switch recovery in high-pressure oil. The results of the experiments suggest that oil flow dynamics play a particularly important role in the statistical spread of the breakdown process and that through careful design and tuning the high-pressure oil switch technology is capable of medium-energy, high rep-rate operation with jitter in the range of ±8% of the mean breakdown voltage or less.

A pulse modulator was developed to pulse charge the test switches to high-voltage. The modulator utilized a thyratron-switched capacitor bank, storing 250 J at 25 kV, to drive the primary winding of a pulse transformer. The pulse transformer pulse-charged the water PFL to 250 kV in 2.547 μs through the leakage inductance. The test switches discharged the PFL into a series of high-voltage coaxial cables that terminated into a high-voltage, low-inductance water resistor.

The pulse transformer was modified to include a core-reset winding. A third winding was added to the pulse transformer and a core-reset power supply drove current through the third winding to provide the reset magnetic field. The core-reset power supply was designed and fabricated with a pulse filter to block the modulator discharge. The core-reset circuit has been tested with the system operating in rep-rate bursts to 100 pps.

The water PFL was refurbished with a series of insulator bushings. The bushings were designed with the use of electrostatic models to ensure flashover-free operation for at

least 10^8 shots, based on calculations of flashover probability. The simulations were further utilized to verify bushing integrity in the cases that either oil or air become trapped on the lower surface of the upper bushing. Design improvements were incorporated into the newly fabricated bushings, including angled water ports to reduce trapped air pockets, an improved mounting structure, and the use of advanced polymers.

A high-performance flowing load resistor was designed and fabricated. The load resistor was designed for minimal inductance to minimize the L/R time constant. A wide, parallel-plate geometry was selected for its low-inductance properties. The load resistor has been demonstrated for a large number of 1,000-shot bursts at 15 pps.

A rep-rate switch was designed fabricated to develop some initial data on the breakdown performance of poly-α olefin oil. Three electrode materials were tested at pressures up to 1,500 psig and rep-rates up to 20 pps. The two types of stainless steel utilized were found to exhibit good erosion characteristics. A set of Elkonite electrodes was also tested, also with good erosion characteristics. All of the tests performed with the rep-rate switch were in 10-shot bursts.

The rep-rate DVT switch was modified to incorporate design enhancements. A number of mechanical problems were discovered that prevented the DVT switch from operating in a manner consistent with the design goals. The mechanical failure in two areas of the switch prompted a redesign of the switch receiver, featuring stress-reducing geometry modifications and improved fixturing techniques. Current gaskets were also added to components that thread together to eliminate the formation of carbon within the switch. The plastic envelope was characterized on the bench to determine the degree of axial elongation at various pressures within the operating pressure range.

Tests performed with the rep-rate switch provided initial data for breakdown and erosion. The breakdown data suggested that for an unoptimized design, operating in short bursts, a significant number of misfires occur. When the bursts with misfires are ignored the typical jitter (1-σ range) is on the order of ±13%. The more important results were related to electrode erosion. The erosion tests revealed that a typical stainless steel (type-304) would perform on par with a hardened stainless steel (17-4 precipitation hardened). The tests also revealed that Elkonite, in short bursts of shots, can be expected to perform reasonably well for at least about 1,000 shots.

The rep-rate DVT switch provided by far the most important data. The breakdown voltage was analyzed for a number of different hydraulic parameters to ascertain any dependence of breakdown characteristics upon oil flow or pressure. Pressure was expected to increase the breakdown voltage by small amounts for increasing pressure due to the elongation of the plastic envelope at higher pressures. The data presented suggests that this is indeed the case—as the pressure is increased the breakdown voltage appears to follow linearly. The breakdown voltage dependence on pressure is relatively weak, however, resulting in less than a 10 kV increase in breakdown voltage magnitude, from 260 kV to 270 kV, for a pressure increase from 2,000 to 2,500 psig respectively, under single-shot conditions. Oil flow was found to have nearly as much effect on the breakdown strength of the oil as the oil pressure. In the first rep-rate experiment reported for the DVT switch, a 6 gpm increase in the oil flow rate caused an increase in breakdown voltage of about 10 kV from 210 kV to 220 kV at 1,000 psig and 230 kV to 240 kV at 1,500 psig.

Electrode erosion in the rep-rate DVT switch was characterized for two different materials and two different dynamic oil flow scenarios. The dynamic flow study underscored the importance of oil flow dynamics to the characteristics of the erosion pattern. Increased oil flow rates and reduced turbulent rotation reduces the height of the discharge band under similar test conditions. The electrode material tests showed stainless steel electrodes were superior for long-duration bursts. The Elkonite electrodes were found to undergo surface fractures resulting in rapid electrode erosion, probably due to the metallurgical properties of Elkonite. The Elkonite therefore performs satisfactorily only in short bursts at high-pressure, as found with the first rep-rate switch.

Appendix A. LTSpice Netlist of the Test Stand

Full system simulations were performed in LTSpice utilizing equivalent circuits for several of the components of the system, including the pulse transformer, the high-pressure switch, and the load resistor. The netlist used for simulation is provided as well as circuit diagrams of the equivalent circuits utilized.

A.1. Netlist

```
* Full System Simulation: SystemSim-1b.cir
*  Simulation includes improved models for:
*  - Diode snubber
*  - Pulse transformer
*  - High pressure switch
*
* P. Norgard
* 17 April 2006

**********************************************************************
* Modulator model
Rthy    1  0  10e-3

Cbank   1  2  810e-9 Rser=50e-3 Lser=8e-9 IC=25e3

Dsnub   2  20 D1N5603
Rsnub   20 0  1.4
.model  D1N5603 D(BV=35e3 CJO=6e-12 VJ=70 IS=50e-6)

**********************************************************************
* Pulse transformer model
*  Lp = 78 uH
*  Ls = 7.3 mH
*  Ll = 1.703 uH
*  k = 0.98895
*  Lm = 77.2 uH
Lleakp  2  3  851.5e-9 Rser=15.88e-3 IC=0
Lmag    3  0  75.2e-6 IC=0
Lleaks  3  4  851.5e-9 Rser=1.588e-3 IC=0
Lpri    4  0  76.1e-6 IC=0
Lsec    5  0  7.61e-3 IC=0
Ktrn    Lpri  Lsec  1

**********************************************************************
* Pulse Forming Line model
Opfl    5  0  6  0  PFL IC=0,0,0,0
.model PFL LTRA(Len=1.1711 L=142.88e-9 C=6.1865e-9 R=0 G=0)

**********************************************************************
* High-pressure switch model
```

```
Lk       6   7 25.7e-9
Ckg      7   0 74.1e-12 IC=0
Cak      7   9 78.1e-12 IC=0
Cag      9   0 79.3e-12 IC=0
Sarc     7   8 y 0 Sarcm
.model Sarcm SW(Ron=25e-3 Roff=1e6 Vt=1 Vh=0)
Larc     8   9 3e-9
*              Time to Breakdown
*                       |
*                       |
Varc     y   0 pulse(0 2 2.028e-6 2e-9 2e-9 5e-6 50e-3)
La       9 10 36.9e-9

*********************************************************************
* Output network model
Ofline  10 0 11 0 FEED IC=0,0,0,0
.model FEED LTRA(Len=14.325 L=21.063e-9 C=1.2132e-9 R=0 G=0)

*********************************************************************
* Load resistor model
Lload  11 12 38.5e-9
Rload  12 0 4.2

*********************************************************************
* Control Commands
.tran 0.1e-9 4e-6 0 0.1e-9 UIC
.end
```

A.2. Equivalent Circuits

A.2.1. Pulse Transformer

An equivalent model of the pulse transformer was developed based on the equivalent-T model. The leakage inductance was estimated by analyzing the resultant frequency of a capacitive discharge using known capacitors. A schematic diagram of the pulse transformer is presented in Figure A-1 utilizing the labels found within the netlist.

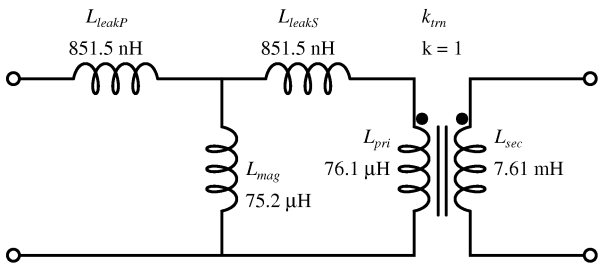

Figure A-1. Schematic diagram of the equivalent-T model of the pulse transformer.

A.2.2. High-Pressure Switch

The equivalent circuit of the DVT switch is presented in Figure A-2. The three capacitances were estimated within an electrostatic simulation of the electrodes, performed with the Ansoft Maxwell 2D electrostatic simulator. Typical gap spacings were inserted into the model. The anode and cathode inductances were estimated as the total coaxial inductance associated with the geometry of the anode and cathode structures.

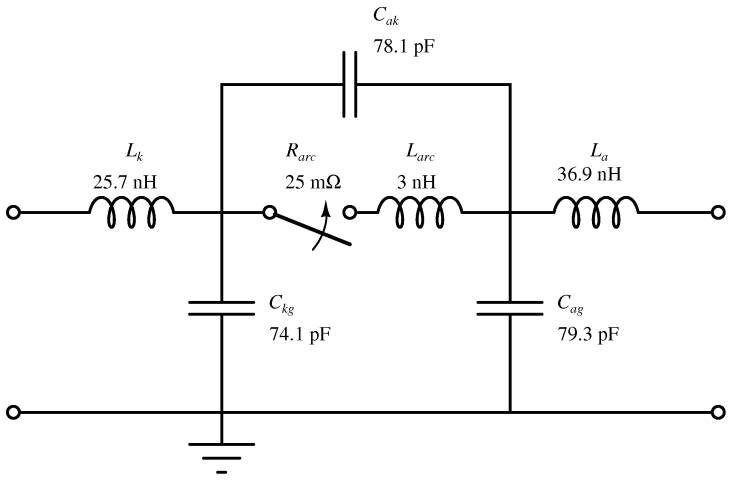

Figure A-2. Equivalent model of the high-pressure DVT switch.

A.2.3. Load Resistor

An equivalent model of the load resistor is presented in Figure A-3. The load resistor was modeled as an L-R network because the complete model of the load, which is composed of a number of parallel and series capacitive elements, simplifies into the model presented in Figure A-3. The voltages reflected from the load back towards the switch agree well with observed voltage reflections.

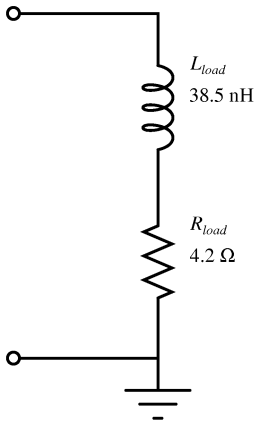

Figure A-3. Schematic diagram of the equivalent load resistor model.

Appendix B. Dielectric Test Switch Drawings

The original line drawings of the dielectric test switch are presented in this appendix. The eight polymer bolts that hold the switch together were never explicitly drawn—their dimensions were decided upon during the machining phase of switch fabrication.

There are several notable changes to the switch that are not reflected in these drawings that are related to the bolt failures. On page 1 of 6 (bottom plate, top view) the 9/16 inch holes on the 4 inch radius were increased in diameter to 7/8 inch to accommodate the increased diameter switch clamping bolts. Similarly on page 3 of 6 (top plate, bottom view) the 9/16”-18 threaded holes were increased to 7/8”-9 (UNC) threads for the new bolts. Finally on page 5 of 6 (switch housing) an o-ring groove was added to the top and bottom of the housing just outside of the 2 inch inner diameter to reduce the cross sectional area exposed to high pressure oil.

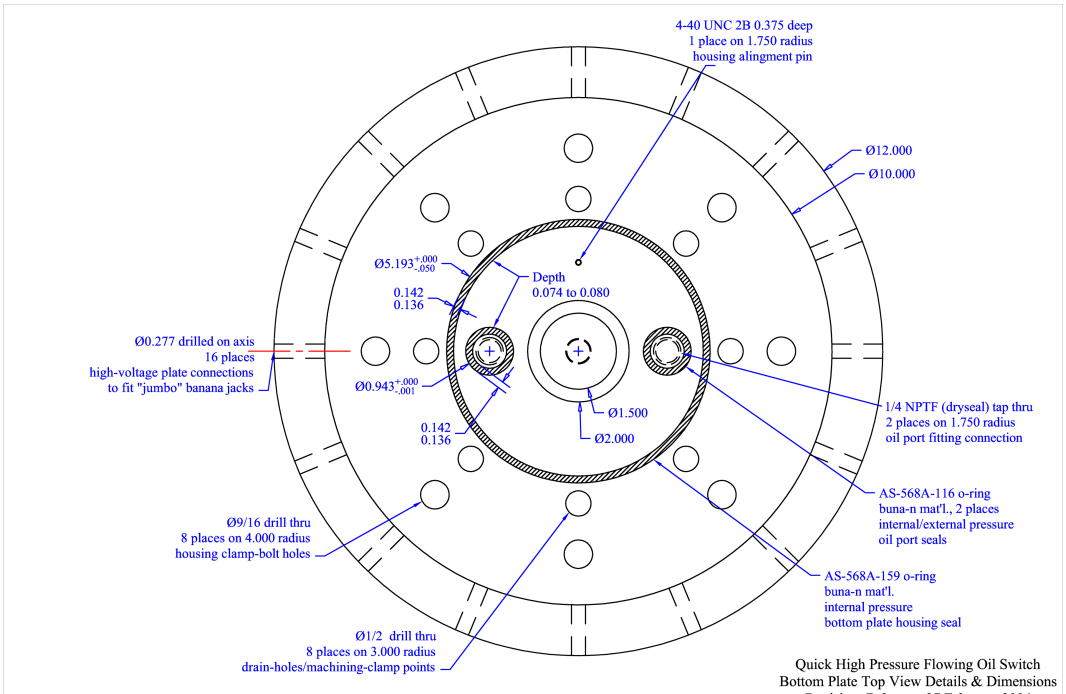

Quick High Pressure Flowing Oil Switch
Bottom Plate Top View Details & Dimensions
Revision: B-2 27 February 2004
Scale: none Page 1 of 6

Peter Norgard
University of Missouri - Columbia
Columbia, Missouri 65211
Work sponsored by the United States Air Force.

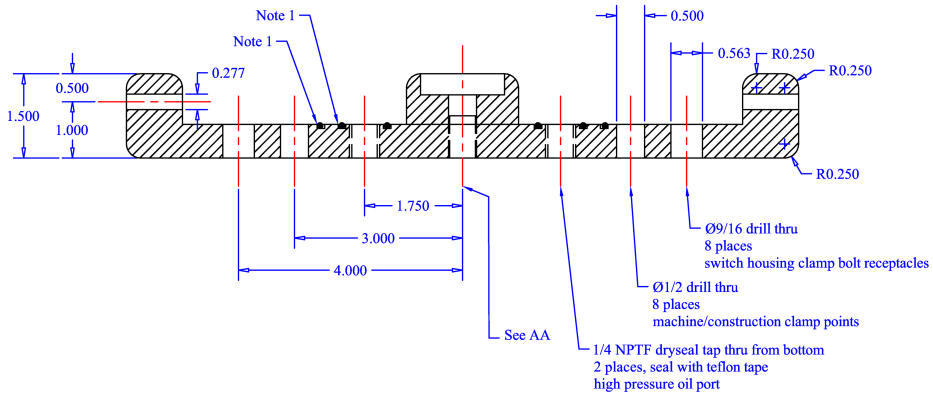

AA

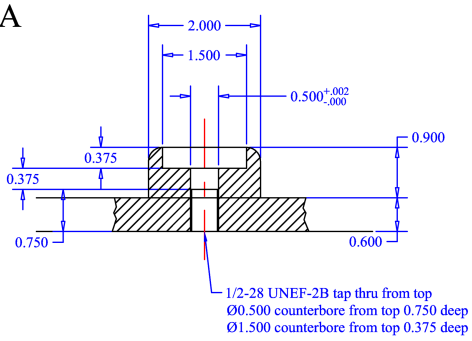

Notes:
1. See page 1 for o-ring groove dimensions, break o-ring groove edges
2. Material is Aluminum alloy 6061
3. Unless noted, all tolerances ±0.01
4. All dimensions in inches

Quick High Pressure Flowing Oil Switch
Bottom Plate Profile View Details & Dimensions
Revision: B-2 28 February 2004
Scale: none Page 2 of 6

Peter Norgard
University of Missouri - Columbia
Columbia, Missouri 65211
Work sponsored by the United States Air Force.

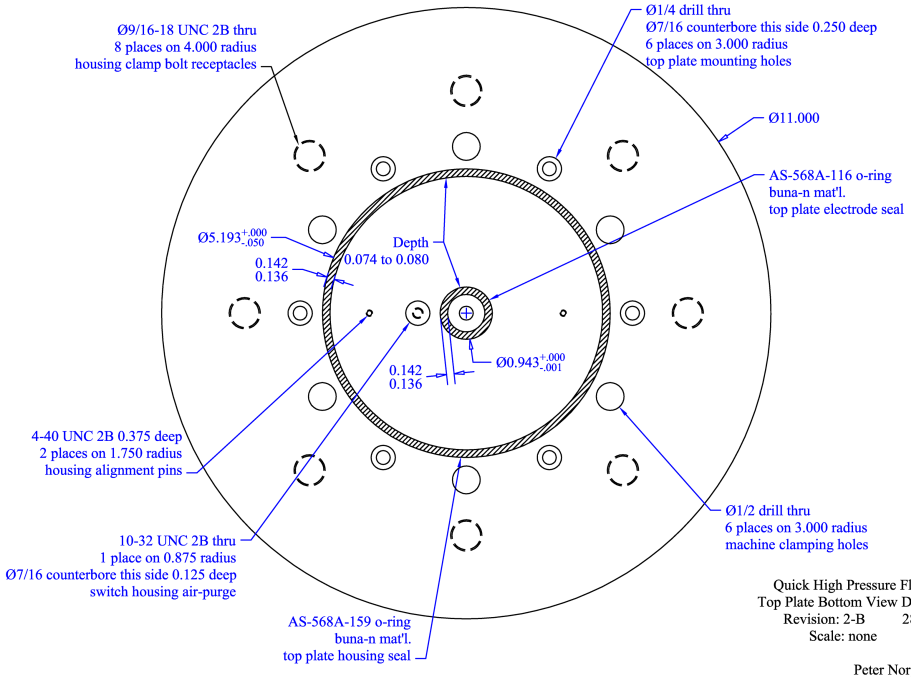

Quick High Pressure Flowing Oil Switch
Top Plate Bottom View Details & Dimensions
Revision: 2-B 28 February 2004
Scale: none Page 3 of 6

Peter Norgard
University of Missouri - Columbia
Columbia, Missouri 65211
Work sponsored by the United States Air Force.

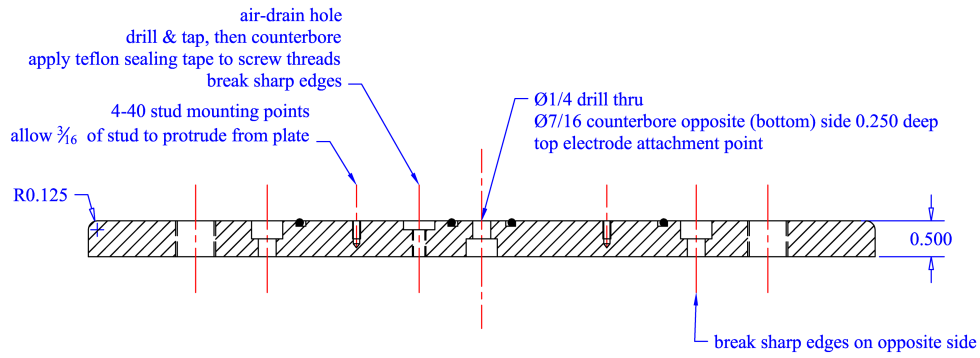

Quick High Pressure Flowing Oil Switch
Top Plate Profile View Details & Dimensions
Revision: 2-B 28 February 2004
Scale: none Page 4 of 6

Peter Norgard
University of Missouri - Columbia
Columbia, Missouri 65211
Work sponsored by the United States Air Force.

Notes:
1. Unless noted, all tolerances ±0.01
2. All dimensions given in inches
3. Top plate constructed from Aluminum alloy 6061

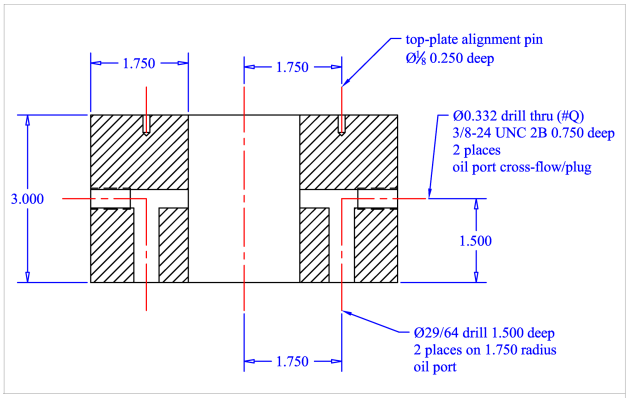

Notes:
1. Unless noted, all tolerances ±0.01
2. All dimensions given in inches
3. Housing material is General Electric Lexan

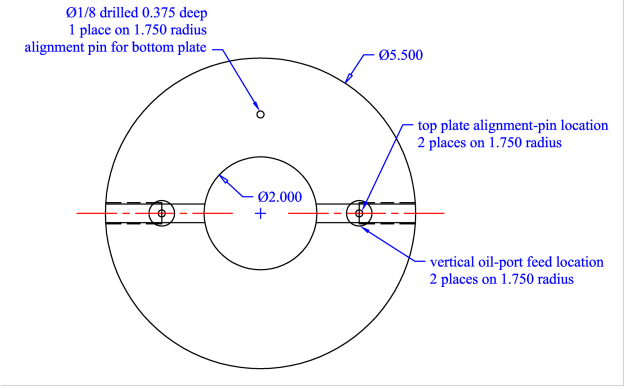

Quick High Pressure Flowing Oil Switch
Switch Housing Details & Dimensions
Revision: B-2 28 February 2004
Scale: none Page 5 of 6

Peter Norgard
University of Missouri - Columbia
Columbia, Missouri 65211
Work sponsored by the United States Air Force.

Top-Plate Electrode

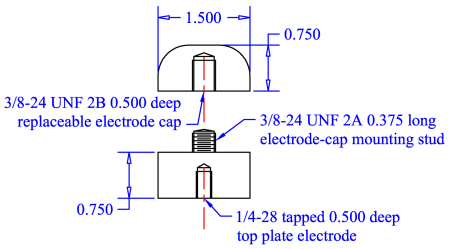

Bottom-Plate Electrode Cap

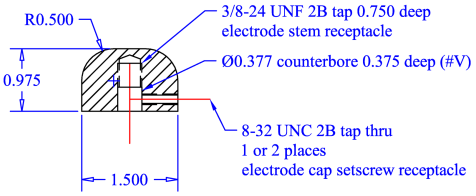

Notes:
1. Unless noted, all tolerances ±0.01
2. All dimensions given in inches
3. Electrode stems/bases composed of Stainless Steel alloy 17-4 precipitation hardened OR alloy 304
4. Electrode caps composed of Elkonite alloy K33 (or equivalent) OR Stainless Steel alloy 17-4 precipitation hardened

Bottom-Plate Electrode Adjustment Stem

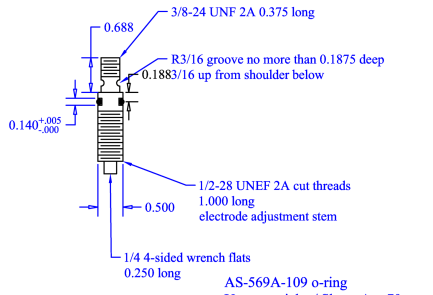

Quick High Pressure Flowing Oil Switch
Electrode (Top & Bottom) Details & Dimensions
Revision: B-2 28 February 2004
Scale: none Page 6 of 6

Peter Norgard
University of Missouri - Columbia
Columbia, Missouri 65211
Work sponsored by the United States Air Force.

Appendix C. DVT Switch Drawings

The DVT switch was developed as a partnership between the University of Missouri – Columbia and Alpha Omega Power Technologies, L.L.C. Alpha Omega Power Technologies, or AOPT, provided the mechanical analysis and machine-shop drawings while the University of Missouri performed electrical and electrostatic modeling, as well as general conceptual oversight.

The final drawings utilized for fabrication of the optimized high pressure switch are presented in this appendix. The appendix begins with assembly drawings to show the relative locations of all of the parts. The assembly drawings are followed by all of the machined switch components.

PROPRIETARY INFORMATION

REVISIONS			
REV	DESCRIPTION	DATE	APPROVED
-	BASELINE	03/12/04	
A	MODS TO MC-104 AND NEW MC-115	09/19/04	
B	MC-104 REPLACED WITH MC-117	10/07/04	
C	ELECTRODE SECTIONAL UPDATE	01/05/05	

NOTES:

1. ITEM 11 ATTACHES TO BLUMLEIN INNER CONDUCTOR WITH EXISTING SHCS.

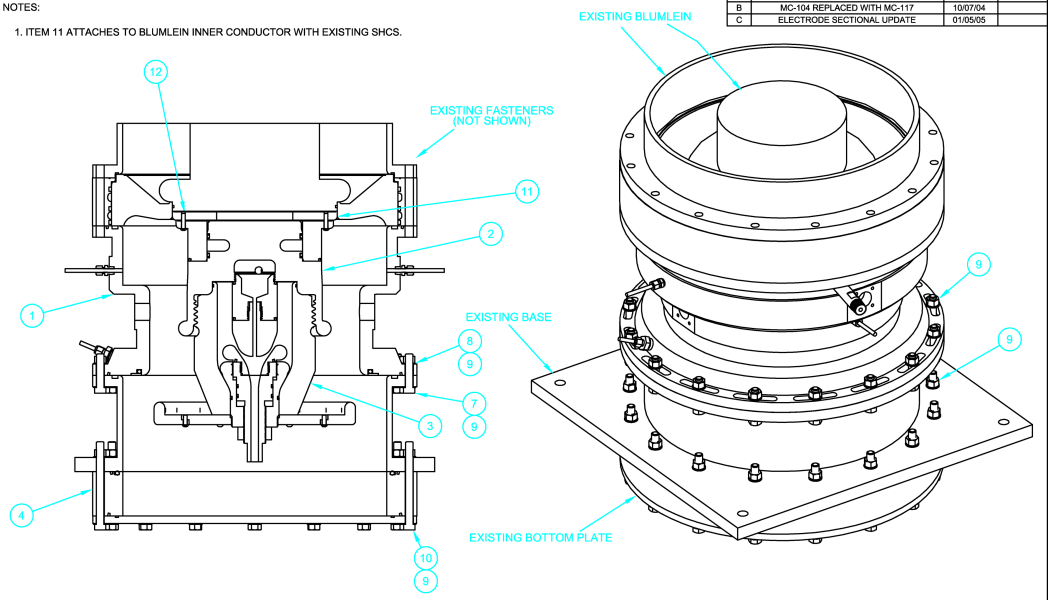

ITEM	QTY	UOM	PART NUMBER	DESCRIPTION	SUPPLIER
12	8	EA	511-1420-1-2AA2A	1/4-20 BHCS X 1" LONG, S/S	BARNHILL BOLT
11	1	EA	HPS1-MC-101	EXTENSION	MACHINING
10	16	EA	52-12-512-2AAAA	1/2-13 X 5.5 LONG HEX BOLT, S/S	BARNHILL BOLT
9	32	EA	202-12-A-2AAAA	1/2-13 HEX NUT, S/S	BARNHILL BOLT
8	64	EA	306-12-A-2AAAA-C816	1/2 FLAT WASHER, REDUCED OD, S/S	BARNHILL BOLT
7	16	EA	52-12-214-2AAAA	1/2-13 X 2.25 LONG HEX BOLT, S/S	BARNHILL BOLT
6	4	EA	2-115	O-RING, BUNA-N, 70 DUROMETER	SOUTHWEST SEALS
5	2	EA	HPS1-MC-113	FLOW TUBE	MACHINING
4	1	EA	HPS1-AS-104	ASSEMBLY, AUXILLARY EXTENSION TUBE	ALPHA-OMEGA
3	1	EA	HPS1-AS-103	SWITCH GROUND SIDE ASSEMBLY	ALPHA-OMEGA
2	1	EA	HPS1-AS-102	SWITCH CHARGE SIDE ASSEMBLY	ALPHA-OMEGA
1	1	EA	HPS1-AS-101	EXTENSION ASSEMBLY	ALPHA-OMEGA

Alpha-Omega Power Technologies, LLC.
3701 Hawkins Street NE
Albuquerque, NM 87109

TITLE: ATTACHED TOP ASSEMBLY

SIZE	DWG NO	REV
A	HPS1-AS-100	C

PROJECT	SCALE	SHEET
HPS1	NONE	1 OF 2

PROPRIETARY INFORMATION

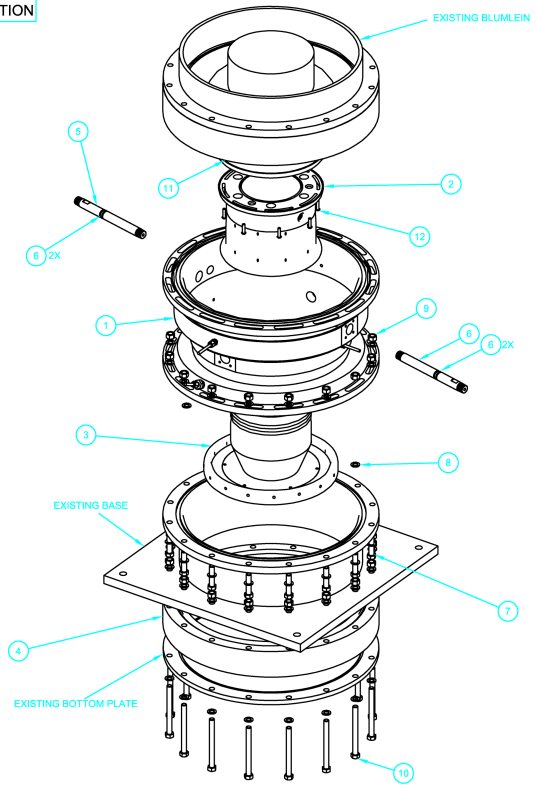

SIZE	DWG NO	REV
A	HPS1-AS-100	C

PROJECT	SCALE	SHEET
HPS1	NONE	2 OF 2

PROPRIETARY INFORMATION

REVISIONS			
REV	DESCRIPTION	DATE	APPROVED
-	BASELINE	03/12/04	
A	GROUND ELECTRODE MOD AND BAL SEAL	01/05/05	

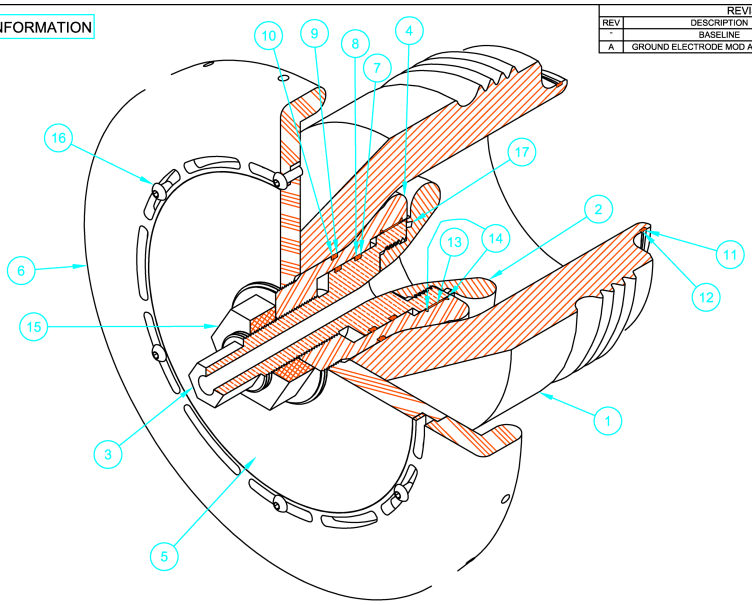

ITEM	QTY	UOM	PART NUMBER	DESCRIPTION	VENDOR
17	8	IN	BG 20	EMI GASKET	BAL-SEAL
16	6	EA	511-1420-58-2AA2A	1/4-20 PHCS X 5/8 LONG, S/S	BARNHILL BOLT
15	1	EA	217-112-A-01AAA	1 1/2 Hex Thin/Jam Nut,NF, Steel,Zinc	BARNHILL BOLT
14	2	EA		SNAP RING, FROM BL70N	MULTICONTACT
13	1	EA		MULTILAM STRIP, FROM BL70N	MULTICONTACT
12	1	EA	8-161	PAR BAK, 80 DUROMETER	SOUTHWEST SEALS
11	1	EA	2-161	O-RING, BUNA-N, 70 DUROMETER	SOUTHWEST SEALS
10	1	EA	8-234	PAR BAK, 80 DUROMETER	SOUTHWEST SEALS
9	1	EA	2-234	O-RING, BUNA-N, 70 DUROMETER	SOUTHWEST SEALS
8	2	EA	8-227	PAR BAK, 80 DUROMETER	SOUTHWEST SEALS
7	2	EA	2-227	O-RING, BUNA-N, 70 DUROMETER	SOUTHWEST SEALS
6	1	EA	HPS1-MC-112	FIELD SHAPER MODIFICATION	MACHINING
5	1	EA	HPS1-MC-111	FIELD SHAPER RING ADAPTER	MACHINING
4	1	EA	HPS1-MC-110	GROUND ELECTODE COLLAR	MACHINING
3	1	EA	HPS1-MC-109	GROUND ADJUSTER	MACHINING
2	1	EA	HPS1-MC-108	GROUND ELECTRODE	MACHINING
1	1	EA	HPS1-MC-105	SWITCH HOUSING	MACHINING

Alpha-Omega Power Technologies, LLC.
3701 Hawkins Street NE
Albuquerque, NM 87109

TITLE: SWITCH GROUND SIDE ASSEMBLY

SIZE	DWG NO	REV
A	HPS1-AS-103	A

PROJECT: HPS1 | SCALE: NONE | SHEET: 1 OF 1

PROPRIETARY INFORMATION

REVISIONS			
REV	DESCRIPTION	DATE	APPROVED
-	BASELINE	03/12/04	
A	UPDATED PER LAYOUT CHANGES AND DESCRIBED ASSEMBLY/DISASSEMBLY	09/17/04	
B	MC-104 REPLACED BY MC-117	10/07/04	
C	UPDATED 106/7 ADDED BAL SEAL	01/05/05	

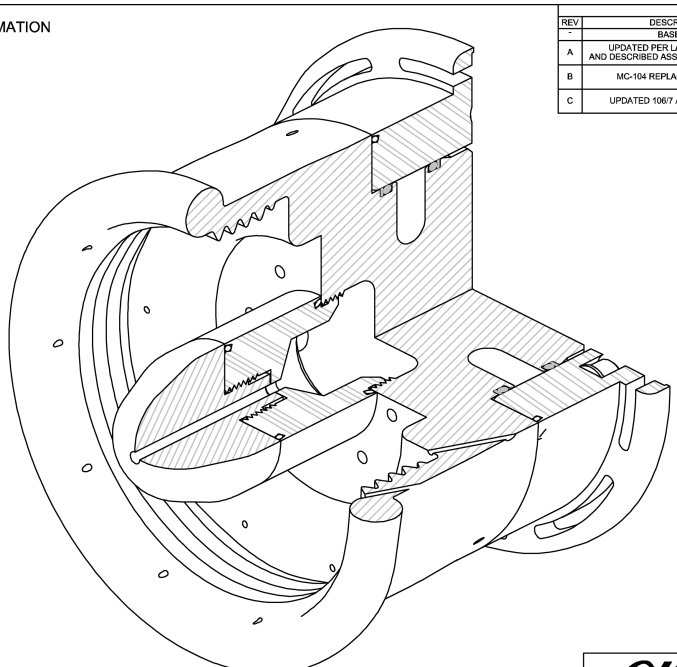

ITEM	QTY	UOM	PART NUMBER	DESCRIPTION	SPECIFICATION
11	14	IN	BG 20	EMI GASKET	BAL-SEAL
10	6	EA	306-12-A-2AAAA-C816	1/2 FLAT WASHER, REDUCED OD, S/S	BARNHILL BOLT
9	6	EA	504-1220-3-AAA2A	1/2-20 x 3 Socket Head Cap Screw,S/S, Hex Drive	BARNHILL BOLT
8	3	EA	90298A735	S/S Shoulder Screw 1/2" Dia, 6" L Shoulder, 3/8"-16	MCMASTER-CARR
7	A/R	EA	n/a	COPPER WOUND CONDUCTIVE GASKET	BAL-SEAL
6	2	EA	8-361	PAR BAK, 80 DUROMETER	SOUTHWEST SEALS
5	2	EA	2-361	O-RING, BUNA-N, 70 DUROMETER	SOUTHWEST SEALS
4	1	EA	HPS1-MC-107	CHARGE ELECTRODE	MACHINING
3	1	EA	HPS1-MC-106	CHARGE ELECTRODE ADAPTER	MACHINING
2	1	EA	HPS1-MC-117	RECEIVER, SWITCH HOUSING	MACHINING
1	1	EA	HPS1-MC-115	FLOW COLLAR	MACHINING

Alpha-Omega Power Technologies, LLC.
3701 Hawkins Street NE
Albuquerque, NM 87109

TITLE: SWITCH CHARGE SIDE ASSEMBLY

SIZE	DWG NO	REV
A	HPS1-AS-102	C

PROJECT: HPS1 | SCALE: NONE | SHEET: 1 OF 4

PROPRIETARY INFORMATION

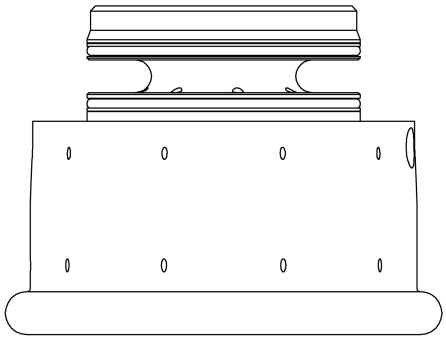

SIZE	DWG NO	REV
A	HPS1-AS-102	C
PROJECT HPS1	SCALE NONE	SHEET 2 OF 4

PROPRIETARY INFORMATION

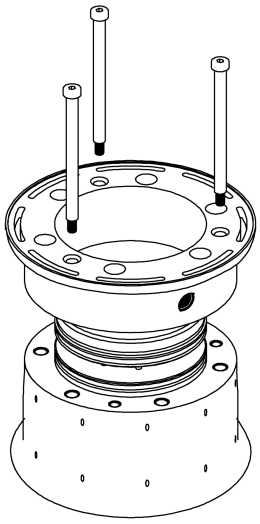

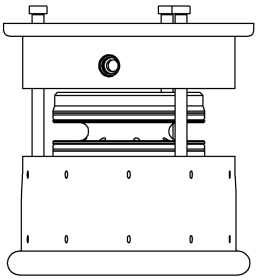

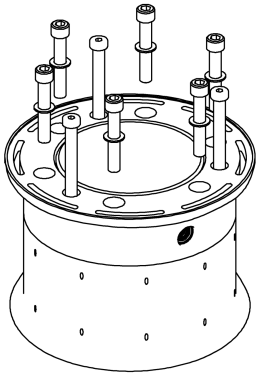

SIZE	DWG NO	REV
A	HPS1-AS-102	C
PROJECT HPS1	SCALE NONE	SHEET 3 OF 4

PROPRIETARY INFORMATION

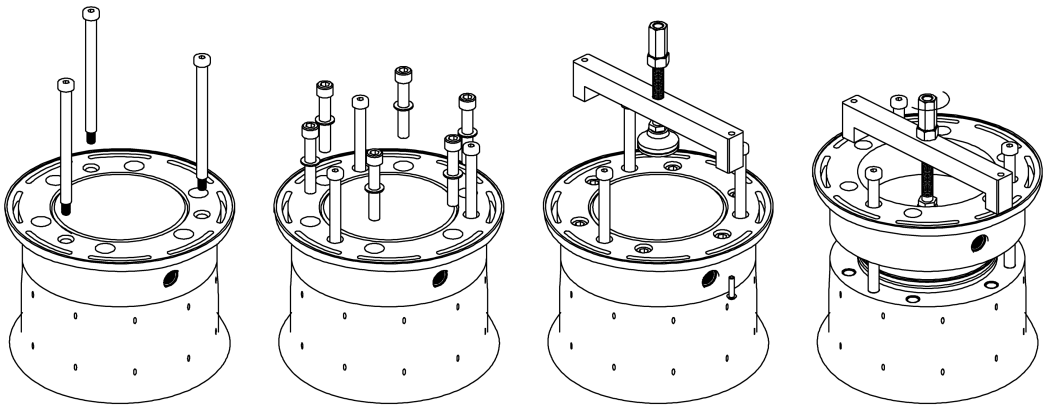

SIZE	DWG NO	REV
A	HPS1-AS-102	C
PROJECT HPS1	SCALE NONE	SHEET 4 OF 4

REVISIONS			
REV	DESCRIPTION	DATE	APPROVED
–	BASELINE	09/21/04	

NOTES:
1. MATERIAL: ALUMINUM 6061–T6.

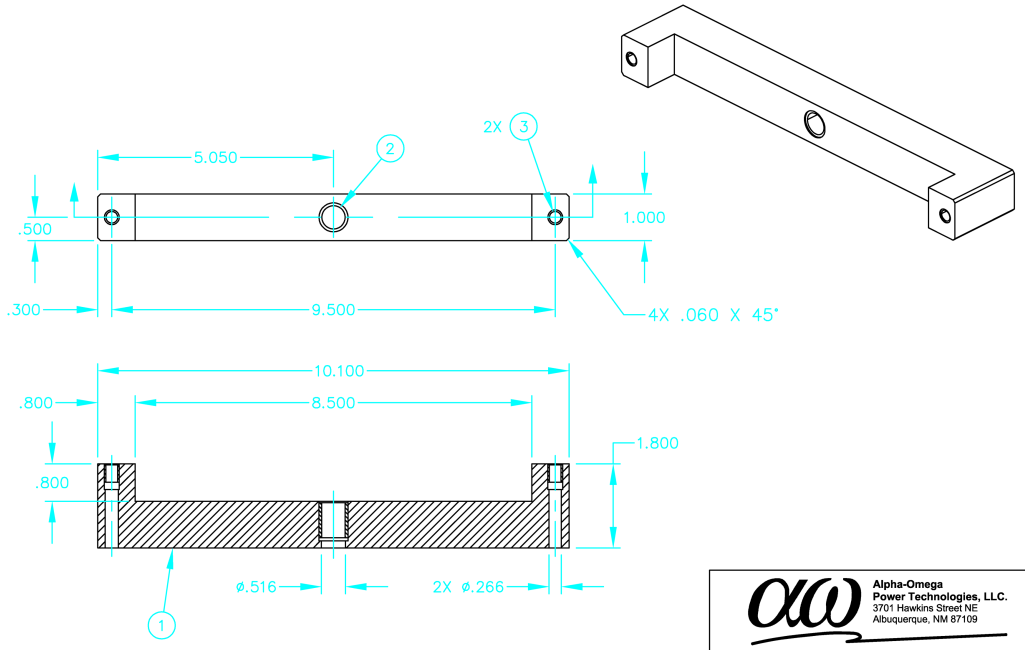

ITEM	QTY	UOM	PART NUMBER	DESCRIPTION	SPECIFICATION
3	2	EA	1185-4CN375	HELICOIL .250-20 X 1.5 DIA	X
2	1	EA	1185-8CN750	HELICOIL .500-13 X 1.5 DIA	X
1	1	EA	HPS1-MC-116	EXTRACTOR TOOL	MACHINED

Alpha-Omega
Power Technologies, LLC.
3701 Hawkins Street NE
Albuquerque, NM 87109

TITLE: EXTRACTOR TOOL

SIZE	DWG NO	REV
A	HPS1-MC-116	–
PROJECT HPS1	SCALE NONE	SHEET 1 OF 1

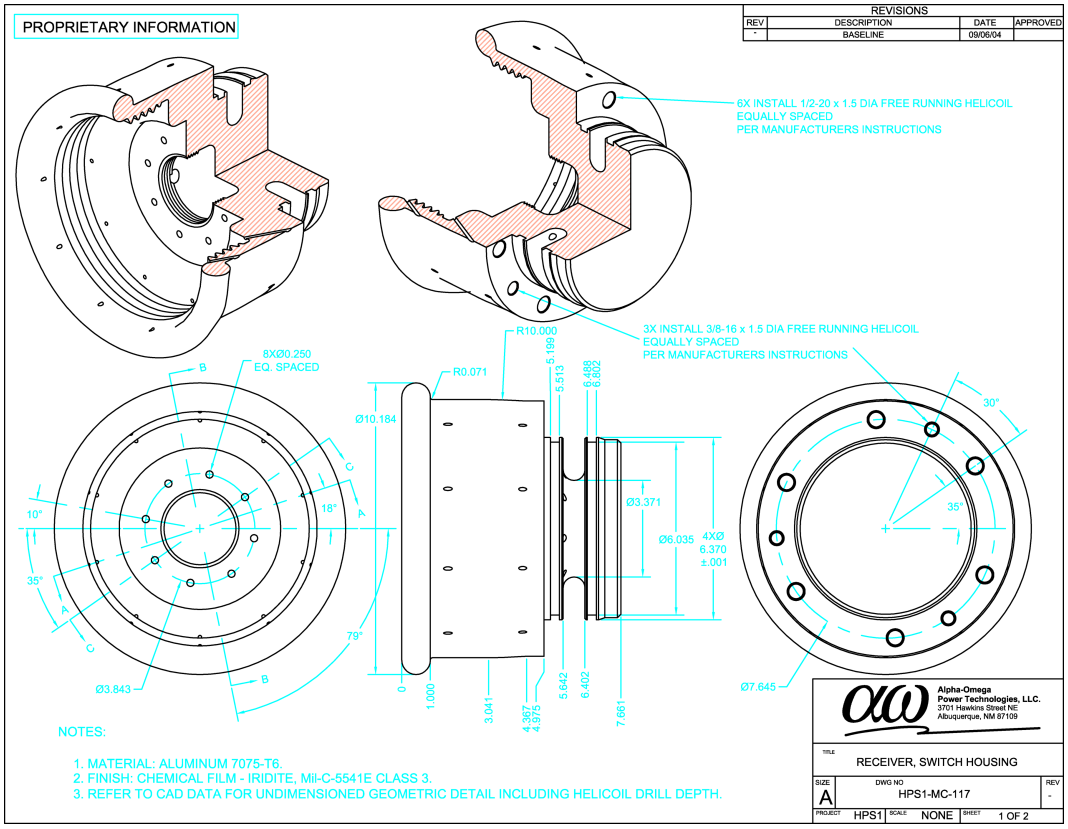
PROPRIETARY INFORMATION
REVISIONS
REV | DESCRIPTION | DATE | APPROVED
- | BASELINE | 09/06/04
6X INSTALL 1/2-20 x 1.5 DIA FREE RUNNING HELICOIL EQUALLY SPACED PER MANUFACTURERS INSTRUCTIONS
3X INSTALL 3/8-16 x 1.5 DIA FREE RUNNING HELICOIL EQUALLY SPACED PER MANUFACTURERS INSTRUCTIONS
8XØ0.250 EQ. SPACED
R10.000
R0.071
Ø10.184
Ø3.371
Ø6.035
4XØ 6.370 ±.001
Ø3.843
Ø7.645
30°
35°
10°
18°
79°
5.199
5.513
6.488
6.622
0
1.000
3.041
4.367
4.975
5.642
6.402
7.661
NOTES:
1. MATERIAL: ALUMINUM 7075-T6.
2. FINISH: CHEMICAL FILM - IRIDITE, Mil-C-5541E CLASS 3.
3. REFER TO CAD DATA FOR UNDIMENSIONED GEOMETRIC DETAIL INCLUDING HELICOIL DRILL DEPTH.
Alpha-Omega Power Technologies, LLC.
3701 Hawkins Street NE
Albuquerque, NM 87109
TITLE
RECEIVER, SWITCH HOUSING
SIZE A | DWG NO HPS1-MC-117 | REV -
PROJECT HPS1 | SCALE NONE | SHEET 1 OF 2

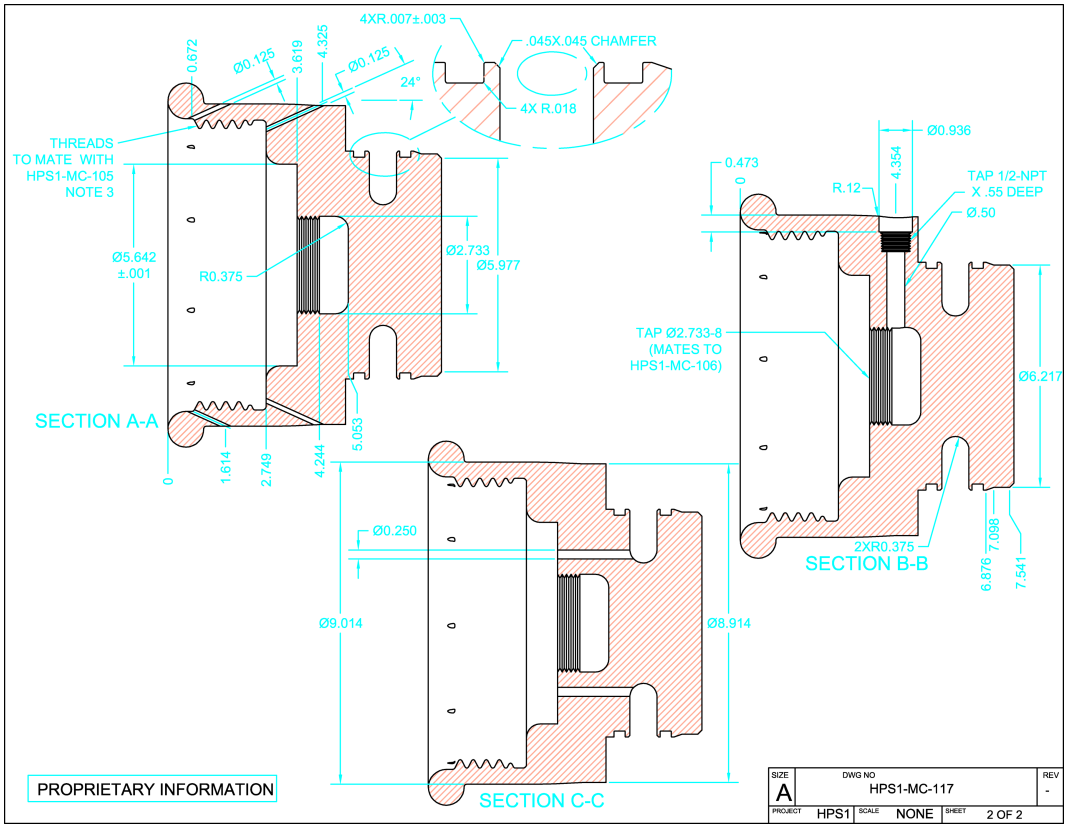
4XR.007±.003
.045X.045 CHAMFER
4X R.018
24°
0.672
Ø0.125
3.619
4.325
Ø0.125
THREADS TO MATE WITH HPS1-MC-105 NOTE 3
Ø5.642 ±.001
R0.375
Ø2.733
Ø5.977
SECTION A-A
0
1.614
2.749
4.244
5.053
Ø0.936
0.473
R.12
4.354
TAP 1/2-NPT X .55 DEEP
Ø.50
TAP Ø2.733-8 (MATES TO HPS1-MC-106)
Ø6.217
2XR0.375
SECTION B-B
6.876
7.098
7.541
Ø0.250
Ø9.014
Ø8.914
SECTION C-C
PROPRIETARY INFORMATION
SIZE A | DWG NO HPS1-MC-117 | REV -
PROJECT HPS1 | SCALE NONE | SHEET 2 OF 2

PROPRIETARY INFORMATION

REVISIONS			
REV	DESCRIPTION	DATE	APPROVED
-	BASELINE	09/17/04	

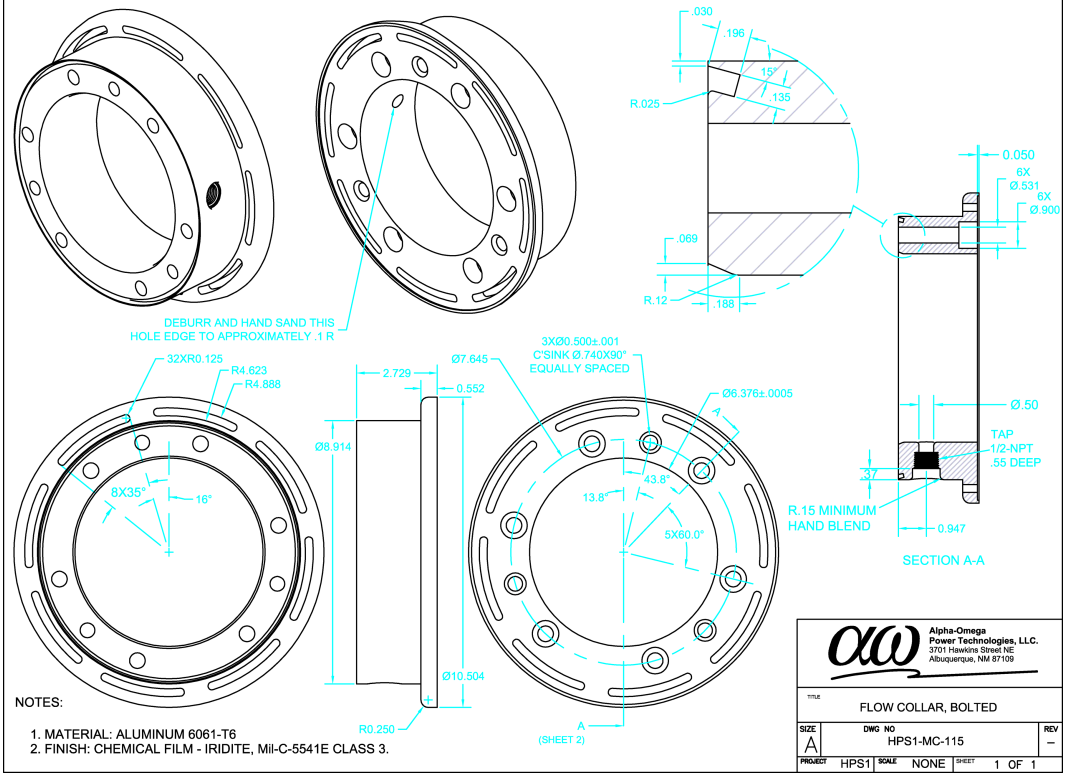

NOTES:

1. MATERIAL: ALUMINUM 6061-T6
2. FINISH: CHEMICAL FILM - IRIDITE, Mil-C-5541E CLASS 3.

Alpha-Omega
Power Technologies, LLC.
3701 Hawkins Street NE
Albuquerque, NM 87109

TITLE		
FLOW COLLAR, BOLTED		
SIZE A	DWG NO HPS1-MC-115	REV –
PROJECT HPS1	SCALE NONE	SHEET 1 OF 1

PROPRIETARY INFORMATION

REVISIONS			
REV	DESCRIPTION	DATE	APPROVED
-	BASELINE	03/12/04	

NOTES:

1. MATERIAL: ULTEM 2300.
2. REFER TO CAD DATA FOR GEOMETRIC DETAIL.

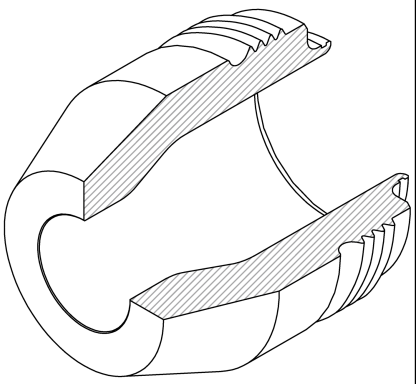

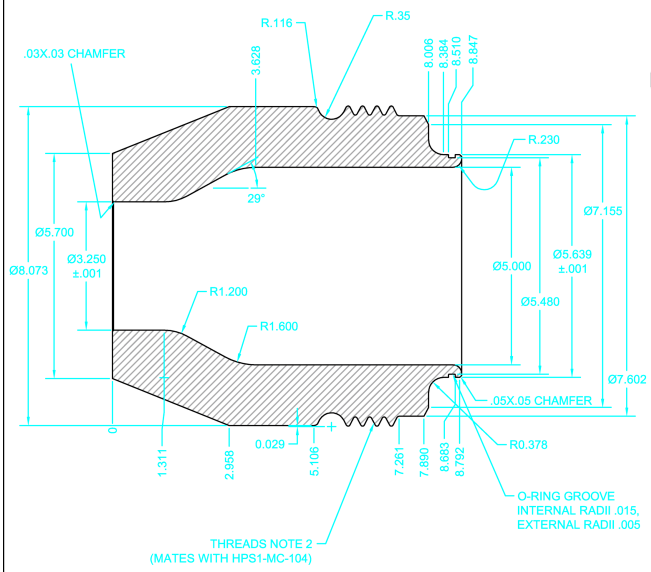

Alpha-Omega
Power Technologies, LLC.
3701 Hawkins Street NE
Albuquerque, NM 87109

TITLE		
SWITCH HOUSING		
SIZE A	DWG NO HPS1-MC-105	REV -
PROJECT HPS1	SCALE NONE	SHEET 1 OF 1

PROPRIETARY INFORMATION

REVISIONS			
REV	DESCRIPTION	DATE	APPROVED
-	BASELINE	03/12/04	
A	ADDED NYLON LOCKING FEATURE	01/05/05	
B	NIB OFF, BAL SEAL GROOVES & NOTES 2,3	02/05/05	

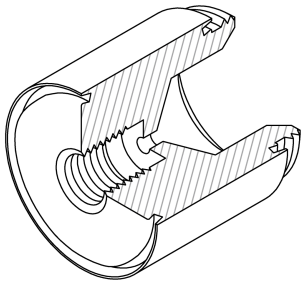

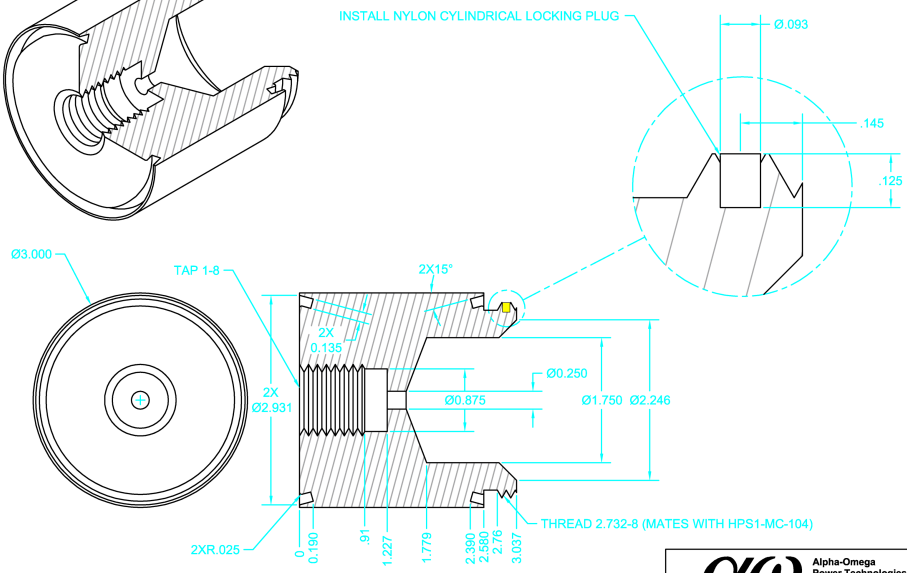

NOTES, UNLESS OTHERWISE SPECIFIED:

1. MATERIAL: 303 OR 304 STAINLESS STEEL.
2. TOLERANCES X.XXX ±.005, X.XX±.02.
3. SURFACE FINISH: 125

Alpha-Omega Power Technologies, LLC.
3701 Hawkins Street NE
Albuquerque, NM 87109

TITLE: CHARGE ELECTRODE ADAPTER

SIZE	DWG NO	REV
A	HPS1-MC-106	B

PROJECT	SCALE	SHEET
HPS1	NONE	1 OF 1

PROPRIETARY INFORMATION

REVISIONS			
REV	DESCRIPTION	DATE	APPROVED
-	BASELINE	03/12/04	
A	ADDED NYLON LOCKING FEATURE	01/05/05	
B	LENGTH MODS, NOTES 2&3	02/05/05	
C	Nose cone installation features	02/13/05	

NOTES:
1. MATERIAL: COPPER-TUNGSTEN CONTACT RAY AT 341-4828.
2. TOLERANCES X.XXX ±.005, X.XX±.02.
3. SURFACE FINISH: 125

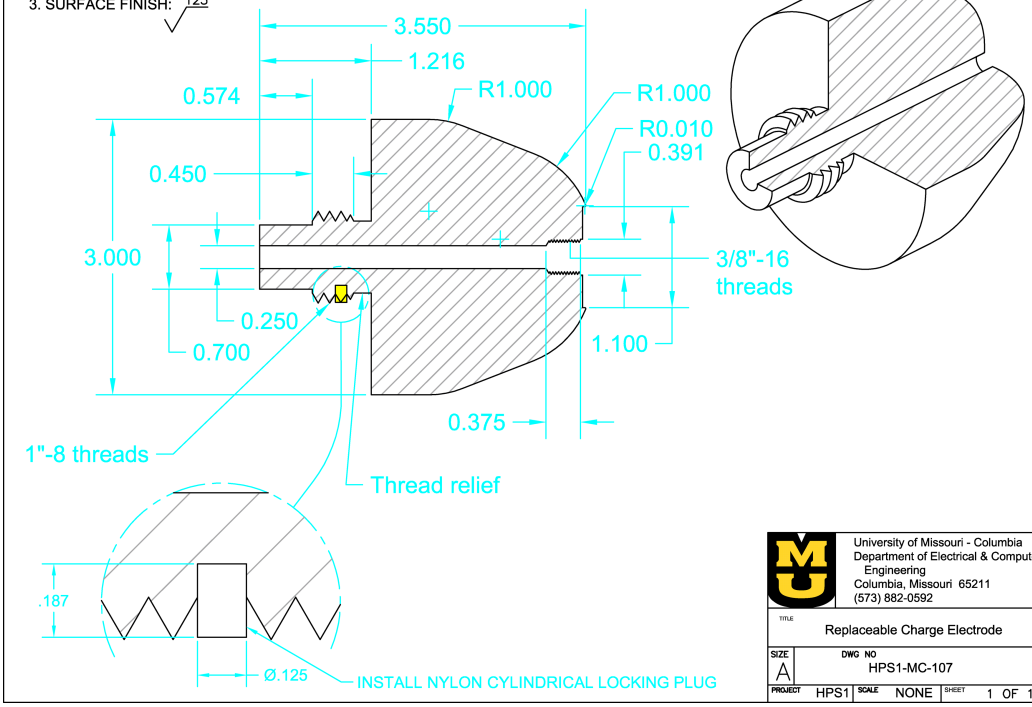

University of Missouri - Columbia
Department of Electrical & Computer Engineering
Columbia, Missouri 65211
(573) 882-0592

TITLE: Replaceable Charge Electrode

SIZE	DWG NO	REV
A	HPS1-MC-107	C

PROJECT	SCALE	SHEET
HPS1	NONE	1 OF 1

PROPRIETARY INFORMATION

REVISIONS			
REV	DESCRIPTION	DATE	APPROVED
-	BASELINE	03/12/04	
A	ADDED NYLON LOCKING FEATURE	01/05/05	
B	REMOVED NIB, ADDED GROOVE NOTES 2&3	02/05/05	

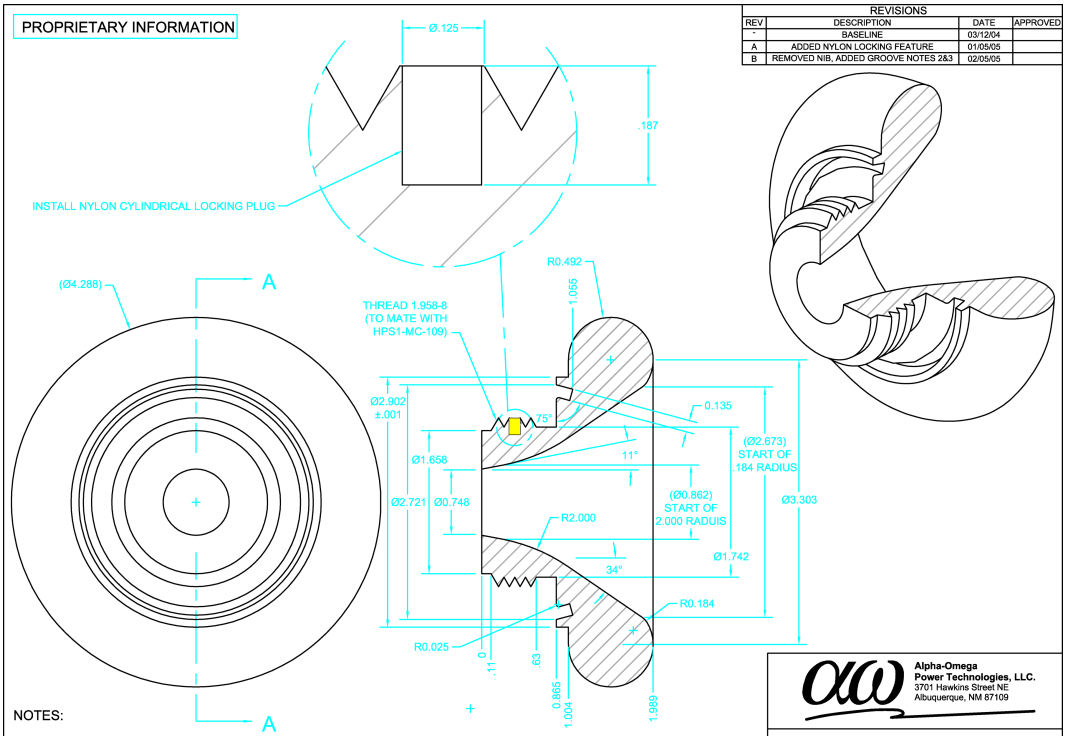

NOTES:

1. MATERIAL: COPPER-TUNGSTEN CONTACT RAY AT 341-4828.
2. TOLERANCES X.XXX ±.005, X.XX±.02.
3. SURFACE FINISH: 125

Alpha-Omega
Power Technologies, LLC.
3701 Hawkins Street NE
Albuquerque, NM 87109

TITLE: GROUND ELECTRODE

SIZE	DWG NO	REV
A	HPS1-MC-108	B

PROJECT	SCALE	SHEET
HPS1	NONE	1 OF 1

PROPRIETARY INFORMATION

REVISIONS			
REV	DESCRIPTION	DATE	APPROVED
-	BASELINE	03/12/04	
A	CHANGED THREAD FROM 12 TPI TO 28 TPI	04/29/04	

NOTES:

1. MATERIAL: STAINLESS STEEL 17-4 PH.

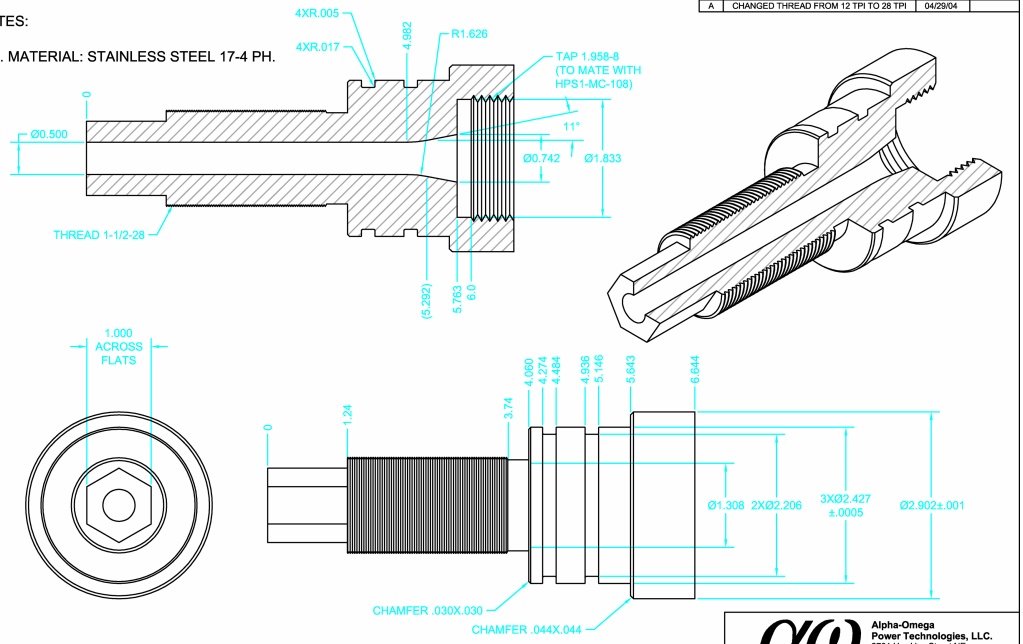

Alpha-Omega
Power Technologies, LLC.
3701 Hawkins Street NE
Albuquerque, NM 87109

TITLE: GROUND ELECTRODE ADJUSTER

SIZE	DWG NO	REV
A	HPS1-MC-109	A

PROJECT	SCALE	SHEET
HPS1	NONE	1 OF 1

PROPRIETARY INFORMATION

REVISIONS			
REV	DESCRIPTION	DATE	APPROVED
-	BASELINE	03/12/04	
A	CHANGED FROM 12 TO 28PI ON INTERNAL THREAD	04/29/04	

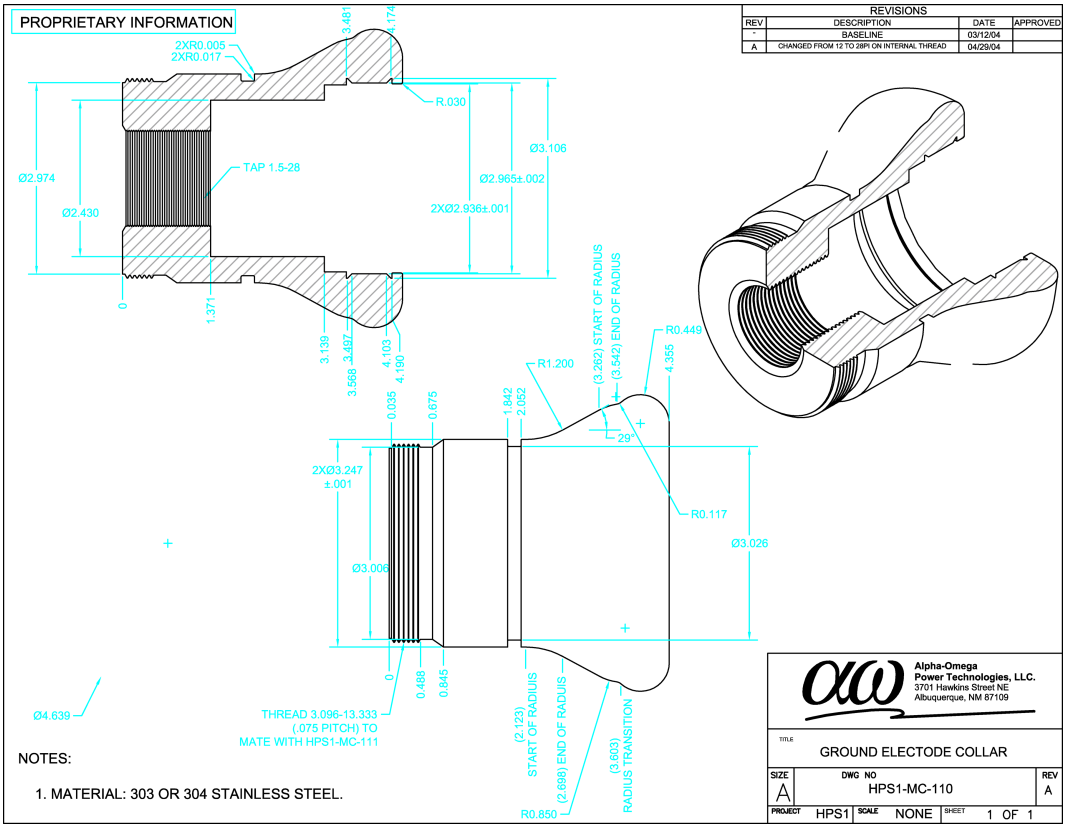

NOTES:

1. MATERIAL: 303 OR 304 STAINLESS STEEL.

Alpha-Omega Power Technologies, LLC.
3701 Hawkins Street NE
Albuquerque, NM 87109

TITLE: GROUND ELECTODE COLLAR

SIZE	DWG NO	REV
A	HPS1-MC-110	A

PROJECT	SCALE	SHEET
HPS1	NONE	1 OF 1

PROPRIETARY INFORMATION

REVISIONS			
REV	DESCRIPTION	DATE	APPROVED
-	BASELINE	03/12/04	

NOTES:

1. MATERIAL: ALUMINUM 6061-T6
2. FINISH: CHEMICAL FILM - IRIDITE, Mil-C-5541E CLASS 3.

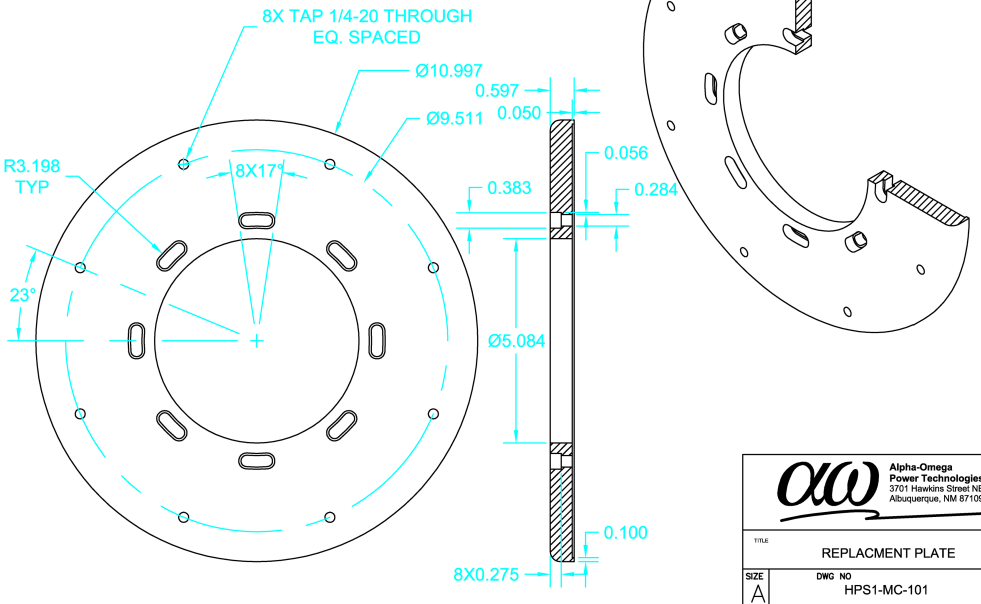

Alpha-Omega Power Technologies, LLC.
3701 Hawkins Street NE
Albuquerque, NM 87109

TITLE: REPLACMENT PLATE

SIZE	DWG NO	REV
A	HPS1-MC-101	–

PROJECT	SCALE	SHEET
HPS1	NONE	1 OF 1

PROPRIETARY INFORMATION

REVISIONS			
REV	DESCRIPTION	DATE	APPROVED
-	BASELINE	03/12/04	

NOTES:

1. MATERIAL: ALUMINUM 6061-T6
2. FINISH: CHEMICAL FILM - IRIDITE, Mil-C-5541E CLASS 3.

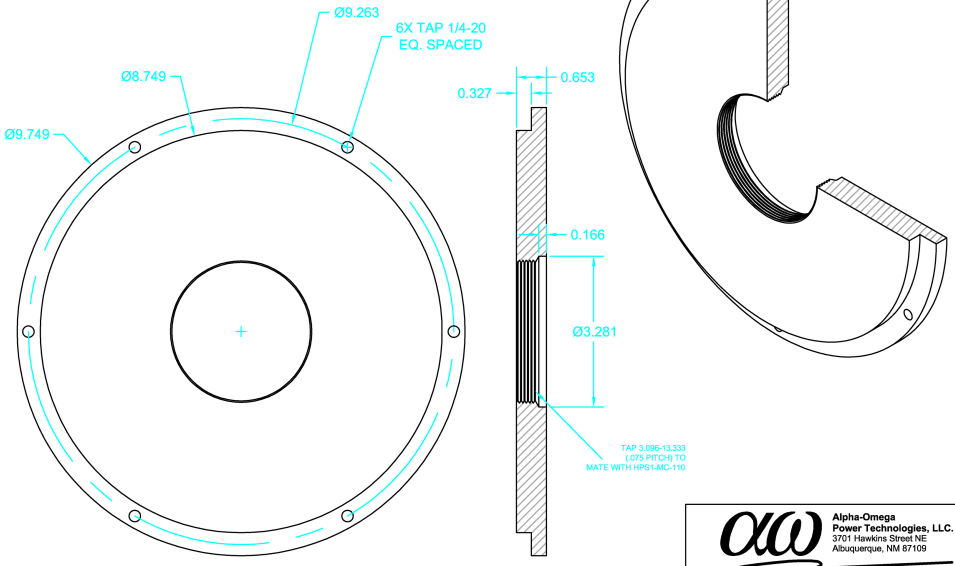

Alpha-Omega Power Technologies, LLC.
3701 Hawkins Street NE
Albuquerque, NM 87109

TITLE: FIELD SHAPER RING ADAPTER

SIZE	DWG NO	REV
A	HPS1-MC-111	–

PROJECT	SCALE	SHEET
HPS1	NONE	1 OF 1

PROPRIETARY INFORMATION

REVISIONS			
REV	DESCRIPTION	DATE	APPROVED
-	BASELINE	03/12/04	
A	FULLY DIMENSIONED PART	07/16/04	

NOTES:

1. MATERIAL: 6061-T6 ALUMINUM.
2. FINISH: CHEMICAL FILM - IRIDITE, Mil-C-5541E CLASS 3.

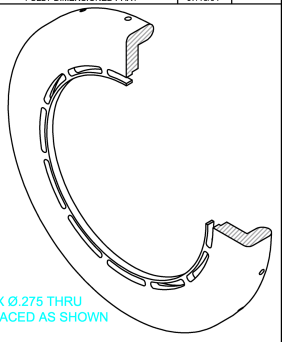

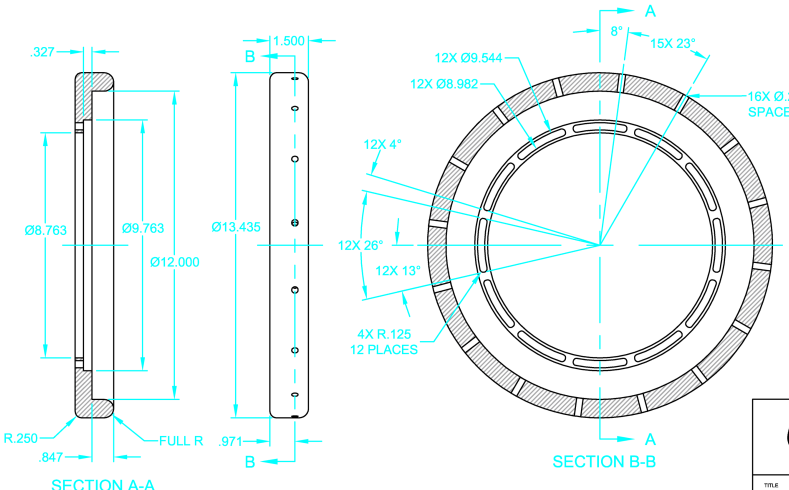

Alpha-Omega Power Technologies, LLC.
3701 Hawkins Street NE
Albuquerque, NM 87109

TITLE: FIELD SHAPER MODIFICATION

SIZE	DWG NO	REV
A	HPS1-MC-112	A

PROJECT	SCALE	SHEET
HPS1	NONE	1 OF 1

PROPRIETARY INFORMATION

REVISIONS			
REV	DESCRIPTION	DATE	APPROVED
-	BASELINE	03/12/04	

NOTES:

1. MATERIAL: POLYCARBONATE

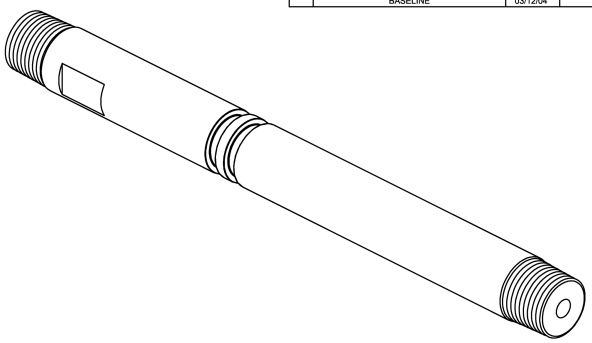

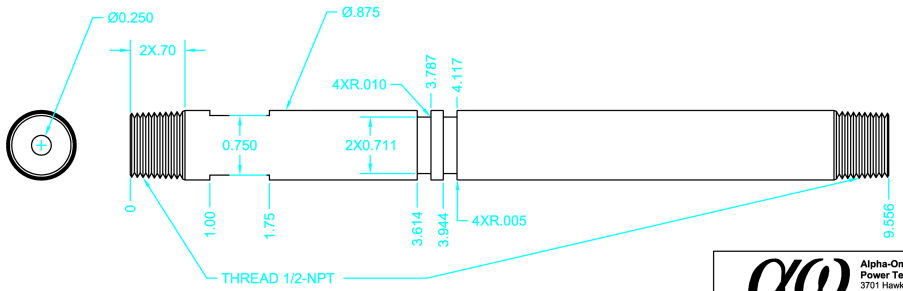

Alpha-Omega Power Technologies, LLC.
3701 Hawkins Street NE
Albuquerque, NM 87109

TITLE: TOP FLOW TUBE

SIZE	DWG NO	REV
A	HPS1-MC-113	–

PROJECT	SCALE	SHEET
HPS1	NONE	1 OF 1

PROPRIETARY INFORMATION

REVISIONS			
REV	DESCRIPTION	DATE	APPROVED
-	BASELINE	03/12/04	

NOTES:

1. MATERIAL: 1/8" ALUMINUM
2. FINISH: CHEMICAL FILM - IRIDITE, Mil-C-5541E CLASS 3.

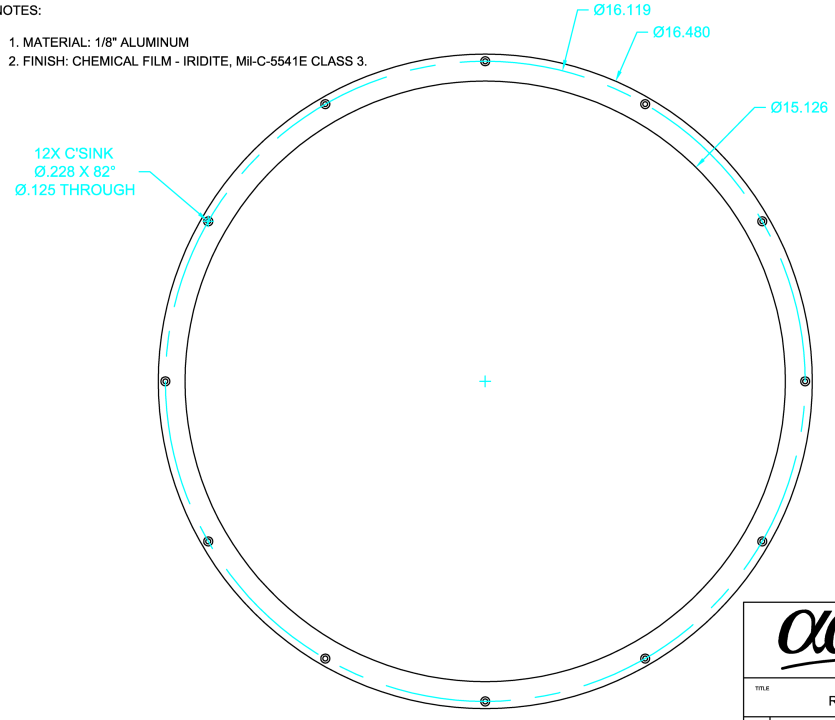

Alpha-Omega Power Technologies, LLC.
3701 Hawkins Street NE
Albuquerque, NM 87109

TITLE: RAGOWSKI COVER

SIZE	DWG NO	REV
A	HPS1-MC-114	–

PROJECT	SCALE	SHEET
HPS1	NONE	1 OF 1

PROPRIETARY INFORMATION

REVISIONS			
REV	DESCRIPTION	DATE	APPROVED
*	BASELINE	03/12/04	

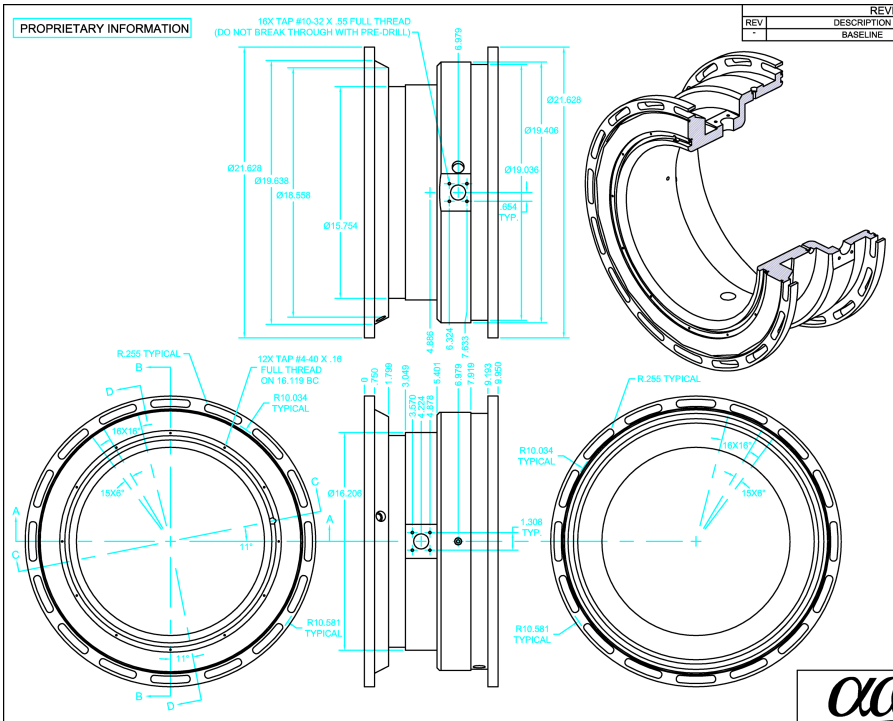

NOTES:

1. MATERIAL: ALUMINUM 6061-T6
2. FINISH: CHEMICAL FILM - IRIDITE, Mil-C-5541E CLASS 3.

Alpha-Omega
Power Technologies, LLC.
3701 Hawkins Street NE
Albuquerque, NM 87109

EXTENSION

SIZE	DWG NO	REV
A	HPS1-MC-100	–
PROJECT HPS1	SCALE NONE	SHEET 1 OF 2

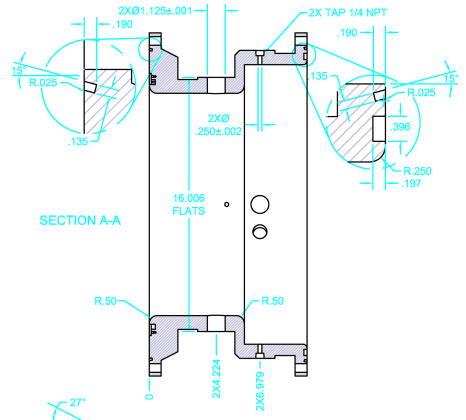

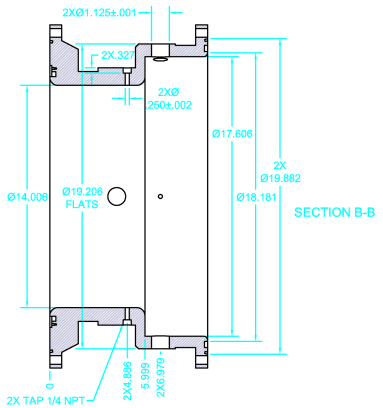

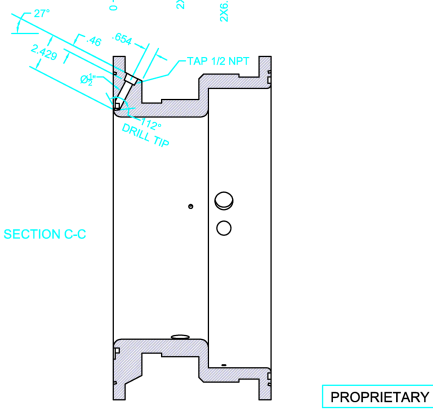

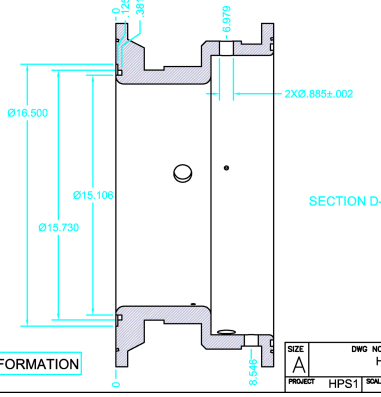

PROPRIETARY INFORMATION

SIZE	DWG NO	REV
A	HPS1-MC-100	–
PROJECT HPS1	SCALE NONE	SHEET 2 OF 2

PROPRIETARY INFORMATION

REVISIONS			
REV	DESCRIPTION	DATE	APPROVED
-	BASELINE	02/12/05	
A	Modified shape & changed electrode-side geom.	02/13/05	

NOTES:

1. Material: Natural polycarbonate plastic.

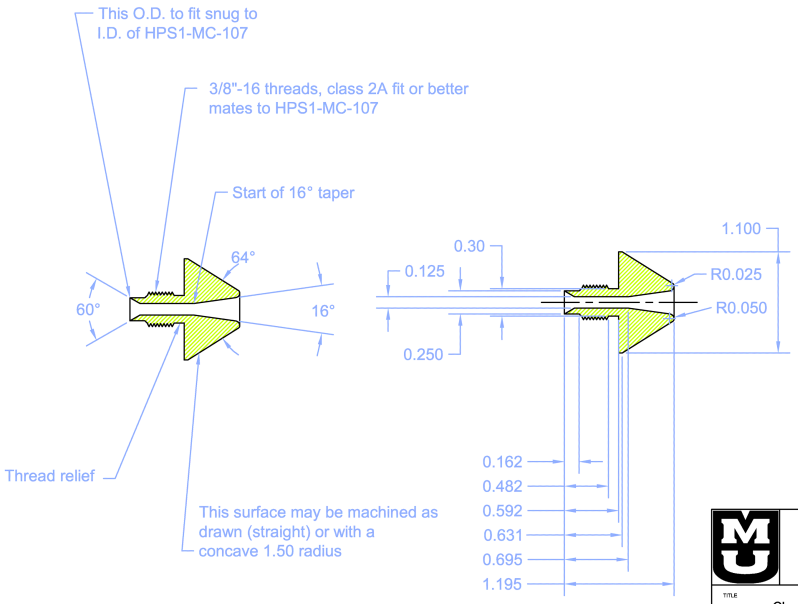

University of Missouri - Columbia
Department of Electrical & Computer Engineering
Columbia, Missouri 65211
(573) 882-0592

TITLE: Charge Electrode Nose Cone

SIZE	DWG NO	REV
A	HPS1-MC-119	A

PROJECT	SCALE	SHEET
HPS1	NONE	1 OF 1